2022

Energy Integrated Ratio Analysis of the Anomalous Precession Frequency in the Fermilab Muon g-2 Experiment

Ritwika Chakraborty

University of Kentucky, ritwika.c757@gmail.com
Author ORCID Identifier:
 https://orcid.org/0000-0003-4687-1322
Digital Object Identifier: https://doi.org/10.13023/etd.2022.357

Right click to open a feedback form in a new tab to let us know how this document benefits you.

STUDENT AGREEMENT:

I represent that my thesis or dissertation and abstract are my original work. Proper attribution has been given to all outside sources. I understand that I am solely responsible for obtaining any needed copyright permissions. I have obtained needed written permission statement(s) from the owner(s) of each third-party copyrighted matter to be included in my work, allowing electronic distribution (if such use is not permitted by the fair use doctrine) which will be submitted to UKnowledge as Additional File.

I hereby grant to The University of Kentucky and its agents the irrevocable, non-exclusive, and royalty-free license to archive and make accessible my work in whole or in part in all forms of media, now or hereafter known. I agree that the document mentioned above may be made available immediately for worldwide access unless an embargo applies.

I retain all other ownership rights to the copyright of my work. I also retain the right to use in future works (such as articles or books) all or part of my work. I understand that I am free to register the copyright to my work.

REVIEW, APPROVAL AND ACCEPTANCE

The document mentioned above has been reviewed and accepted by the student's advisor, on behalf of the advisory committee, and by the Director of Graduate Studies (DGS), on behalf of the program; we verify that this is the final, approved version of the student's thesis including all changes required by the advisory committee. The undersigned agree to abide by the statements above.

<div align="right">

Ritwika Chakraborty, Student

Dr. Tim Gorringe, Major Professor

Dr. Christopher Crawford, Director of Graduate Studies

</div>

Energy Integrated Ratio Analysis of the Anomalous Precession Frequency in the Fermilab Muon g-2 Experiment

---

DISSERTATION

A dissertation submitted in partial
fulfillment of the requirements for
the degree of Doctor of Philosophy
in the College of Arts and Sciences
at the University of Kentucky

By
Ritwika Chakraborty
Lexington, Kentucky

Director: Dr. Tim Gorringe, Professor of Physics
Lexington, Kentucky
2022

ABSTRACT OF DISSERTATION

Energy Integrated Ratio Analysis of the Anomalous Precession Frequency in the
Fermilab Muon g-2 Experiment

The muon's anomalous magnetic moment, a_μ, provides a unique way for probing physics beyond the standard model experimentally as it gathers contributions from all the known and unknown forces and particles in nature. The theoretical prediction of a_μ has been in greater than 3 σ tension with the experimental measurement since the results of the Muon g-2 Experiment at the Brookhaven National Laboratory (E-821) were published in the early 2000s with a precision of 540 ppb. To settle this tension, the new Fermilab Muon g - 2 Experiment (E-989) is currently taking data with the aim of experimentally determining a_μ with a final precision of 140 ppb. The determination of a_μ involves measuring the magnetic field in which the muons undergo spin precession and the anomalous part of the spin precession frequency, ω_a. We use a new reconstruction approach called the energy integrating method in which the total energy of the decay positrons deposited in the electromagnetic calorimeters is continuously recorded. This reconstruction method for the ω_a analysis has different sensitivity to some of the major systematic biases compared to the traditional method which reconstructs individual positron events. Furthermore, we employ a ratio histogramming procedure that has reduced sensitivity to slow variations in the data. In this dissertation the muon g-2 experiment at Fermilab is described followed by a detailed discussion of the Run-2 and Run-3 precession frequency data analysis using the new energy integrating ratio histogramming method.

KEYWORDS: muon, anomaly, precession, precision, standard model, ratio q-method

<div align="right">

Ritwika Chakraborty

September 21, 2022

</div>

Energy Integrated Ratio Analysis of the Anomalous Precession Frequency in the
Fermilab Muon g-2 Experiment

By
Ritwika Chakraborty

<div align="right">

Dr. Tim Gorringe
Director of Dissertation

Dr. Christopher Crawford
Director of Graduate Studies

September 21, 2022
Date

</div>

To Mamoni (my mother),
the most incredible person that I have ever known

Ran Hong and Zachary Hodge for introducing me to the Data Acquisition system for the experiment and teaching me the basics. I would especially like to thank Stefano Mastroianni for helping me navigate my way through the workings of the DAQ. His willingness to help me out whenever I encountered a tricky situation while being DAQ-on-call during the experimental run and to answer my questions at odd hours has truly been of enormous help to me.

I would also like to thank the members of Q-method group Fang, Dima and Joey for their support. My special thanks to Laura for spending a lot of time discussing the details of the analysis and helping me debug a lot of my codes. Working with this group has really been a great pleasure. And I would also like to thank my friends in the physics department who made me feel at home away from home, Murchhana, Ashish, Nikhil, Abel, Michelle and Rashika.

I am also very thankful towards my friends who have made sure that our friendship does not suffer from the long distances between us, especially, Shikha, Sachin, Arundhati, Kunal and Prasun. Special thanks to Geo, for always being there through thick and thin and helping me out during the last stretch of the thesis writing. I am very grateful towards my father for his unending love and for being the constant source of encouragement and support especially during the darkest of times. And finally I am eternally thankful to my mother, to whom this thesis is dedicated. She has been the best teacher I have ever had in my entire life and she is the reason behind my love for math and eventually physics. It was because of her, I had the courage to start my journey in graduate school to study physics and I just wish she was around to see me finish it.

TABLE OF CONTENTS

Chapter 1 Introduction

The work detailed in this dissertation describes a precision measurement of the anomalous magnetic moment of a subatomic particle called the muon. For almost a century the determination of magnetic moments of the subatomic particles has been of great interest to the physicists, and it has advanced our understanding of the nature of the universe. The Muon g-2 experiment in Fermilab aims to do the same by carrying out a measurement of the anomaly in muon's magnetic moment with an unprecedented precision. The anomaly arises due to the contribution of the virtual particles and forces in nature to the interaction of the muon with an external magnetic field. The measurement is motivated by a long standing discrepancy between the theoretical prediction and the experimental value of the anomaly. By increasing the precision on the experimental value, this experiment aims to settle this discrepancy by either confirming the theory or by strengthening the disagreement further. If the disagreement between the theory and the experiment widens, this could mean that our physical understanding of nature is not complete and there are more unknown particles or forces that are yet to be discovered.

This chapter details the importance of magnetic moments of the subatomic particles and introduces the muon and the significance of its magnetic moment. Further it motivates the purpose of the experiment being carried out in Fermilab. Chapter 2 discusses the measurement principle and gives a detailed description of the experimental setup required to carry out this measurement. Chapter 3 describes the development of a new technique for the determination of the anomalous precession frequency of the muon which is one of the two prime components that go into the experimental measurement of its anomalous magnetic moment, the other being the magnetic field in presence of which the muons undergo spin precession. This method is an important alternative way of determining the precession frequency and serves to show the robustness of the experimental measurement. A brief overview of the Run-1 analysis using this new method is also given in this chapter. In Chapter 4, an improvement in the histogramming technique is introduced which is motivated by the need for reducing the systematic uncertainty on the spin precession frequency measurement determined using the alternative technique. Chapter 5 describes the analysis of Run-2 and Run-3 data using this improved new technique and provides the blinded analysis results. The last chapter is a summary of the Run-1 results and its significance and the conclusions drawn from the Run-2 and 3 blinded analysis using the new improved technique.

1.1   g-factor of Charged Particles

1.1.1   Classical Magnetic Moment

Charged particles possessing angular momentum have an intrinsic magnetism characterized by their magnetic moments. A simple case is shown in the figure 1.1, where a particle with charge q and mass m, is following a circular loop of radius r and velocity v. The orbital angular momentum of this particle can be expressed as

$$\vec{L} = m\,\vec{r} \times \vec{v} \tag{1.1}$$

The magnetic moment of this charged particle then can be defined as

$$\vec{\mu} = g\frac{q}{2m}\vec{L} \tag{1.2}$$

where g is a dimensionless quantity and is defined as the ratio of the angular momentum and the magnetic moment of a particle. For our system of a charged particle rotating in a circular loop,

$$g = 1. \tag{1.3}$$

This relation holds true for all the classical charged particles even at the atomic level[1]. But this relation fails when quantum mechanics comes into play.
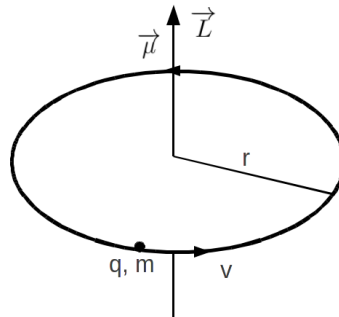
Figure 1.1: A charged particle with mass, m, and charge, q, rotating in a circular loop of radius, r, with velocity v, has an orbital angular momentum, L and possesses a magnetic dipole moment μ .

1.1.2   Spin Angular Momentum

Since the rise of quantum mechanics in the early 20th century, the structure of the subatomic particles has been widely studied. In 1926, Uhlenbeck and Goudsmith [4] hypothesized that the electron possessed an intrinsic spin angular momentum. In 1922, Stern and Gerlach [5] had already shown the *spatial quantization of angular*

momentum in their well known experiment with silver atoms in an inhomogeneous magnetic field[2] in which the beam of silver atoms was observed to be split into two distinct components along the direction of the dipole magnetic field. This observation was later interpreted as the quatization of the spin angular momentum. Existence of the spin quantum number would explain the anomalous Zeeman effect in which the number of spectral lines of an atom in presence of an external magnetic field were not equal to what would be expected if the electrons only possessed orbital angular momentum. This also led to the explanation that the interaction between the magnetic moment of the electron and its spin angular momentum was twice as strong as the interaction between the magnetic moment of the electron and its orbital angular momentum [1]. So, replacing orbital angular momentum, $\vec{L}$, with spin angular momentum $\vec{S}$ in equation 1.2,

$$\vec{\mu} = g\frac{q}{2m}\vec{S} \tag{1.4}$$

where

$$g = 2 \tag{1.5}$$

In 1927, it was shown by Thomas [6] [7] that the value $g = 2$, which was needed to explain the experimental observations, can be deduced by using relativistic kinematics.

1.2 Numerical Value of g-factor

1.2.1 Dirac Equation

The first robust theoretical prediction of numerical value of g for spin half charged elementary particles was given by Dirac [8] in 1928 by combining quantum mechanics and special relativity in his equation which describes free spin half charged particles

$$i\gamma^\mu\partial_\mu\psi(x) - m\psi(x) = 0 \tag{1.6}$$

where γ_μ are a set of 4×4 constant matrices called *gamma matrices*, ψ is the field of particles like electrons and ∂_μ is the four component (three space-like and one time-like) gradient or derivative. Dirac equation eventually led to formulation of *Quantum Field Theory (QFT)* to describe creation and annihilation of relativistic particles. In this theory, instead of working with individual particles, the concept of particle *fields* was introduced to deal with relativistic systems containing multiparticle states.

To include the electromagnetic interaction, the Dirac equation is modified to

$$\gamma^\mu(i\partial_\mu - eA_\mu)\psi(x) - m\psi(x) = 0 \tag{1.7}$$

where A_μ is the four component electromagnetic vector potential and e is the charge on an electron. In perturbation theory, the mathematical formalisms for working with such field equations allow for diagrammatic representation known as Feynman

diagrams[3]. Figure 1.2 shows a Feynman diagram for the simple interaction between an electron and electromagnetic field. The mathematical object connected with this interaction point is called the *electron vertex function.*
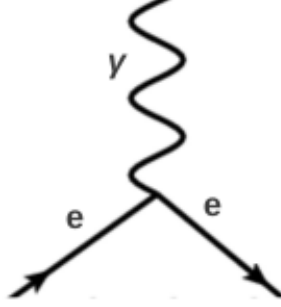
Figure 1.2: Feynman diagram for an electron, e, interacting with electromagnetic field, γ. The straight lines denote the electron and the wavy line denotes the photon.

In QFT, particle interactions (scattering amplitude, cross sections etc) are calculated using the scattering or the $S-matrix$. For charged spin half particles interacting with electromagnetic potential, the invariant matrix element of S-matrix, $\mathcal{M}$, in the fourier space is given by[3]

$$i\mathcal{M} = -i(2m).e\xi'^{\dagger}(-\frac{1}{2m}\sigma^k[F_1(0) + F_2(0)])\xi\tilde{B}^k(\overrightarrow{q}) \tag{1.8}$$

where, ξ are the two-component spinors that solve the Dirac equation in the non-relativistic limit, σ^k are the Pauli spin matrices, $F_1(q^2)$ and $F_2(q^2)$ are the Dirac and Pauli form factors respectively, and are functions of scalar four-momentum transfer squared, q^2, and $\tilde{B}^k(\overrightarrow{q}) = -i\epsilon^{ijk}q^i\tilde{A}^j(\overrightarrow{q})$. This can be interpreted as the Born approximation to the scattering of a charged spin half particle by a potential well where the potential is the interaction with the magnetic field, $-\overrightarrow{\mu}.\overrightarrow{B}$ [3] and for a slowly varying electrostatic field over large distances, $\overrightarrow{q} \to 0$. Consequently, in the leading order $F_1 = 1$ and $F_2 = 0$, so

$$\overrightarrow{\mu} = \frac{e}{m}\xi'^{\dagger}\frac{\overrightarrow{\sigma}}{2}\xi \tag{1.9}$$

And since $\overrightarrow{S} = \overrightarrow{\sigma}/2$,

$$g = 2 \tag{1.10}$$

and the next order terms in perturbation theory are higher order in the fine structure constant, α.

1.2.2 Deviation from g=2

Around this time, more experiments were done to test the predictions of Dirac theory. Notably in 1933, Stern [9] [10] performed an experiment with a molecular hydrogen beam and determined the magnetic moment of the proton to be much larger than 2. At that time, it was believed that protons and electrons are similar point like spin half particles with opposite charges. In 1939, Alvarez [11] measured the magnetic moment of neutrons by determining their Larmor precession frequency in the presence of magnetic field and found that to be much larger than 2 as well. The anomalous magnetic moments of protons and neutrons were later found to be largely due to the internal structure of these composite particles.

In 1947, Kusch and Foley and others [12] [13] [14] made measurements of magnetic moment of the electron by studying the hyperfine splitting structure of atoms in presence of magnetic field and found that numerical value of g deviated from predicted value of 2 by 0.119 percent[16]

$$g = 2(1 + 0.00119) \pm 0.0001 \tag{1.11}$$

indicating that the electron possesses an *intrinsic* or *anomalous* magnetic moment above that deduced from the Dirac theory. This indicates that the Dirac theory does not describe the electron's interaction with the magnetic field completely.

1.2.3 Quantum Electrodynamics
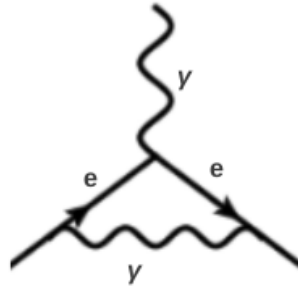
Figure 1.3: Feynman diagram for radiative correction to vertex function involving one virtual photon loop. The solid line represents the electron and the wavy line denotes the photon.

In 1947, Schwinger [15] proposed the theory of *Quantum Electrodynamics* in which the interaction of an electron with an external electromagnetic field included production and absorption of virtual photons. This is called a *radiative correction*. The Feynman diagram for such an interaction now includs a loop denoting the virtual photon as shown in figure 1.3. Schwinger calculated this correction precisely [15] and thus explained the anomalous part of the magnetic moment.

Mathematically, the next to leading order term in equation 1.8 can be calculated to be

$$F_2(0) = \frac{\alpha}{2\pi} \approx 0.0011614 \tag{1.12}$$

And thus, anomalous magnetic moment of electron is

$$g = 2(1 + 0.0011614) \tag{1.13}$$

which is in agreement with Kusch and Foley's result in equation 1.10.

1.3 Muon and the Standard Model

1.3.1 Discovery of Muon

In 1936, Anderson and Neddermeyer [17] identified a new class of particles in cosmic rays using cloud chambers. These particles were as ionizing as electrons but showed a higher charge to mass ratio characterized by more curled particle tracks in the presence of a magnetic field inside the ionization chambers. In 1937, their discovery was confirmed by Street and Stevenson [18]and they also measured the mass of this new class of particles which was found to be approximately a couple of hundred times heavier than the electron. In 1946, Conversi, Pancini, and Piccioni [19] demonstrated that these new particles were unstable and decayed into lighter electrons. These newly discovered particles were called *muons*.

1.3.2 Properties of Muon

As mentioned in the last subsection, muons are elementary particles with the same charge as electrons. Their rest mass is about 105.7 MeV/c^2 which is 207 times the mass of the electron (0.511 MeV/c^2). Muons are radioactive and primarily decay into electrons and neutrinos via weak interaction as shown in figure 1.4. Their average lifetime is 2.2 μs.

1.3.3 The Standard Model

The Standard Model of particle physics is a field theory of elementary particles and their interactions. The particles having spin 1/2 are called *fermions* and they are the constituents of all the stable matter in the universe. The interactions of the particles are mediated by the *force carriers*. They are *bosons* with spin 1 and the Higgs boson is the only particle in the Standard Model with spin 0. Figure 1.5 shows all the particles and the force carriers described by the Standard Model. The force carriers are gluons, photons, W and Z bosons and they are responsible for strong force, electromagnetic force and the weak force respectively. The fermions can be either *leptons* or *quarks* which are the building blocks of the universe. Quarks can interact via all the fundamental forces in nature and are always found in bound states in nature (for example inside protons and neutrons) while the leptons can only interact via the gravitational, weak or electromagnetic interaction. There are three
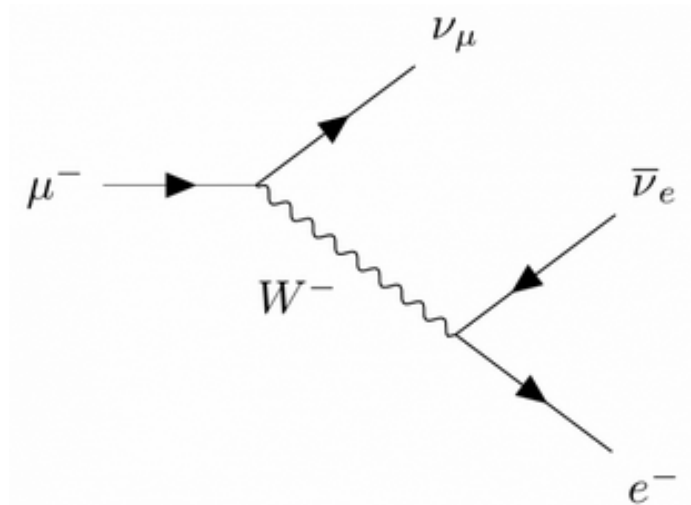
Figure 1.4: Feynman diagram for decay of muon, μ^- into electron, e^-, and neutrinos, $\bar{\nu}_e$ and ν_μ, mediated by weak interaction force carrier, W^- boson

generations of each of the particles usually characterized by their masses. Finally there is the Higgs boson which is responsible for the mass generation of the massive vector bosons and all the fermions.

1.3.4   Standard Model Prediction of Muon g-2

Since the interaction of the electron (or any spin half charged particle) with an electromagnetic field can be influenced by all possible virtual particles coming in and out of existence in the vacuum, the anomalous part of the magnetic moment, ((g-2)/2), will gather contribution from all the particles and forces in nature that couple to the electron. Using the standard model of particle physics one can calculate the various contributions from the known particles and forces. The first order correction to the anomalous part of an electron's magnetic moment is already shown in equation 1.13. This also holds true for muons and taus. However the higher order corrections are mass dependent and hence the heavier leptons have different contributions from the higher order terms. In other words, the contribution of higher order contributions involving higher energy or mass scales, Λ, to a lepton's anomalous magnetic moment goes as [21]

$$\delta a_l \propto \frac{m_l^2}{\Lambda^2} \tag{1.14}$$

where we have defined $a_l = (g_l - 2)/2$. This implies that the anomalous magnetic moment of the muon which is ~ 200 times heavier than the electron is $m_\mu^2/m_e^2 \approx 40000$ times more sensitive to these corrections than an electron. This, along with the fact that muons are more stable than taus, are the reasons why the comparisons with experimental measurement of anomalous magnetic moments of leptons are done with muons. The development of the Muon g-2 experiments will be discussed in detail in

7
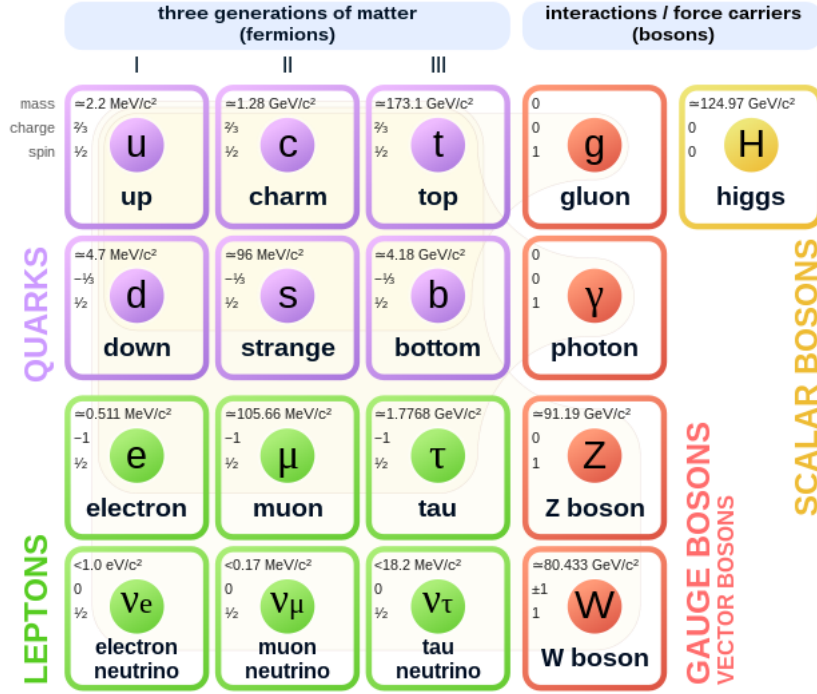
Figure 1.5: The standard model of particle physics. In violet color are the three generations of up and down quarks, the leptons are shown in green, in red are the four force carriers and the Higgs boson is shown in yellow. Image credit [20].

the next subsections.

The standard model predicts that contributions to anomalous magnetic moment of muons, $a_\mu(= (g_\mu - 2)/2)$, are from three types of corrections, quantum electrodynamics (QED), electro-weak (EW) interactions and hadronic (Had).

$$a_\mu^{SM} = a_\mu^{QED} + a_\mu^{EW} + a_\mu^{Had} \tag{1.15}$$

The contribution from the hadronic virtual loops (a_μ^{Had}) dominate the uncertainty on the overall standard model prediction of a_μ. As a result, a lot of the recent focus has been on developing ways of precisely calculating a_μ^{Had}. To arrive at a concensus on the theoretical value of the muon magnetic anomaly, a group was formed called *Muon g-2 Theory Intitiative*, whose goal is to recommend a single value of a_μ^{SM}. The first recommendation was published in 2020 as a white paper[22]. Following this recommendation, the numerical standard model value of muon magnetic anomaly is

$$a_\mu^{SM} = 116592089(63) \times 10^{-11} \tag{1.16}$$

Each of the components of this correction are described below.
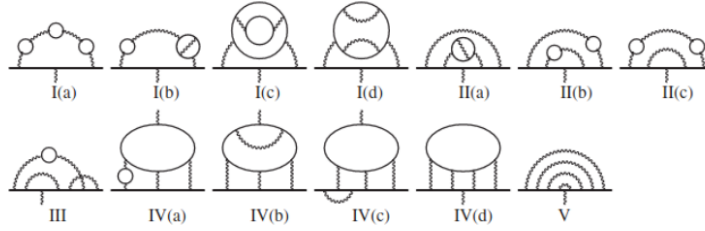
Examples of 4-loop Feynmann Diagrams
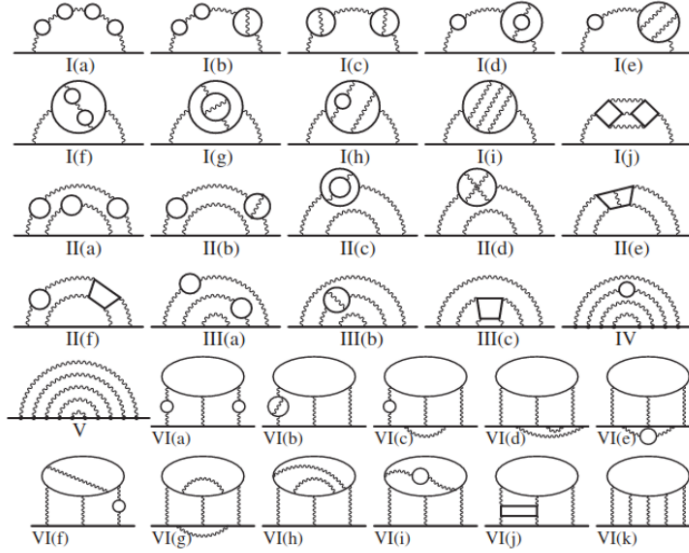
Examples of 5-loop Feynmann Diagrams

Figure 1.6: Feynman diagrams showing the 8th and 10th corrections to the vertex diagram. The top two rows show the four-loop diagrams corresponding to 8th order QED corrections while the bottom six rows show the five-loop diagrams for the 10th order QED corrections to muon magnetic anomaly [23].

Quantum Electrodynamics (QED)

The first order correction to (g-2)/2 given in equation 1.13 is called the one loop QED correction since the virtual photon forms a loop at the vertex. The higher order corrections are obtained by doing a perturbative expansion in terms of α.

$$a_\mu^{QED} = \sum_{n=1}^{\infty} (\frac{\alpha}{\pi})^n a_\mu^{2n} \tag{1.17}$$

In terms of Feynman diagrams, this means the number of photon loops are increased in each subsequent higher order. The representative diagrams from the four and five loop contributions are shown in figure 1.6. Currently, the corrections upto 5-loops (10th order in a_μ) have been estimated [23] and the total contribution from

9

the QED corrections is

$$a_\mu^{QED} = 116584718.931(104) \times 10^{-11} \tag{1.18}$$

The uncertainty comes from lepton mass ratios, numerical evaluation of 8th and 10th order terms and the uncertainty from the determination of α done with atom-interferometry measurements of the Cs atom[25].

Electro-weak (EW)
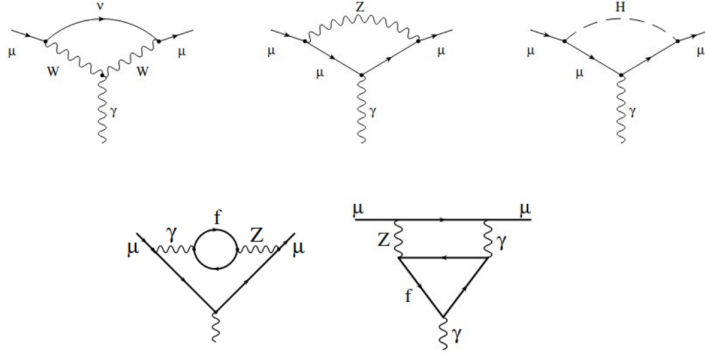
Figure 1.7: Feynman diagrams showing the one-loop and two-loop diagrams contributing to the electroweak corrections to muon magnetic anomaly. The wavy lines represent the vector bosons and the dotted line is for the Higgs boson [24].

The contributions from the EW corrections come in due to the appearance of the massive bosons at the vertex. They can be any of the vector bosons (W or Z) or the Higgs particle. These contributions are calculated upto two-loop order and are generally suppressed due to the high mass of the bosons relative to the muon [24]. The contribution to muon magnetic anomaly from EW corrections is

$$a_\mu^{EW} = 153.6(1.0) \times 10^{-11} \tag{1.19}$$

Hadronic

The hadronic contributions come from the Feynman diagrams where quarks appear at the vertex. The calculation of hadronic contributions to a_μ poses an additional challenge owing to the non-perturbative nature of QCD (Quantum Chromodynamics). One of the hadronic contribution is called *hadronic vacuum polarization* (HVP) as shown in figure 1.8. This can be calculated with the use of experimental cross-section data, involving e^+e^- annihilation to hadrons, and perturbative QCD to evaluate energy-squared dispersion integrals [26], [27]. The leading order term in the dispersion integral is [28], [29]

$$a_\mu^{HVP,LO} = \frac{\alpha^2}{3\pi^2} \int_{m_\pi^2}^{\infty} \frac{ds}{s} R(s) K(s) \tag{1.20}$$

10

where m_π is the mass of pion, $K(s)$ is the kernel function and $R(s)$ is defined as

$$R(s) = \frac{\sigma^0_{had,\gamma(s)}}{4\pi\alpha^2/(3s)} \tag{1.21}$$

with

$$\sigma^0_{had,\gamma(s)} \equiv \sigma^0(e^+e^- \to \gamma* \to hadrons + \gamma) \tag{1.22}$$

The leading order HVP contribution to a_μ is

$$a_\mu^{HVP,LO} = 6931(40) \times 10^{-11} \tag{1.23}$$

Similarly, the next to leading order (NLO) and next-to-next leading order (NNLO) are evaluated to be

$$a_\mu^{HVP,NLO} = 98.3(7) \times 10^{-11}, a_\mu^{HVP,NNLO} = 12.4(1) \times 10^{-11} \tag{1.24}$$
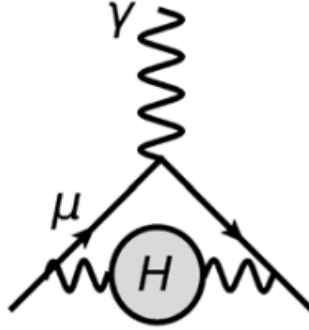
Figure 1.8: Feynman diagram showing the hadronic vacuum polarization contribution to the muon magnetic anomaly. The solid line represents the muon and the wavy line denotes the photon. The gray circle represents the quark loop.

Very recently, HVP contributions to a_μ^{SM} have also been calculated using lattice QCD techniques which do not rely on experimental data on electron-positron annihilation into hadrons or dispersive techniques [30],[31],[32]. These predictions differ from the dispersive predictions by couple of standard deviations and are in tension with the HVP contribution value recommended by the theory initiative white paper. These results are currently being reviewed by the Muon g-2 Theory Initiative and the numerical value of the hadronic contributions to a_μ^{SM} will be updated according to their recommendation.

The other type of hadronic contribution is called *hadronic light-by-light* (HLbL) shown in figure 1.9. The correction is determined phenomenologically by using dispersive
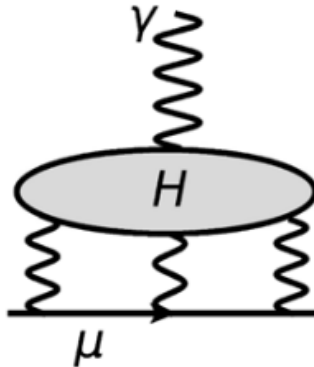
Figure 1.9: Feynman diagram for hadronic light-by-light correction. It shows the hadronic loop in gray coupling to four photons. The solid line represents the muon and the wavy line denotes the photon.

relations similar to the HVP case. The main contributions come from data driven estimation of numerically dominant contributions from the single-pseudoscalar poles and large parts of the two-pion intermediate states, the model-dependent estimates for the sum of scalar, tensor, and axial-vector contributions and perturbative QCD determination of the c-quark contribution [22]. The leading order and next to leading order estimates of a_μ are

$$a_\mu^{HLbL,LO} = 92(19) \times 10^{-11}, a_\mu^{HLbL,NLO} = 2(1) \times 10^{-11} \tag{1.25}$$

1.4 Experimental Measurement of Muon g-2

1.4.1 History of Muon g-2 Experiments

An important concept behind the experimental measurement of anomalous muon magnetic moment is the fact that parity is not conserved in weak interactions [33] [34]. In 1957, Garwin, Lederman and Weinrich experimentally showed that parity was violated in decay of pions to muons and then muons to electrons [35]. As a result of this observation, it was possible to directly measure the muon anomalous magnetic moment using naturally polarized muon beams. In 1959, Garwin et al. first measured muon's g-factor by stopping a beam of muons in a bromoform target in presence of a homogeneous magnetic field. They reported their value of g with a 0.007% accuracy[36]

$$g = 2(1.00122 \pm 0.00008) \tag{1.26}$$

which was in agreement with the predictions of QED at that time.

The next generation experimental measurements of a_μ were done in CERN. The first experiment, conducted between 1960 and 1962, injected a positive muon beam
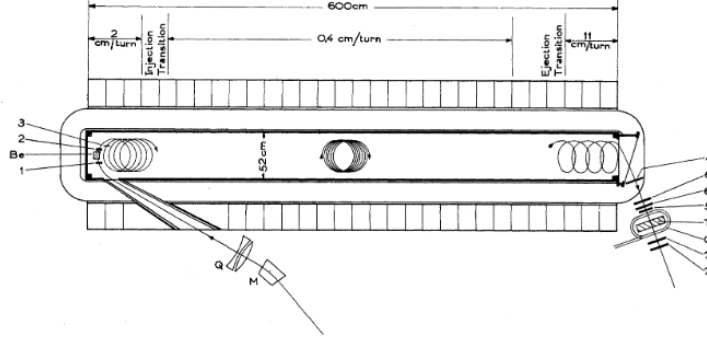
Figure 1.10: A schematic representation of muons spiraling in a dipole magnetic field inside the storage ring used in the CERN-1 Muon g-2 experiment. The length of the magnet is 6 meters. M denotes the bending magnet and Q denotes a pair of quadrupoles. The numbers 1 through 7 show the position of the counters for counting muon coincidences. Be is the Beryllium moderator and T is the Methylene-iodide target. Image credit [38].

in the presence of a strong dipole magnetic field as shown in figure 1.10. The muons coming out of the magnetic field region were then stopped by a methylene iodide target [37] [38]. The time distribution of the decaying muons was used to determine the anomalous magnetic moment. The second experiment was done in 1966 and involved a storage ring magnet in which the muons decayed into electrons [39]. The physics behind the storage ring magnets will be discussed in detail in the next chapter. And the third and final muon g-2 experiment at CERN was conducted between 1974 and 1979 with a storage ring magnet in which muon beam was subjected to vertical focussing using electrostatic quadruples [40] [41] [42]. The setup of CERN-3 muon g-2 experiment is shown in figure 1.11. The results of the 3 experiments from CERN are summarized below.

$$a_\mu^{CERN-1} = (1162 \pm 5) \times 10^{-6} \tag{1.27}$$

$$a_\mu^{CERN-2} = (11661 \pm 3.1) \times 10^{-7} \tag{1.28}$$

$$a_\mu^{CERN-3} = (1165924 \pm 8.5) \times 10^{-9} \tag{1.29}$$

These results were in agreement with the standard model prediction at that point of time.

1.4.2 Muon g-2 Experiment at Brookhaven National Lab (E-821)

In the 1980s an experiment to measure a_μ with much higher precision was proposed to be set up in Brookhaven National Laboratory (BNL). The goal of this new experiment was to look for electro-weak contribution to muon's anomalous magnetic
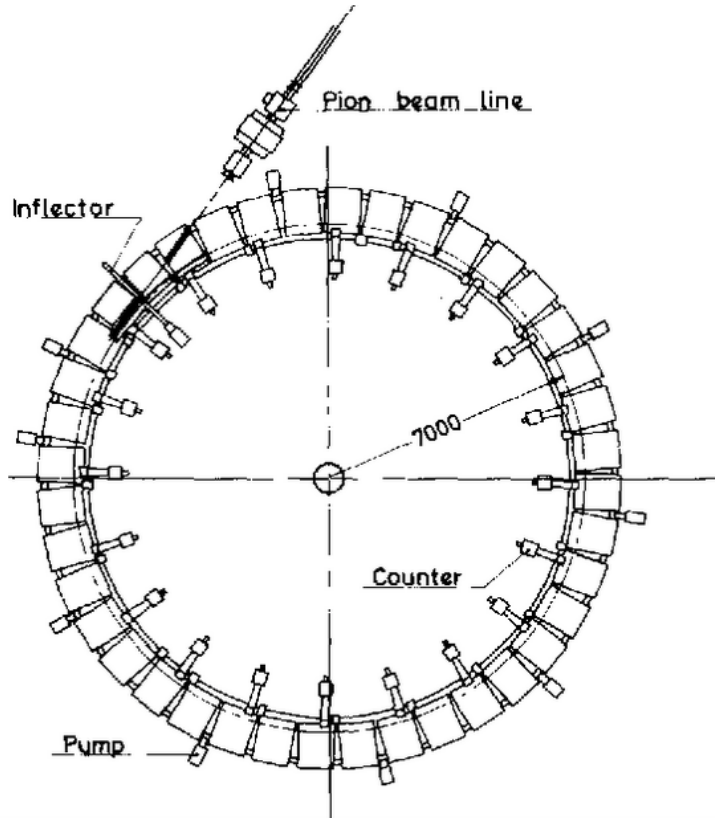
Figure 1.11: A schematic representation of the storage ring used in the CERN-3 Muon g-2 experiment. The ring, with radius 7 meters, is made up of 40 contiguous magnet pieces as shown. There are 24 lead-scintillator shower counters shown on the inner side of the ring. The pion beam was injected into the ring through an inflector magnet which provided a field free region at the entrance to the storage region indicated at the top left part of the ring [43].

moment. Additionally, this experiment would also have the scope to confirm the predictions of the standard model or look for the existence of physics beyond this theory. Some of the features of the experimental design were similar to that of the CERN-3 experiment. For example, the experiment was conducted in a storage ring with a dipole magnetic field and electrostatic quadruples were used to achieve vertical focussing. The muon beam with the same relativistic energy was used (this energy corresponding to a Lorentz boost factor of γ=29.3 had a special advantage which will be again discussed in detail in the next chapter). The significant upgrades with respect to the last experiment included a more homogenous magnetic dipole field and better method of mapping the field with the help of a trolley with a NMR probe, a more intense beam, muon kicker to directly inject muon beam in the storage region, an improved inflector magnet and a four fold symmetry in the electrostatic quadrupole system [43].

The BNL experiment concluded taking data in 2001 and accumulated a dataset which achieved a precision of 540 ppb. The final result of the experiment is

$$a_\mu^{BNL} = 116592080(63) \times 10^{-11} \tag{1.30}$$

In this, 460 ppb was statistical uncertainty while 280 ppb came from various systematic effects. This number was about 2.7 standard deviations away from the theoretical standard model prediction at that time. With improvement in precision in numerical techniques and data driven approaches to hadronic contributions, the current deviation (with respect to the theoretical value recommended by the white paper [22]) stands at about 3.7 σ as shown in figure 1.12.
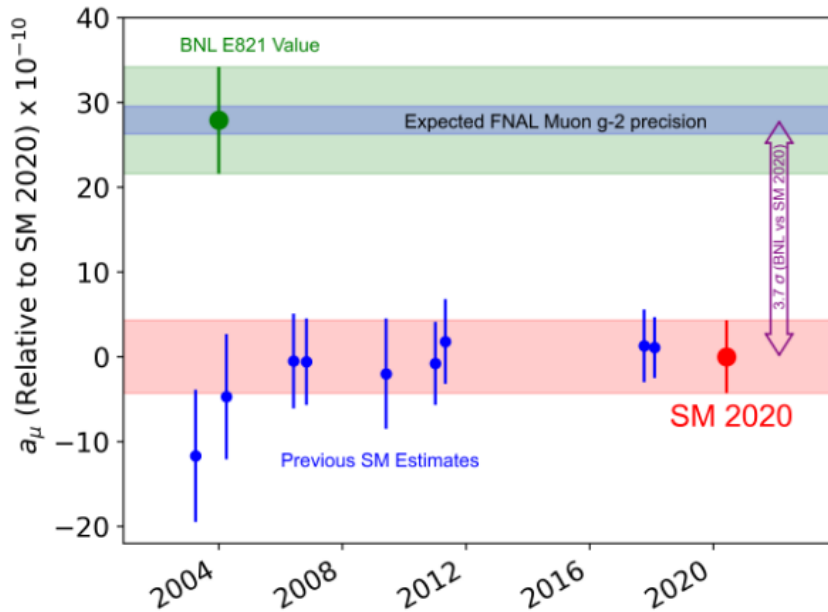
Figure 1.12: Plot showing the comparison of theoretical and experimental values of muon g-2. The points marked in blue are the old Standard Model estimates, the red point and the red band corresponds to the current standard model estimate and the associated uncertainty respectively as per [22]. The green band represents the BNL experimental value of g-2 and the associated uncertainty and the blue band within the green band shows the predicted uncertainty band for the new Fermilab g-2 experiment. Note that the current Standard Model estimate denoted by "SM 2020" in red does not include the recent lattice results [30],[31],[32] and this plot will be updated later according to the recommendation made by the Muon g-2 Theory Initiative.

While the standard model of particle physics has been tested remarkably well experimentally for all its predicted particles and their interactions, it also has some problems. It does not include gravitational force. It does not explain matter-antimatter

asymmetry observed in the universe and does not incorporate dark matter. Thus this discrepancy is a compelling hint towards the existence of unknown particles or forces that are not included in the standard model. Although 3.7 σ is a tantalizing discrepancy, it still does not meet the threshold (5 σ) to conclusively say that the standard model is incomplete. This motivates the need to improve the precision on both theoretical and experimental values of a_μ. Hence a new experiment is set up in Fermilab to achieve better precision on the muon anomalous magnetic moment.

1.4.3   Goal of Fermilab Muon g-2 Experiment

The goal of the Fermilab Muon $g-2$ experiment (E-989) is to measure anomalous magnetic moment of muon, a_μ, with a final precision of 140 ppb. If the current central experimental value agrees with the findings of E-989, this would mean a deviation of about 7σ, which is well above the discovery threshold. The new experiment aims to achieve this unprecedented precision by increasing statistics and incorporating improvements in its measurement techniques.

The storage ring magnet is the same as the one used in the BNL experiment. The experiment aims to limit its systematic uncertainties to 100 ppb with an expectation to collect data with which the statistical precision will be 100 ppb. The major instrumental upgrades include a purer source of muon beam with a higher rate of delivery to the storage ring at Fermilab, a new dedicated fast kicker, calorimeter detectors with segmented lead fluoride crystals, dedicated straw trackers to image the beam and improved magnetic field homogeneity. Each of these components will be discussed in detail in the next chapter.

Chapter 2 The Fermilab Muon g-2 Experiment

2.1 Measurement Principle

Measurement of the anomaly in muon $g - 2$ in E-989 employs the fact that a charged particle possessing spin angular momentum in presence of external magnetic field experiences a torque τ due to the interaction of its magnetic moment μ with the magnetic field B

$$\vec{\tau} = \vec{\mu} \times \vec{B} \tag{2.1}$$

and undergoes Larmor precession with angular frequency

$$\vec{\omega_s} = \frac{ge}{2m}\vec{B} \tag{2.2}$$

where g is the g-factor, e is the charge on the particle and m is its mass. For a relativistic particle, such as the muons in a storage ring with dipole magnetic field, this is given by the more generalized Thomas precession

$$\vec{\omega_s} = -\frac{ge\vec{B}}{2m_\mu} - (1 - \gamma)\frac{e\vec{B}}{m_\mu\gamma} \tag{2.3}$$

where γ is the Lorentz boost factor for the muons in the ring and m_μ is the muon mass. In a storage ring with magnetic field, the positively charged muon also undergoes cyclotron motion with an angular frequency

$$\vec{\omega_c} = \frac{e\vec{B}}{2m_\mu\gamma} \tag{2.4}$$

The difference between the two frequency or the rate of precession of muon's spin with respect to the rate of change of muon's momentum vector is given by

$$\vec{\omega_s} - \vec{\omega_c} = -\frac{ge\vec{B}}{2m_\mu} - (1 - \gamma)\frac{e\vec{B}}{m_\mu\gamma} - \frac{e\vec{B}}{2m_\mu\gamma} \tag{2.5}$$

We can rewrite this as

$$\vec{\omega_a} = -(\frac{g - 2}{2})\frac{e\vec{B}}{m_\mu} = -a_\mu\frac{e\vec{B}}{m_\mu} \tag{2.6}$$

where we have defined $\vec{\omega_a} = \vec{\omega_s} - \vec{\omega_c}$ and $a_\mu = (\frac{g-2}{2})$.

To ensure that the muons are confined to the center of the ring and do not spiral up or down, a vertical focussing is employed in the storage ring with the help of an electrostatic quadrupole system. Due to this, the muons also experience an electric field $\vec{E}$ and the above equation has to be modified to

$$\vec{\omega_a} = -\frac{e}{m_\mu}[a_\mu\vec{B} - (a_\mu - \frac{1}{\gamma^2 - 1})\frac{\vec{\beta} \times \vec{E}}{c}] \tag{2.7}$$

17

But it is possible to choose γ in such a way that $a_\mu \approx \frac{1}{\gamma^2 - 1}$ so that the term involving the E-field vanishes in the above equation. This value of $\gamma \approx 29.3$ corresponds to the so called *magic momentum*=3.09 GeV/c. So, now we have

$$\omega_a = -a_\mu \frac{e\overrightarrow{B}}{m_\mu} \tag{2.8}$$

As clear from equation 2.8, the difference between the spin precession frequency and the cyclotron frequency is non-zero only because $g \neq 2$. So, in absence of the anomalous contribution to muon's spin precession frequency, the spin will precess at the same rate as the cyclotron frequency as shown in figure 2.1.
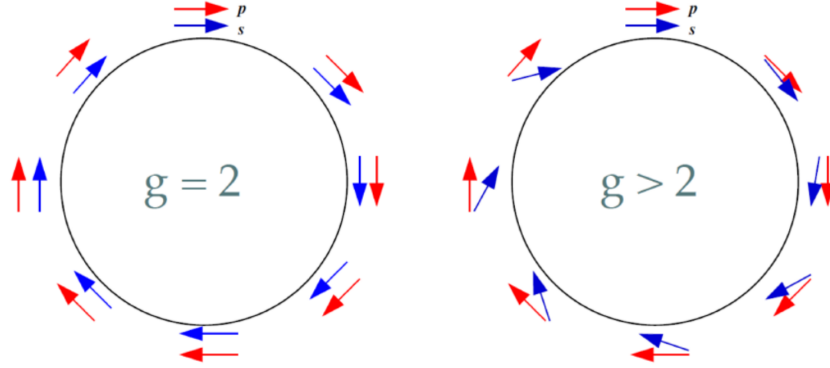
Figure 2.1: Spin precession and cyclotron motion in presence (right) and absence (left) of muon magnetic moment anomaly. The red and blue arrows denote the momentum and spin of the muon. The rate of change of momentum and spin are equal in absence of anomalous part of muon magnetic moment

From equation 2.8, it is clear that in the experimental setup of E-989, a precision measurement of the anomalous spin precession frequency, ω_a and the magnetic field, B, are required.

The magnetic field in equation 2.8 is measured using proton nuclear magnetic resonance (NMR) in the experiment which will be discussed in section 2.3. So B can be rewritten in terms of proton's Larmor frequency given by

$$B = \frac{\hbar \omega_p}{2\mu_p} \tag{2.9}$$

Similarly, the electric charge, e, can also be written in terms of constants which have been experimentally determined with high precision

$$e = \frac{4m_e \mu_e}{\hbar g_e} \tag{2.10}$$

18

Using relations 2.9 and 2.10, equation 2.8 can be rewritten as

$$a_\mu = \frac{\omega_a}{\tilde{\omega}_p} \frac{m_\mu}{m_e} \frac{\mu_p}{\mu_e} \frac{g_e}{2} \tag{2.11}$$

The quantities g_e, m_μ/m_e and μ_p/μ_e have been experimentally measured with precision 0.26 ppt[45], 22 ppb[46] and 3 ppb[47] respectively. Notice that, ω_p has been replaced by $\tilde{\omega}_p$ which is the precession frequency of the protons weighted by the muon distribution which will be discussed in section 2.3. The subsequent sections describe the measurement of the muon's anomalous spin precession frequency and the magnetic field in which the muons are stored.

2.2 Anomalous Precession Frequency Measurement

The determination of muon's anomalous spin precession frequency ω_a is based on the physical properties of the muon decay mechanism. Muons decay into positrons in storage ring following parity violating weak decay. The longitudinally polarized muons decay to positrons, electron neutrinos and muon anti-neutrinos.

$$\mu^+ \rightarrow e^+ + \nu_\mu + \overline{\nu_e} \tag{2.12}$$

Due to the parity violating weak decay, preferentially the positrons are right handed, neutrinos are left handed and anti-neutrinos are right handed. In the rest frame of the muon, the high energy positrons are emitted in the direction of the muon spin as shown in figure 2.2. When boosted to lab frame, positrons are higher energy when muon spin and momentum parallel to each other and lower energy when the muon spin and momentum are anti-parallel to each other.

In the rest frame of the muon, defining $y = E'/E_{max=53MeV}$, the differential angular distribution of the positrons is given by the following [44]

$$\frac{dP(y, \theta')}{dy d\Omega} \propto n'(y)[1 + \alpha'(y) \cos \theta'] \tag{2.13}$$

where

$$n'(y) = 2y^2(3 - 2y), \tag{2.14}$$

θ' is the angle between muon spin and positron momentum in muon rest frame and

$$\alpha'(y) = \frac{2y - 1}{3 - 2y} \tag{2.15}$$

The muons in the storage ring are highly relativistic with a lorentz factor of $\gamma = 29.3$. This causes the decay angle between the muon spin and positron momentum to be highly compressed. The observed energy of the decay positrons in the laboratory frame in terms of the rest frame energy is

$$E_{lab} = \gamma(E' + \beta p'c \cos \theta') \approx \gamma E'(1 + \cos \theta') \tag{2.16}$$
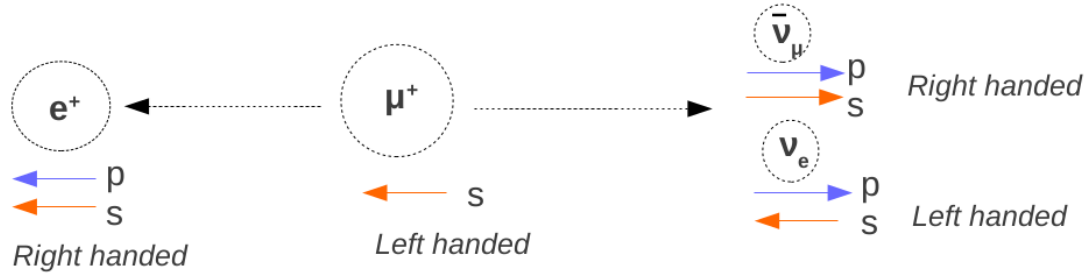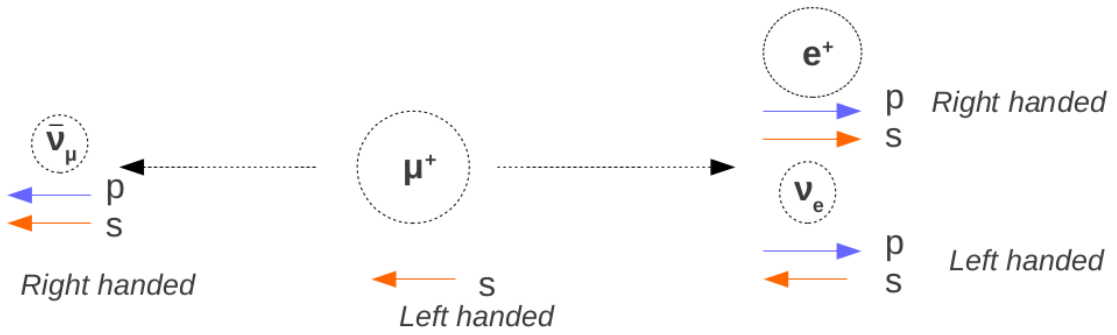
Figure 2.2: The top figure shows the emission of highest energy decay positrons while the bottom figure shows the lowest energy case in the rest frame of the muon. Due to parity violating nature of weak decay, the positrons are emitted preferentially right handed and carry information about the muon spin direction.

Note in the laboratory frame, the angle between muon spin component and momentum can also be re-written as $\theta = \omega_a t$. As the count of muons exponentially decay with a boosted lifetime of $\gamma\tau$, the integral of the number of positrons above an energy threshold is modulated by ω_a as

$$N(t) = N_0 e^{\frac{-t}{\gamma\tau_\mu}}[1 + A\cos(\omega_a t - \phi)] \tag{2.17}$$

where A is the asymmetry in the number of positrons emitted with a particular helicity due to parity violation. The asymmetry is a function of laboratory energy since the correlation between muon spin and positron momentum is stronger at higher energies. The modulation of high energy (above the energy threshold of 1.7 GeV) positrons by ω_a is shown in figure 2.3. In the experiment ω_a can be determined by fitting either the time distribution of high energy positrons (T-method) or the time distribution of the total energy of the positrons (Q-method).

20
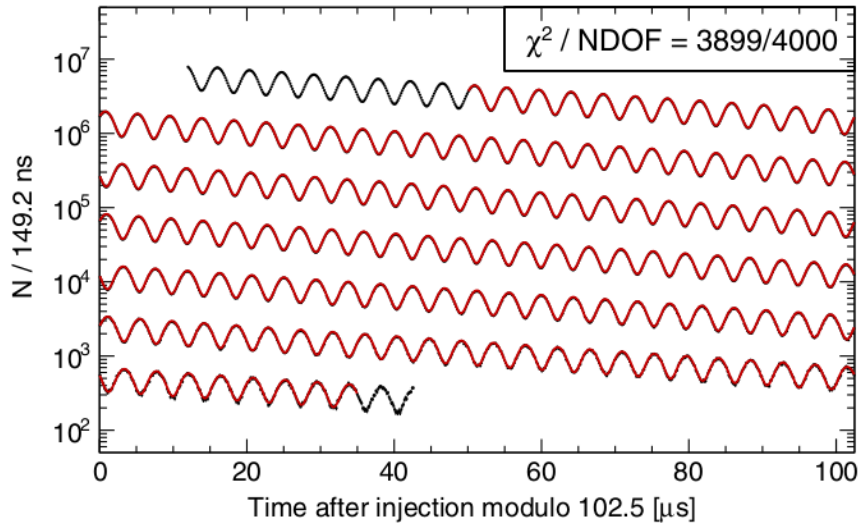
Figure 2.3: Time spectrum of high energy positrons in Run-1d above a threshold of ~1.7 GeV.

The statistical fractional error on anomalous spin precession frequency is

$$\frac{\delta\omega_a}{\omega_a} = \frac{\sqrt{2}}{\omega_a \tau_\mu \sqrt{NA^2}} \tag{2.18}$$

where N is the number of decay positrons and A is the decay asymmetry. To minimize the uncertainty on ω_a in the threshold based high energy positron counting methods (T-method), the energy threshold which maximizes the quantity NA^2 (plotted in figure 2.4) is chosen. This however does not apply to the method that uses total energy of the decay positrons which will be described in detail in the next chapter.

2.3 Magnetic Field Measurement

The other quantity which is measured in the experiment is the magnetic field in the storage volume as seen by the stored muons. The magnetic field is measured by using pulsed proton nuclear magnetic resonance (NMR) in which the Larmor precession frequency of protons in water samples are determined. The magnetic field is given in terms of the precession frequency at a reference temperature, T, by the following expression

$$B = \frac{\hbar \tilde{\omega}'_p(T)}{2} \tag{2.19}$$

The stability of the magnetic field in the storage volume is achieved by NMR magnetometer devices which feedback the magnet current supply. Additionally, the localized fine tuning of the field is done by *shimming* in which movable magnet pieces are
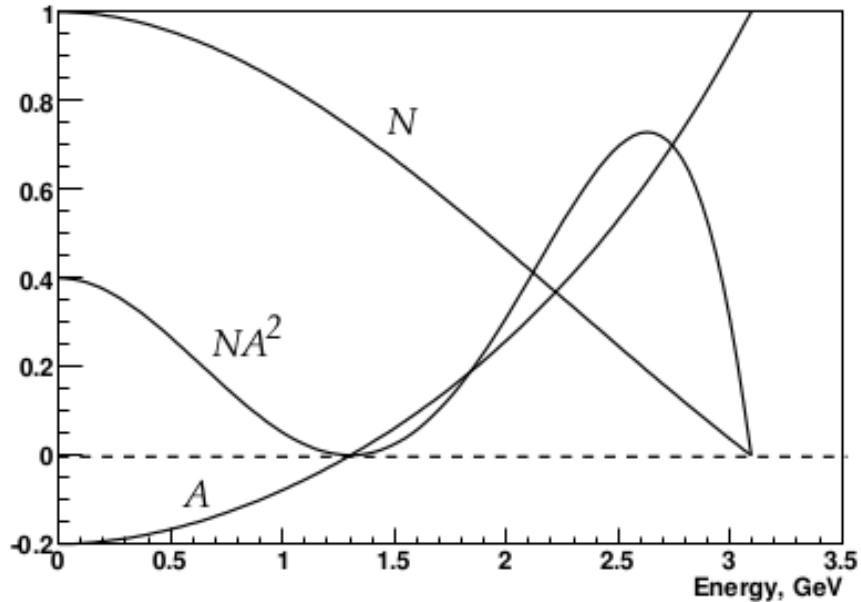
Figure 2.4: Plot showing count of high energy positrons, N, asymmetry, A and NA^2 versus energy. The statistical uncertainty on ω_a can be minimized by maximizing NA^2.

used[60].

To measure the precession frequency ω_p, there are 17 NMR probes mounted on a movable trolley. The trolley is driven around the ring every 3 days between the data taking intervals to map the magnetic field in the storage volume. Moreover, there are 378 fixed probes spread across 72 azimuthal locations in the ring that continuously measure the magnetic field. The measurements recorded by the trolley probes and the fixed probes are combined to determine the magnetic field versus position and time in the storage volume. Finally, this magnetic field value determined in terms of proton precession frequency is weighted by the distribution of muons in the beam averaged over time and space to obtain $\tilde{\omega}_p$ in equation 2.11.

2.4 Experimental Setup

The basic experimental setup of the new Fermilab Muon g-2 experiment is same as that of the BNL g-2 experiment (E-821) with major upgrades to improve precision of a_μ measurement to reach the planned goal. It consists of a superconducting storage ring magnet with radius 7.112 m and magnetic field strength of 1.45 T as shown in figure 2.6. A positive muon beam orbits the ring and decays into positrons in presence of a vertical magnetic field. The muon beam is constrained in the storage region with the help of an Electrostatic Quadrupole (ESQ) System. The decay positrons are
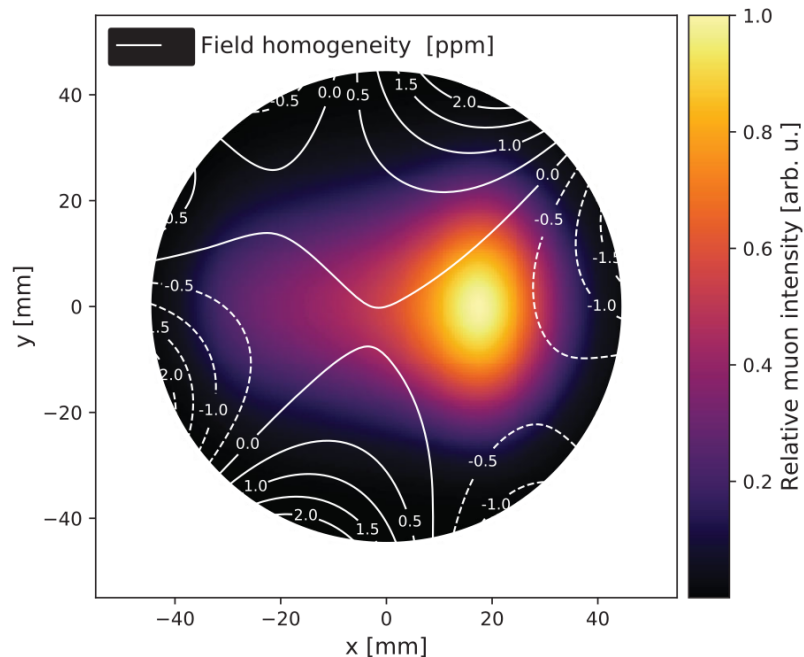
Figure 2.5: Figure showing magnetic field contours and azimuthally averaged muon population distribution in E-989 Run-1.

detected by electromagnetic calorimeters located on the inner side of the ring. A detailed description of each of the components of the experimental setup is given in the next subsections.

2.4.1   Production of Muons

The process starts with a beam of H^- ions accelerated by the linear accelerator, *Linac*, to a kinetic energy of 400 MeV. This ion beam is passed through a stripping foil to remove electrons to obtain a beam of protons. The *Booster*, which is a type of synchrotron, accelerates the protons to kinetic energy of 8 GeV and produces 4×10^{12} protons per batch. After this the *Recycler* bunches the beam into 4 bunches of 10^{12} protons each and one batch at a time is extracted out of the Recycler. The proton beam collides with a pion production target which is made up of nickel-iron alloy. The secondary beam produced at the target is collected using a lens. Following this, the positively charged particles with energy ∼3.11 GeV are selected using a bending magnet. The M2 and M3 beamlines are equipped to capture muons with energy 3.09 GeV which corresponds to the magic momentum described in section 2.1 which decay from the pions. The pions have spin zero and their decay products, muons and muon neutrinos, are spin 1/2 particles and are preferentially left handed. This is how a muon beam is produced with high longitudinal polarization. The muon beam is then sent to the Delivery Ring (DR) where it undergoes few revolutions during the course of which all the pions decay into muons. Finally the muon beam is sent to the $g - 2$
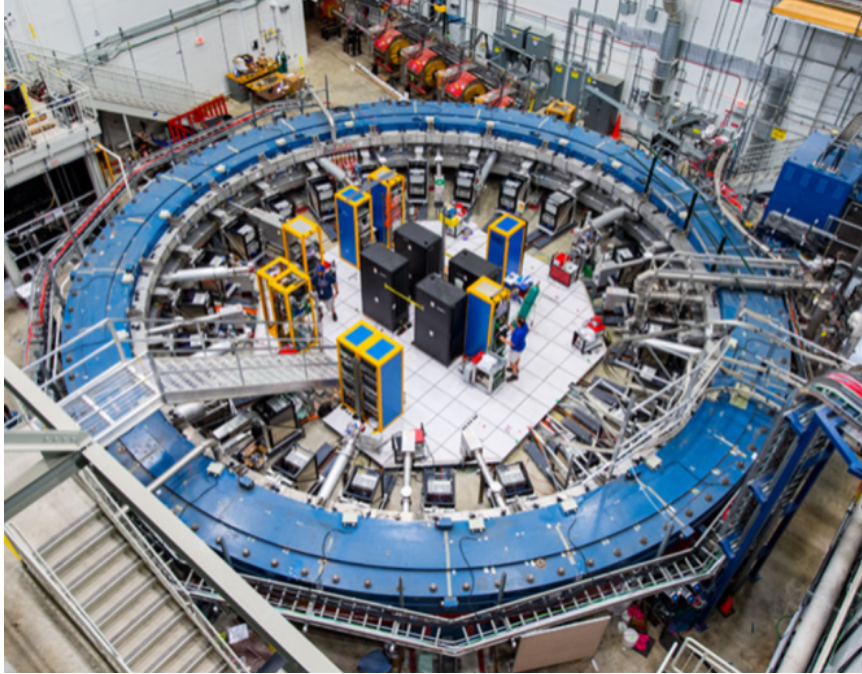
Figure 2.6: A photograph showing the storage ring for the Muon g-2 experiment at Fermilab. The muons enter the storage ring at the top right corner shown in red. The storage ring itself is blue in color with various detectors located at the inner side of the ring. Particularly, the 24 boxes can be seen on the inner side of the ring which are the calorimeter detectors.

storage ring after being extracted through M4 and M5 beamlines at a rate of 16 muon fills every 1.4 seconds as shown in figure 2.7 [49].
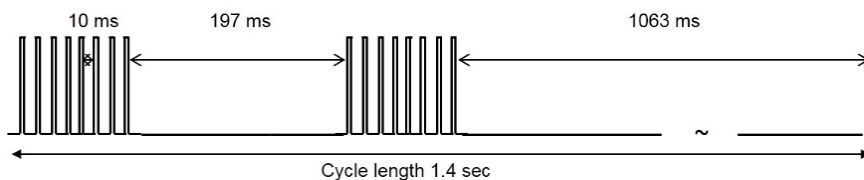
Figure 2.7: This figure shows a schematic representation of time structure of beam pulses to g-2 storage ring [48]. 16 muon fills, on average 10 ms apart, are delivered to storage ring every accelerator super-cycle (1.4 s).

2.4.2 Muons in the Storage Ring

The storage ring is a region of vacuum where the muons decay into positrons in the presence of a vertical magnetic field. The storage ring comprises an arrangement of superconducting coils and an iron yoke in order to produce a uniform 1.45 T vertical
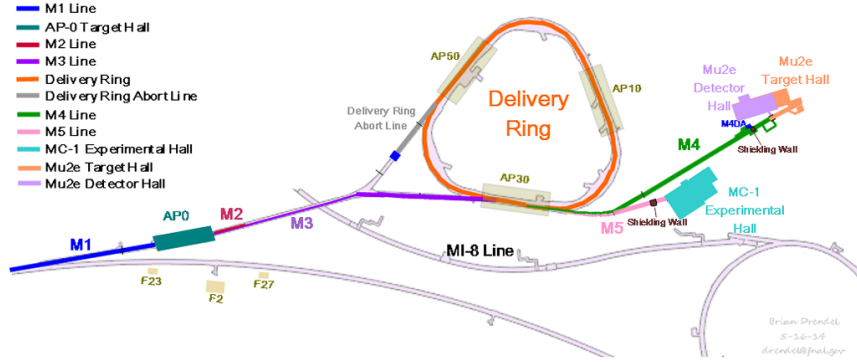
Figure 2.8: This figure shows a schematic representation of production and journey muon beam within Fermilab starting from 8 GeV proton beamline in M1 ending with muon beam at MC1 where the storage ring is located [49]

magnetic field. Figure 2.9 shows a schematic representation of the different components of the ring. The muons enter the ring at the inflector which is a magnet that provides a field free region for the muons to enter the ring. Then there are three kicker plates that produce a transient magnetic field to kick the muon beam onto the optimum orbit. There is also an ESQ system to hold the beam in the storage region by providing a restoring force in vertical direction. This is provided by the four sets of electrostatic quadrupole plates located around the ring.

The muons decay into positrons which are detected in the calorimeters as they produce Cherenkov radiation. There are 24 calorimeters located on the inner side of the ring. They are connected to SiPMs which generate voltage signals corresponding to the light pulses. These voltage signals are then digitized and processed for analysis of the spin precession frequency of the muons.

T0 counter

The $g-2$ storage ring is equipped with a laser monitoring system which is used for a lot of crucial tasks like calibration. One of the most important functions of the laser system is time synchronization. The analysis of muon spin precession frequency is critically dependent on time and it is necessary to have precise knowledge of beam injection time. For this, the laser system fires a sync pulse before injection of each muon fill. However this is not enough for a precise knowledge of beam injection time as there is a changing unknown offset between the sync pulse time and the muon beam injection time. Therefore a $T0$ counter is installed at the point of beam entrance (see subsection on Inflector magnet) which is a scintillator connected to SiPMs. The T0 produces a linear response to the primary beam pulse and the SiPMs produce a signal corresponding to the pulse which is then digitized[48].
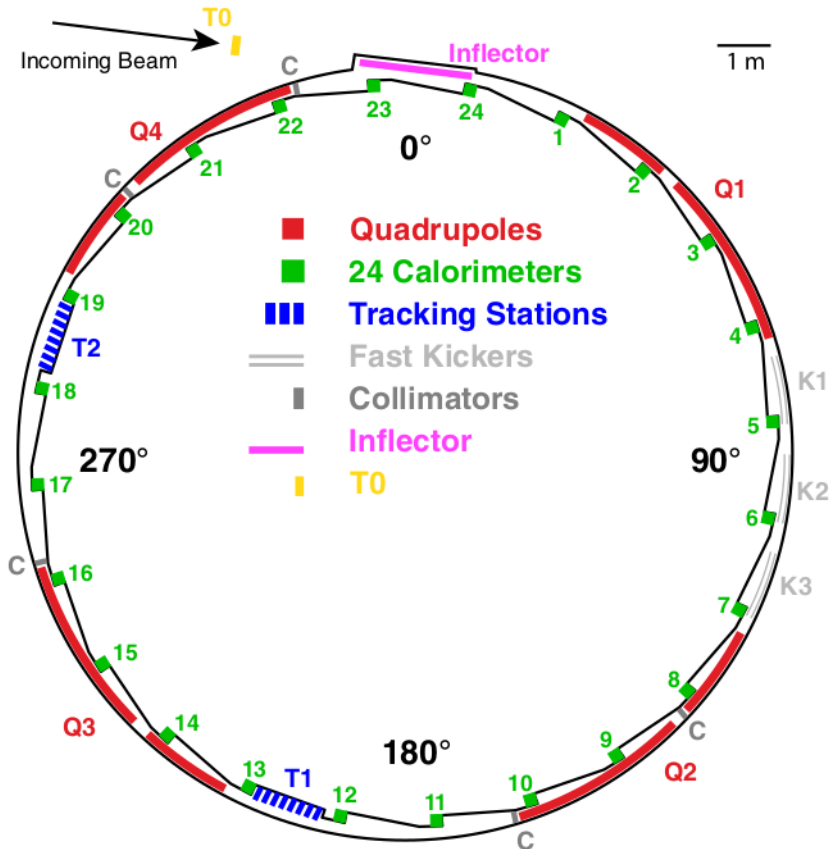
Figure 2.9: This is a schematic representation of the equipment present in the storage ring. Different colors show various detectors as marked in the figure

Inflector

Muons enter the storage ring through a hole in the storage ring magnet and the *inflector* delivers the beam to the edge of the storage region as shown in figure 2.10. The inflector is a superconducting magnet that cancels the dipole field of the storage ring and provides an almost field free region. The inflector from E-821 was refurbished for use in E-989 data taking. It's novel geometry of the discrete superconducting currents as shown in figure 2.10 prevents leak of magnetic flux and a superconducting shield also reduces disturbances to the magnetic field of the storage region [51].

Kicker

After the muon beam entrance to the storage region is facilitated by the inflector magnet, the beam is still not centered on the ideal orbit. To achieve the ideal beam positioning, three additional plates are installed in the storage region, called the *kicker plates* which produce a transient magnetic field. These are 1.27-m-long non-ferric aluminum electromagnets that are pulsed at current values 3-4 kA. These magnets
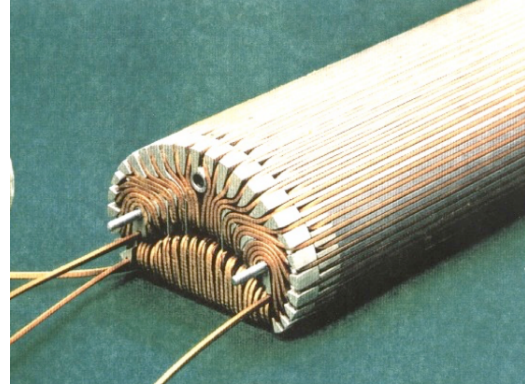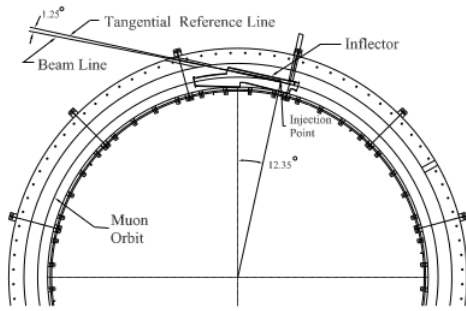
Figure 2.10: Figure on the left is a diagrammatic representation of the position of the inflector magnet at the point of muon beam injection in the storage ring. Figure on the right shows a photograph of the inflector magnet.

kick the muons onto the stable orbit necessary for the measurement of a_μ. A schematic representation of the kick is shown in figure 2.11 [50].
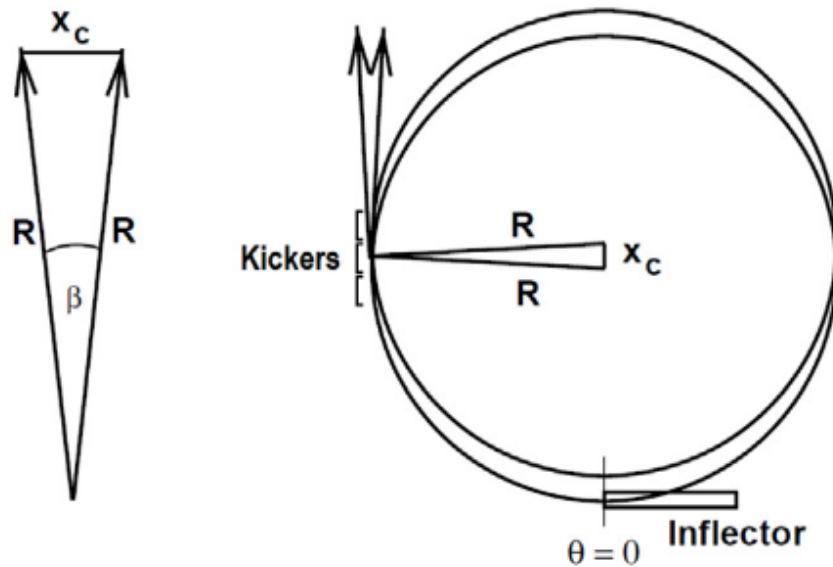
Figure 2.11: The beam enters the storage region at $\theta=0$ and it crosses over to the storage region at $\theta=\pi/2$. At this point the kickers deflect it onto the stable orbit.

Collimators

Collimators are five copper rings located inside the storage ring that are used to define the beam cross-section in the storage region. The muons which are outside of the storage region hit the collimators, lose their energy and are eventually lost from the

storage region. These lost muons can sometimes be detected along with the positrons in the calorimeters and thus a correction is applied to account for these events. The lost muon correction technique will be discussed in detail in the next chapter.

ESQ System and Betatron Oscillation

As mentioned before, the dipole magnetic field is not enough to constraint the beam in the storage region as it can only exert force in the radial direction. So an electrostatic quadrupole field is needed for a restoring force in a vertical direction. This is acheived by the four pairs of high voltage quadrupole plates inside the ring as shown in figure 2.9. As the muon beam enters the ring, the electrostatic quadrupole plates are charged asymmetrically to force the beam edges to be confined inside the region of cross section defined by the collimators. This is called *scraping*. After $\sim 7~\mu s$, [52] the quad plates are charged symmetrically to their nominal voltage for long term storage of the muon beam.

The quad plates along with the vertical magnetic field provide a linear restoring force in the radial direction. As a result of restoring forces in vertical and radial directions, the muons in the storage region undergo harmonic motion given by

$$x = x_0 + A_x cos(\sqrt{1-n}\frac{s}{R_0}) \tag{2.20}$$

and

$$y = A_y cos(\sqrt{n}\frac{s}{R_0}) \tag{2.21}$$

where s is the arc length, R_0 is the radius of the ring, n is the field index

$$n = \frac{kR_0}{vB_0} \tag{2.22}$$

and A_x and A_y are the amplitudes of oscillations in horizontal and vertical directions. These oscillation are called betatron oscillations. The horizontal and vertical betatron frequencies are defined in terms of cyclotron frequency, f_c, as

$$f_x = f_c\sqrt{1-n} \tag{2.23}$$

and

$$f_y = f_c\sqrt{n} \tag{2.24}$$

Calorimeters

Each of the 24 (numbered 1 to 24 in figure 2.9) calorimeters is a two dimensional array of Lead Fluoride (PbF_2) crystals. The positrons decaying from the muons curl inward and hit the face of the calorimeter as shown in figure 2.12. PbF_2 is an excellent medium for producing Cherenkov radiation[54] and owing to its high density and low radiation length its well suited to build a compact calorimeter detector. As the positrons pass through the PbF_2 crystals, they produce a shower of Cherenkov

photons. The crystals are connected to Silicon Photomultipliers (SiPMs) which produce voltage pulses proportional to detected photons. This signal is then digitized using an electronic waveform digitizer which is then processed and saved by the Data Acquisition System (DAQ). This process happens continuously for 700 μs after the beam injection and samples are recorded at a rate of 800 Mega-Samples per second (MSPS).
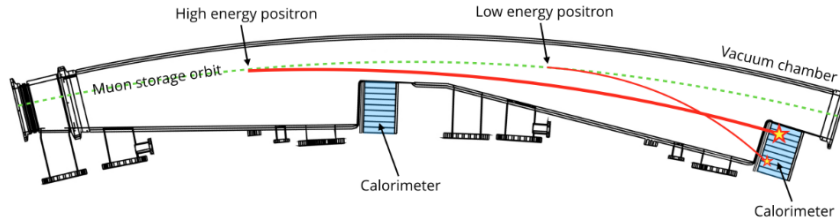
Figure 2.12: Figure illustrating detection of decay positrons in the electromagnetic calorimeters in the storage ring.

Tracker

There are two stations in front of calorimeter 12 and 18 where trackers are installed. These are made up gaseous ionization straw chambers which are used to reconstruct the profile of the muon beam during the fill period. As the decay positrons pass through the straw chambers before hitting the calorimeters, the straw chambers in the tracker produce a current which can be digitized. Each tracker has 8 modules with 128 straws per module. The trackers provide useful information about beam profiles, beam oscillations and decay positron momentum hitting the calorimeters [53].

2.5 Data Acquisition System (DAQ)

All the signals produced in different detectors have to be saved in real time for offline analysis which is done by the DAQ. Each calorimeter as well as the other detectors are connected to a μTCA crate. The voltage signals produced in each calorimeter are digitized using a five channel waveform digitizer, WFD5 contained within the μTCA crate[55]. The WFD5s are compatible with AMC (Advanced Mezzanine Card) and are connected to AMC13 modules designed by Boston University for CERN CMS experiment[56]. The AMC13s distribute the clock signal within the μTCA crate, facilitate readout of AMCs within the crate and transmit data to the DAQ frontend computers. The Clock and Controls Center (CCC) has a 40 MHz clock for digitization and it encodes the clock signal and beam trigger using Timing, Trigger, and Control (TTC) protocol developed for the CERN Large Hadron Collider experiments[57].

Each WFD5 digitization channel comprises a 12-bit, 800 MSPS Analogue-to-Digital Converter (ADC) chip for the digitization of the SiPM signal. The 800-MHz clock for the WFD5 module derives from the 40-MHz master clock used for CCC digitization. The AMC13 has an *event builder* which collects the data from all the WFD5 modules from a calorimeter and sends that to a DAQ frontend computer over a 10-Gb Ethernet link. The readout and pre-processing of the continuously digitized waveforms from the detector system is done by the frontend computer while the back-end computer is responsible for the event assembly, data storage, and run control[55].

The readout in the frontend machine parallelizes the process using GPU (Graphical Processing Unit) multicore processing. The process consists of a TCP thread that receives and re-assembles the raw data from the AMC13 controller, a GPU thread that manages the GPU-based data processing into various derived datasets, and a MIDAS thread that handles the transfer of MIDAS-formatted events to the back-end computer event builder. MIDAS is a DAQ environment originally developed at PSI and TRIUMF[58]. To facilitate efficient multithreading, Mutual exclusion (Mutex) locks are used to make sure that the threads take turns while accessing the same resources. The ADC samples from each of the 54 crystals are recorded when they exceed a pre-set threshold, typically equivalent to ~ 50 Mev. The MIDAS tools for event building, data storage, and run control are all performed on the backend computer. MIDAS also provides an online database (ODB) used for cataloging and manipulating the parameters for data taking during the course of running the experiment[55].

The DAQ in E-989 processes data from 1296 calorimeter channels (54 channels per calorimeter), two straw tracker stations, auxiliary detectors, the kicker, ESQs and NMR probes. The experiment acquires raw ADC samples at a rate of 20 GigaBytes per second. By implementing CUDA (Compute Unified Device Architecture) codes for parallel processing of data using GPUs in the frontends, the rate at which the data gets written in the tape is reduced by a factor of 100 that is 200 Megabytes per second[59].

2.6 E-field and Pitch Correction

Although the Lorentz factor, γ, in equation 2.7 is chosen such that the electric field term vanishes, in an experimental setup this cannot be perfectly achieved. There is always a spread in the momentum of the muon beam that leads to a small contribution from the E-field. This is called the *E-field* correction. This is true in the experimental setup of E-989 and equation 2.7 can be written in terms radial E-field, E_r, as [48]

$$\omega_a' = \omega_a[1 - \frac{\beta E_r}{cB_y}(1 - \frac{1}{a_\mu \beta^2 \gamma^2})]$$

(2.25)

where $\omega_a = -a_\mu eB/m_\mu$, B_y is the vertical component of the dipole magnetic field and $\beta(= v/c)$ is the muon's velocity in the ring. Thus the fractional change in ω_a due

E-field correction is

$$\frac{\omega_a' - \omega_a}{\omega_a} = \frac{\Delta\omega_a}{\omega_a} = -\frac{2\beta E_r}{cB_y}\left(\frac{\Delta p}{p_0}\right) \tag{2.26}$$

This correction after some manipulations is given by

$$\frac{\Delta\omega_a}{\omega_a} = -\frac{2\beta^2 n(1-n) < x^2 >}{R_0^2} \tag{2.27}$$

where $< x^2 >$ is time averaged equilibrium beam position and R_0^2 is the radius of the ring. The correction is directly applied to ω_a and reduces its value owing to the negative sign [48].

As described in section 2.4, the muon beam in the storage ring undergoes betatron oscillation, f_y, and as a result the condition that muon velocity $\overrightarrow{\beta}$ is orthogonal to the dipole magnetic field, $\overrightarrow{\beta}.\overrightarrow{B} = 0$, does not hold. The angle between the muon momentum and the horizontal axis, ψ, also called the pitch angle, undergoes oscillation [48]

$$\psi = \psi_0 \cos(\omega_y t) \tag{2.28}$$

This effect is requires a *pitch correction* to the measured ω_a. Equation 2.7 is modified to include this effect as follows [48]

$$\overrightarrow{\omega_a'} = -\frac{e}{m_\mu}[a_\mu \overrightarrow{B} - a_\mu(\frac{\gamma}{\gamma+1})(\overrightarrow{\beta}.\overrightarrow{B})\overrightarrow{\beta}] \tag{2.29}$$

Rewriting $\overrightarrow{\beta}$ and $\overrightarrow{B}$ as $\overrightarrow{\beta} = \beta\cos\psi\hat{z} + \beta\sin\psi\hat{y}$ and $\overrightarrow{B} = B_y\hat{y}$, where $\hat{y}$ and $\hat{z}$ denote the vertical and horizontal directions, the transverse component of ω_a, $\omega_\perp$ can be written as [48]

$$\omega_\perp = \omega_{ay}'\cos\psi - \omega_{az}'\sin\psi \approx \omega_a[1 - \frac{\psi^2}{2}] \tag{2.30}$$

The vertical betatron frequency ω_y is one order of magnitude larger than ω_a and as a result, the parallel component of ω_a, $\omega_\parallel$, changes its sign within a cycle of ω_a modulation. This leads to cancellation of $\omega_\parallel$ when a time average of these quantities is taken into account. So pitch correction contribution to ω_a only comes from its transverse component $\omega_\perp$. After some algebraic manipulation, time averaged contribution of pitch correction is [48]

$$C_p = -\frac{n}{4}\frac{< y^2 >}{R_0^2} \tag{2.31}$$

where $< y^2 >$ is the time averaged mean-squared vertical position of the muon beam [48].

Chapter 3 Energy Integrated Reconstruction and Run-1 Analysis

3.1 Motivation

Experimental determination of Muon $g - 2$ is a precision measurement and it is important to validate its accuracy. Traditional determination of muon's anomalous spin precession frequency by counting high energy, above threshold positrons is susceptible to systematic biases. One important source of bias is called pile-up in which a distortion to positron time distribution is caused by misidentification of two or more positron event as one. This can happen when two positron events overlap in time in the calorimeters. Another source of systematic effect comes in due to change in the SiPM voltage signal amplitudes as a result of the detector response, called gain. Bias from gain can cause systematic early-to-late effects. For an unbiased analysis of the precession frequency data, algorithms are developed to identify and mitigate these effects, but these are still significant source of systematic uncertainty in the precession frequency result. Hence it becomes important to perform parallel analyses which would measure the same physical quantity but would have a very different sensitivity to these systematic effects.
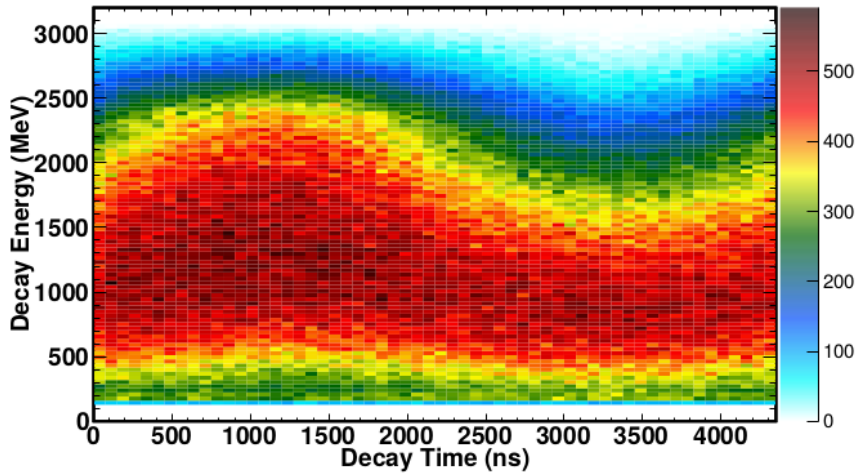
Figure 3.1: Anomalous precession frequency modulation of the decay positron energy. Image credit [48]

One such analysis technique is called Energy Integrating analysis. This is a minimum threshold analysis which does not count high energy positron events, but instead records the energy deposited by the positrons in the calorimeters. Like the number of high energy positrons, the total energy of the decay positrons also changes as a function of the angle between muon's spin and momentum. The muons in the storage ring are longitudinally polarized (spin and momentum are anti-parallel in case of positive

32

muon) as explained in chapter 2. Muons decay into positrons, muon anti-neutrinos and positron neutrinos. Since muon's spin direction is changing with respect to its momentum due to its spin precession, we obtain a modulation in total energy of the decay positron due to its changing energy with spin precession as a result of parity violating weak decay.

As a result, continuous digitized waveforms corresponding to total SiPM currents which are in turn directly proportional to the integral of the energy deposited by the positrons, will also have modulation by the anomalous precession frequency. This method is called the Q-method where Q stands for total charge. The Q-method, having a low threshold, has significantly different sensitivity to the systematic effects coming from gain and pile-up and thus is a crucial parallel analysis to confirm the robustness of experimental determination of the precession frequency in Muon $g - 2$ experiment. Although in effect, application of a small threshold of a couple of hundred MeV is necessary to cut out the region of noise, it is still less sensitive to gain fluctuations. Additionally, since this technique does not require identifying each positron event correctly, it avoids biases resulting from pulse fitting or pulse clustering that are done in positron counting methods. For the same reason, it is largely insensitive to first order pile-up effects. It does suffer from small over/under-estimation of pulse energies, but the overall sensitivity to pile-up is still significantly less than the traditional positron counting method due to the low threshold. The next sections describe the reconstruction of the precession frequency signal for Q-Method analysis.

3.2   Digitized Waveforms in DAQ

Q-method utilizes continuous digitized waveforms in units called ADC (Analogue-to-Digital Converter) values which are proportional to the energy deposited in individual crystals by the decay positrons. These ADC samples are collected as a function of time in bins of pre-defined widths. Each of the 54 (9 by 6) PbF_2 crystals in the calorimeters record digitized waveforms in ADC values as a function of time as shown in figure 3.2.

The smallest bin-width possible with a 800 MSPS data collection rate, as described in chapter 2, is 1.25 ns. However, considering the enormous data rate and limited storage capacity for continuous digitized samples as opposed to the chopped islands that are recorded in positron counting methods, the time bins are decimated by some integer factor greater than 1. Moreover, for the same reason the end time for a Q-method fill is less than T-method and several of the muon fills are combined together into a single unit called *flush* to achieve additional data compression. Table 3.1 shows these DAQ parameters for Run-1 through Run-5. In Run-1, the Q-method signal was recorded in raw time bins of width 75 ns. This was changed in Run-2 and Run-3 to be able to see higher frequency modulations and their effects in the data. The raw bin width for Run 2 and 3 was 18.75 ns.
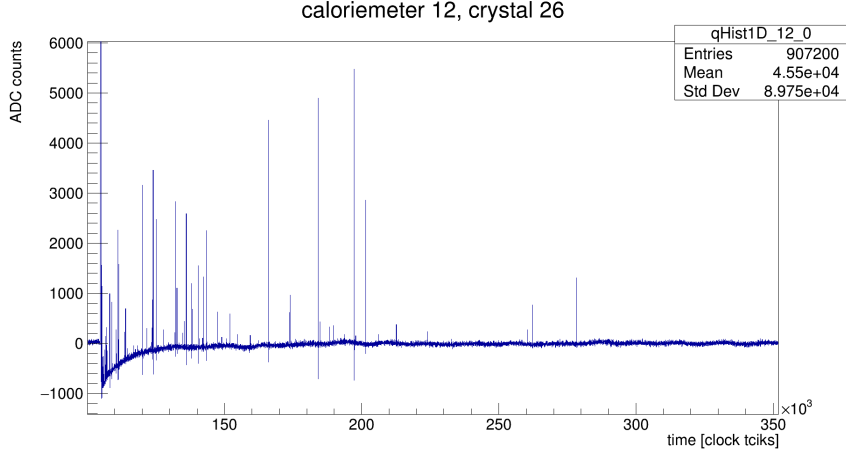
Figure 3.2: ADC signal recorded in 1 flush of a single crystal from dataset 2C

Table 3.1: DAQ configuration parameters for Q-method data collection versus run period

Run Period	Start time	End time	Time Decimation Factor	Muon fills per flush
1	-6 μs	232 μs	60	1
2	-6 μs	309 μs	15	4
3	-6 μs	309 μs	15	4
4	-6 μs	556 μs	30	4
5	-6 μs	556 μs	30	4

3.3 Background Subtraction

The muon beam injection at early time in a fill causes a large radiation flash in the calorimeter which is recorded as a huge pulse followed by a big undershoot due to the detector response. This introduces an early-to-late drift in the pedestal. To be able to clearly see the modulation by ω_a, this effect needs to be removed. To achieve this a background subtraction algorithm is implemented. In this, for a pulse at each time bin, called the *trigger* sample, an average pedestal is calculated which is then subtracted from the ADC value of that pulse. The average is a rolling value which is calculated for an island around each trigger pulse. This island is called the *pedestal window*. With Run-1 DAQ configuration, the pedestal window was chosen to be 4 bins on each side of the trigger pulse with a gap of one bin. This gap is necessary to account for the undershoot due to the detector response after each trigger pulse. It is also necessary to choose the width of the pedestal window to be a multiple of the cyclotron frequency time period (T_c) to eliminate the effects of pedestal bias due to it. T_c in Fermilab storage ring is ~ 149.2 ns. With time decimation factor being 60, the pedestal window of 4 bins amounted to a time window of 300 ns which roughly

twice T_c and hence successfully suppressed any effects coming from it.
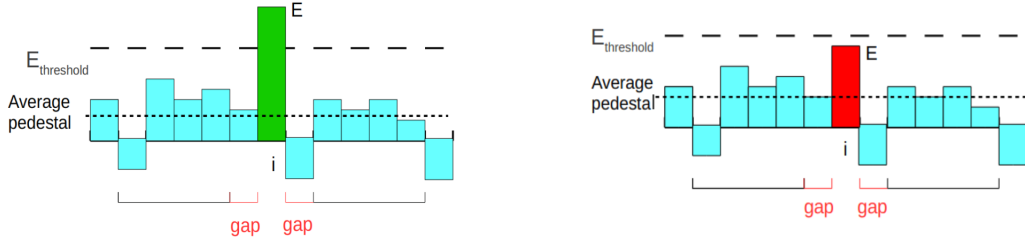
Figure 3.3: Illustration of pedestal subtraction algorithm. The pulse in green color depicts an above threshold trigger sample while the pulse in red color is an example of below threshold trigger sample. The pulses in cyan are the pedestal samples and contribute to average pedestal calculation. The pedestal samples adjacent to the trigger pulse are rejected from average pedestal calculation.

The pedestal subtracted trigger pulse energy is then compared against a small threshold, called *absolute threshold*, which is chosen for each DAQ configuration empirically. The threshold is the energy value which cuts out the average ADC noise coming from the digitizers. This is typically found to be about a couple of hundred MeV and ω_a has no systematic dependence on this empirically chosen value. If the pedestal subtracted energy value is found to be above threshold, it is saved as signal pulse and otherwise it is discarded as noise.

3.4 Noise Handling

To handle above average noise in the crystals, a rolling threshold is introduced. Average noise is calculated for a region chosen near the end of a fill since this region has less probability of having a positron pulse. The standard deviation of the average noise distribution is calculated per crystal. The rolling threshold is calculated by multiplying a *threshold multiplier* chosen empirically with the standard deviation of this calculated average noise. If the rolling threshold is found to be above the absolute threshold, then it becomes the absolute threshold. This raising of the absolute threshold happens very rarely, typically only in case of crystals with excessive noise.

3.5 Construction of Q-Method Time Spectrum

After applying the pedestal subtraction algorithm, the signal pulses need to be converted to meaningful energy units. This is achieved by using energy calibration constants. Additionally, there are two gain corrections that need to be applied to account for early-to-late distortion of signal due to the undershoot of the pedestal happening at the time of injection of the muon beam as a result of the detector response and also due to long term environmental fluctuations.

3.5.1 Energy Calibration

The signal is recorded in units of ADC and should be converted to MeV to report analysis results in meaningful physical units. The energy calibration constants were derived by aligning energy scales of the calorimeter channels relative to each other by using the lost muons energy and the absolute scale was set by doing a 5-parameter T-method fit to the per calorimeter data. The threshold value which gives maximum statistical power, NA^2, and minimum fitted error on ω_a is set to be 1.7GeV. [61].

3.5.2 In-fill Gain Correction

As mentioned before, the calorimeters experience a splash of particle at the time of muon injections causing the baseline to experience a big undershoot. As the recovery from this flash of beam happens, the shape of the baseline undergoes a change during the course of a muon fill which can in turn introduce a time dependence on the precession frequency phase. This can result in a systematic bias in determination of ω_a. To correct for this, a fixed number of laser pulses are fired during each muon fill. The time interval between subsequent pulses is made to vary such that drift in the baseline up to several hundred microseconds is captured by the laser calibration. The change in the amplitude of these laser pulses are then used to construct in-fill gain (IFG) function

$$f_{IFG}(t) = 1 - A_{IFG}e^{-t/\tau_{IFG}} \tag{3.1}$$

which is applied to the positron signal for each muon fill[62].

3.5.3 Out-of-fill Gain Correction

Out-Of-Fill Gain (OOFG) or the long term drift correction is the correction associated with the change in SiPMs' gain in response to environmental fluctuations like temperature. To determine this correction, laser pulses are fired in the calorimeters in the absence of muons and the SiPM responses are recorded. The ratio of the fired laser signal amplitudes and the recorded signal amplitudes are then used to calculate the long term gain effects for the positron signal. These constants are calculated by averaging over a *sub-run* which is roughly equivalent to 5 seconds of running[63].

3.5.4 Pedestal Ringing

Since, Q-method uses continuous waveforms of the digitized data, it is affected by any changes in the pedestal. One such effect is the ringing of the pedestal. The source of this ringing is thought to be oscillation of the digitizer electronic equipment after the beam injection and it is only seen in the early time of the fill [67] after which it dies out as shown in figure 3.4. A data driven multiplicative correction was applied to the histograms to correct for this effect.
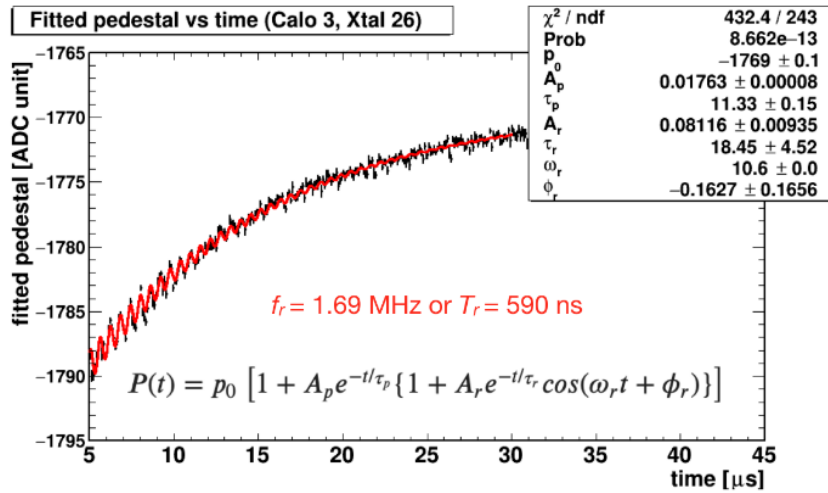
Figure 3.4: Ringing of the pedestal in Run-1 [67] at early times in raw data (before pedestal subtraction).

3.6 Run-1 Analysis

After applying the calibration and correctional constants, the signal histograms from the 1296 (54x24) channels are added together and multiple muon flushes are stacked up to give the wiggle histogram that goes into the ω_a analysis, shown in figure 3.5. The x-axis units are in clock-tick which is roughly equal to 1.25 ns. The time, $t = 0$ should be also assigned at this point and it is typically chosen to be bin which corresponds to the peak of the flash at the time of muon beam injection.
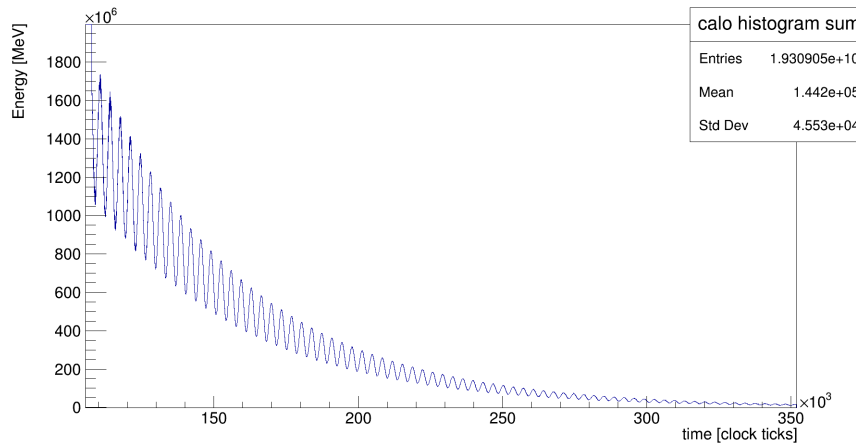
Figure 3.5: Background subtracted, out-of-fill and in-fill gain corrected and energy calibrated positron energy histogram for a subset of Run 2C

37

3.6.1 Assignment of Bin Uncertainties

The contents of the bins is the sum total of the energy hits at that time in fill and the uncertainty comes from statistical uncertainty in the number of pulses that went into that bin, Δn_i, and also the statistical variation from the energy resolution in those pulses, E_i. The fluctuation in the energy value is considered to be a small contribution and is ignored in the uncertainty calculation. The total energy in a time bin of per calorimeter wiggle histograms given by

$$E_{total} = n_1 E_1 + n_2 E_2 + n_3 E_3 + ... \tag{3.2}$$

Ignoring the contribution from the fluctuation of energy per pulse, ΔE_i, the uncertainty for the corresponding bin would be

$$\Delta E_{total} = \sqrt{(E_1 \Delta n_1)^2 + (E_2 \Delta n_2)^2 + (E_3 \Delta n_3)^2 + ...} \tag{3.3}$$

Assuming Poisson statistics and $\Delta n_i = \sqrt{n_i}$,

$$\Delta E_{total} = \sqrt{(E_1 \sqrt{n_1})^2 + (E_2 \sqrt{n_2})^2 + (E_3 \sqrt{n_3})^2 + ...} \tag{3.4}$$

This is approximated as

$$\Delta E_{total} = \sqrt{(E_1)^2 + (E_2)^2 + (E_3)^2 + ...} \tag{3.5}$$

where the effects from *pulse splitting*, that is sharing of a pulse energy between adjacent time bins, are ignored.

3.6.2 Blinding of Anomalous Precession Frequency

Before the analysis of the precession frequency data, the data is blinded to mitigate any biases. This is done in two steps. First, there is a hardware blinding implemented at the digitization precision clock which has a frequency of 40 MHz. This clock is detuned to a secret value between 39 997 to 39 999 kHz unknown to the analyzers. In addition to this a software blinding is also implemented by each analyzer by introducing an offset ΔR unique to each analysis in the precession frequency such that

$$\omega_a = \omega_{ref}[1 - (R - \Delta R) \times 10^{-6}] \tag{3.6}$$

where $\omega_{ref} = 2\pi \times 0.2291$ MHz.

3.6.3 Correcting the Cyclotron Modulation

The temporal length of the muon fill entering the storage ring is 120 ns. The cyclotron frequency of the muon around the ring is 149.2 ns. As a result of this, each calorimeter sees a modulation of the precession frequency signal by the cyclotron frequency in the raw binned (binwidth=18.75 ns in Run-2 and 3) data as shown in figure 3.6. This is called *Fast Rotation* modulation. Before analyzing this data, groups of 8 bins are summed together to make the final bin width of the data to be 150 ns (18.75×8).

This is referred to as *rebinning* by a factor of 8. This washes out most of the effects of fast rotation. However, since the bin width is not exactly equal to the time period of the fast rotation, T_c, a beat frequency is observed at frequency $\sim \omega_c - \omega_b$, where ω_c is the fast rotation frequency and ω_b is the binning frequency.
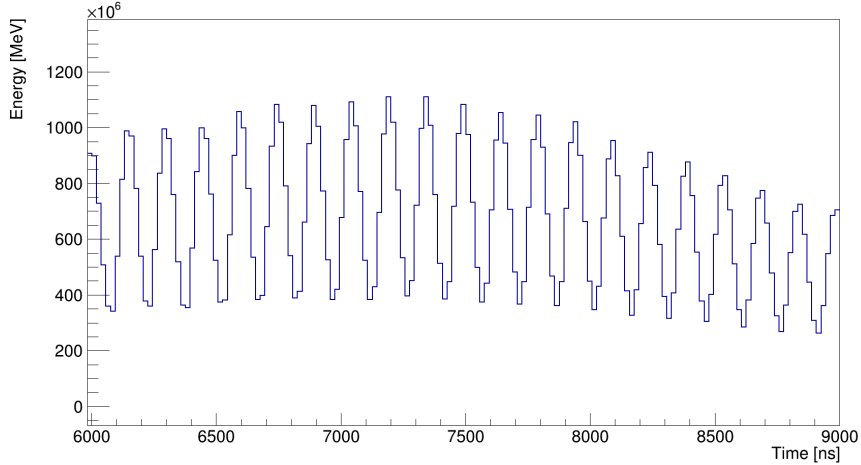
Figure 3.6: Q-method data from calorimeter 1 showing modulation by fast rotation signal at early times in Run-2 summed data

To handle this effect, a phase cancellation approach was adopted. First the data in raw 18.75 ns bins are rebinned by a factor of 4 to make the bin width equal to 75 ns. This is roughly half of T_c. Next, it is superimposed with a histogram which is shifted in time with respect to the first one by 75 ns such that the fast rotation has the opposite phase in the shifted histogram. This cancels out the fast rotation phase as shown in figure 3.7.
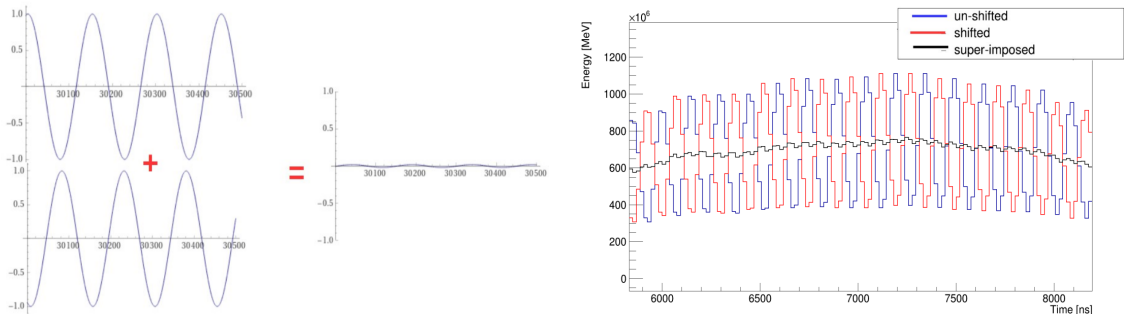
Figure 3.7: Figure on the left shows a toy model of fast rotation correction procedure; figure on the right shows the correction on Q-method Run-2 summed calorimeter 1 data, zoomed into early times (6 to 8 μs)

39

3.6.4 Fit Function

The wiggle histogram (figure 3.5) captures the total energy of the positron ensemble undergoing an exponential reduction at a rate given by the muon's decay lifetime in the storage ring. On top of the decay spectrum, there is a sinusoidal modulation due to the parity violating weak decay of the muons. Largely, a simple 5 parameter function which accounts for these two effects seems to model the data well.

$$f(t) = N_0 e^{(-\frac{t}{\gamma\tau})}(1 + A\cos(\omega_a t - \phi)) \tag{3.7}$$

Howver, after performing the fit when a fast fourier transform (FFT) of the difference between the fit-function and the data (fit-residuals) is produced, other effects begin to show up as peaks as shown in figure 3.8. This motivates the need to introduce additional terms in the fit-function to address these effects.
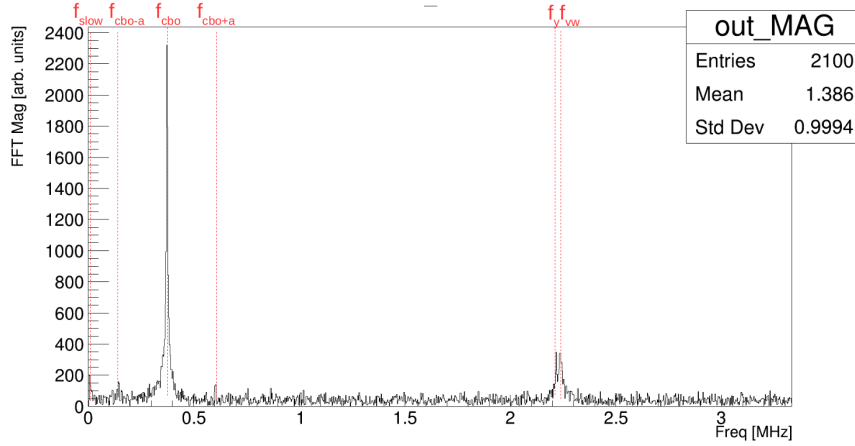
Figure 3.8: Fast fourier transform of the fit residuals showing various effects modulating the precession frequency signal. f_{cbo} is coherent betatron frequency responsible for the oscillation of muon beam in the radial direction. $f_{cbo\pm a}$ are the satellite peaks corresponding to the crossterm between cbo and the anomalous spin precession frequency. f_y and f_{vw} are the muon beam vertical mean oscillation and the vertical width oscillation respectively. f_{slow} is the freuquency corresponsing to the slow variation in the data.

Coherent Betatron Oscillation

As mentioned in chapter 2, the muon beam undergoes betatron oscillations in vertical and radial directions. There is a radial oscillation of the muon beam, given by $f_x = f_c\sqrt{1-n}$, where f_c is the cyclotron frequency [48]. Since the calorimeter arrangement in the experiment is discrete with 24 of them sitting on the inner side of the ring, the observed radial betatron frequency is an alias of f_x and f_c given by

$$f_{cbo} = f_c - f_x \tag{3.8}$$

40

as shown in figure 3.9.
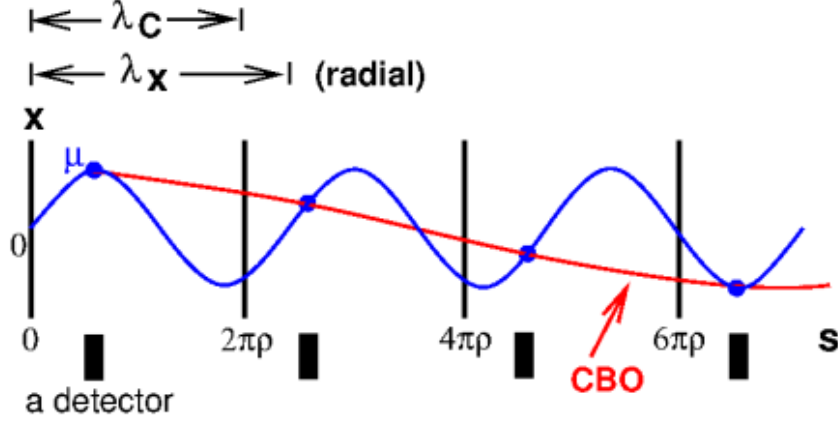
Figure 3.9: Aliasing effect of radial betatron frequency. The blue oscillation depicts the radial betatron oscillation. The black vertical lines denote the cyclotron frequency wavelength and the black rectangular block shows position of one detector. The observed CBO frequency as a result of aliasing in the detector is shown by the red line. (Image taken from [48])

The second harmonic of this frequency $f_{2cbo} = 2f_{cbo}$ is also observed in the FFT. This frequency f_{2cbo} is the oscillation of the radial width of the muon beam. Additionally, two satellite peaks at $f_{cbo} - f_a$ and $f_{cbo} + f_a$ corresponding to the product $cos(\omega_a t).cos(\omega_{cbo} t)$ (since the asymmetry and the phase are also modulated by the CBO frequency) are also observed.

Since, there is a spread in the momentum of the muon beam and the storage potential is not perfectly harmonic, the muon population undergoes the oscillation with slightly different frequencies and eventually decohere. The time constant for decoherence is roughly 250 μs [70]. Exponential functional forms are added to the fit-function to capture the modulation of normalization factor N, asymmetry A and the phase ϕ by CBO.

$$N_{cbo}(t) = 1 + A_{cbo_N} e^{-\frac{t}{\tau_{cbo}}} \cos(\omega_{cbo} t - \phi_{cbo_N}) + A_{2cbo_N} e^{-\frac{2t}{\tau_{cbo}}} \cos(2\omega_{cbo} t - \phi_{2cbo_N}) \quad (3.9)$$

$$A(t) = A_0(1 + A_{cbo_A} e^{-\frac{t}{\tau_{cbo}}} \cos(\omega_{cbo} t - \phi_{cbo_A})) \quad (3.10)$$

$$\phi_a(t) = A_{cbo_\phi} e^{-\frac{t}{\tau_{cbo}}} \cos(\omega_{cbo} t - \phi_{cbo_\phi}) \quad (3.11)$$

Due to damaged resistors in the ESQ system during the Run-1 data taking period the CBO frequency had a time dependence and the form of the CBO envelope had to be updated

$$\omega_{cbo}t \longrightarrow \omega_{cbo}t + A_1 e^{\frac{-t}{\tau_1}} + A_2 e^{\frac{-t}{\tau_2}} \tag{3.12}$$

The amplitude values, A_1 and A_2, and time constant values, τ_1 and τ_2, used were the ones that were directly measured by the tracker system.

Vertical Oscillation

Like radial oscillation, the muon beam also undergoes vertical oscillation. One of them is the oscillation of the mean and is given by

$$f_y = f_c \sqrt{n} \tag{3.13}$$

and is directly observed in the FFT. The vertical width of the beam also undergoes an oscillation called vertical waist motion. This frequency is again aliased like the f_{cbo} and the observed frequency is

$$f_{vw} = f_c - 2f_y \tag{3.14}$$

The envelopes for f_y and f_{vw} have decoherence times of roughly 100 μs and 30 μs respectively. The functional form of these two oscillations are

$$N_{vw}(t) = 1 + A_{vw} e^{-\frac{t}{\tau_{vw}}} \cos(\omega_{vw}t - \phi_{vw}) \tag{3.15}$$

$$N_y(t) = 1 + A_y e^{-\frac{t}{\tau_y}} \cos(\omega_y t - \phi_y) \tag{3.16}$$

Muon Loss

Some of the muons are lost from the storage region after hitting collimators or other obstacles. This leads to a beam energy loss and introduces bias in ω_a determination. Therefore, a correction must be applied to the fit-function to account for these losses. These muons can pass through the detectors as minimally ionizing particles (MIPs) and deposit energies ($\sim$ 170 MeV) in them. Additionally these muons can pass through one or more successive calorimeters. The time of flight between consecutive calorimeters is 6.25 ns. So, time and energy cuts are used to identify lost muons and construct their time spectra as shown in figure 3.10.

The correction term for this effect that goes in the fit-function has the following form

$$\Lambda(t) = 1 - K_{loss} \int_0^t e^{\frac{t'}{\gamma\tau}} L(t')dt' \tag{3.17}$$

where $L(t')$ is the loss time spectrum and K_{loss} is a fit parameter. Muons can be lost from the storage region either by decaying or by escaping. The integral $\int_0^t e^{\frac{t'}{\gamma\tau}} L(t')dt'$
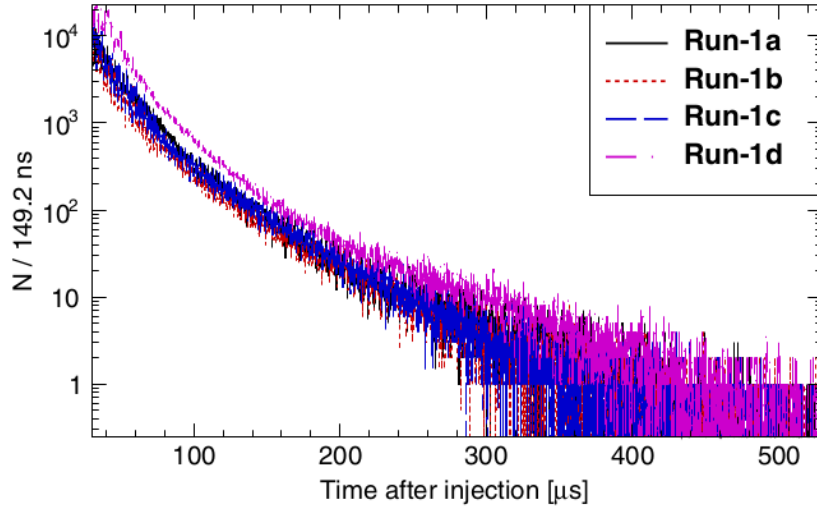
Figure 3.10: The integrated muon loss spectrum in Run-1

is the solution to the differential equation governing the number of muons present in the storage ring at any time following the beam injection[70]. This accounts for the loss in positrons that would have otherwise been present in their time distribution.

Slow Term

As mentioned before, the ESQ system in Run-1 consisted of two damaged resistors. Because of that, the RC time constant of the quadruple plates was found to be higher than designed. This led to a longer recovery period of the beam after scraping which in turn meant that the beam was moving vertically well into the fit time window of the flush. This significantly contributed to the slow effect peak in the FFT [68]. This can also be seen in the fit-residuals as shown in figure 3.11.
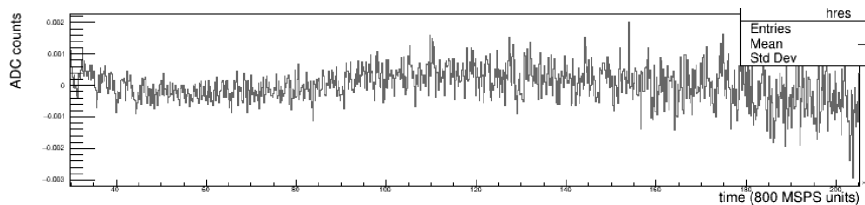
Figure 3.11: The fit residuals (difference between the data and the fit-function) from Run-1c showing the slow term modulation at early time [68]

The functional form for this effect in the fit function is

$$V(t) = A_v e^{-\frac{t}{\tau_A}} + B_v e^{-\frac{t}{\tau_B}} \tag{3.18}$$

43

where τ_A is a shorter time constant of $\sim 5\mu s$ while τ_B is a larger time constant of $\sim 200\mu s$. Another term was needed to account for the relaxation of the asymmetry parameter as a result of this vertical drift of the beam

$$A(t) \rightarrow A(t)e^{-\frac{t}{\tau_{relax}}} \tag{3.19}$$

where τ_{relax} is the time constant and is a fit parameter. This time constant was found to be quite large, of order of few milli-seconds. This relaxation was motivated by the drift of the asymmetry parameter with fit start time [69].

3.6.5 Fit Results

The Run-1 dataset consists of four sub-parts (1a, 1b, 1c and 1d) each with a different field index. The energy calibration and IFG and OOFG corrections were applied after pedestal subtraction. Fit start time for analysis was 30 μs, but it was changed to 50 μs in dataset 1d to minimize effects from the damaged ESQ resistors. An absolute threshold of 300 MeV was applied. The full functional form that was used to fit the datasets was

$$f(t) = N_0 e^{(-\frac{t}{\gamma\tau})} N_{cbo}(t) N_{vw}(t) N_y(t) \Lambda(t) V(t) (1 + A(t)cos(\omega_a t - \phi - \phi(t))) \tag{3.20}$$

Figure 3.12 shows a fit to summed Run-1 data and the FFT of the fit residuals for the same.
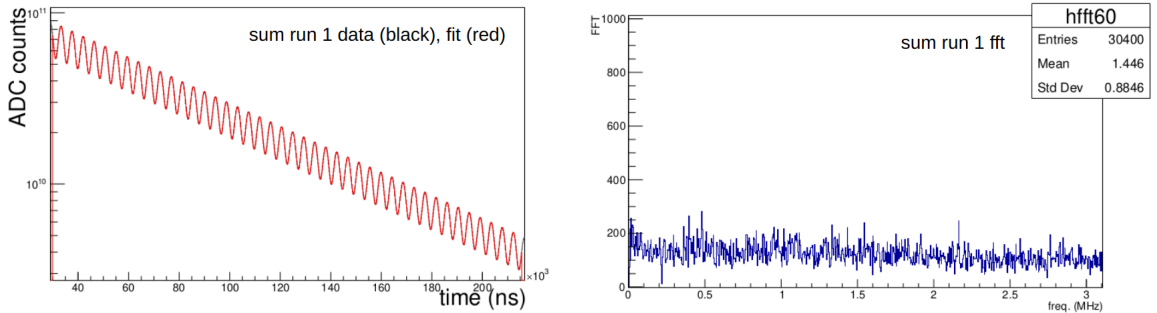
Figure 3.12: Figure on the left shows the fit to the summed Run-1 dataset while the figure on the right shows the fourier transform of fit residuals [71]

Fit results are summarized in the table 3.6.5. R values listed are unblinded values proportional to ω_a according to equation 3.6. The results of Run-1 analysis using Q-method demonstrated agreement with the other analysis and was within the allowed region of deviation. The statistical error bar on Q-method analysis was bigger than other analyses since it employs a minimal threshold and does not maximize its statistical power which can be achieved at around 1.7 GeV threshold. While other threshold based analysis techniques also provided crosschecks, they all relied on the same reconstructed positron events, which means they all used highly correlated data. The Q-method was the most different parallel analyses with a much lower correlation factor (about 0.5) with all other analyses. Therefore, it was the most important

Table 3.2: Run 1 analysis results. The four Run-1 datasets were based on different field indices, n, given in the columns "Dataset" and "Field index (n)". The fitted R-values (according to equation 3.6), after unblinding are given in the column, "R [ppm]" and their corresponding statistical uncertainties are given in column "σ_R [ppm]".

Dataset	Field index (n)	R [ppm]	σ_R [ppm]
1a	0.108	-83.96	2.07
1b	0.120	-79.70	1.76
1c	0.120	-81.03	1.45
1d	0.107	-82.74	1.29

Table 3.3: Run 1 systematic uncertainties. The column "Systematic effect" lists all the systematic effects that were calculated for Run-1 Q-method analyses and the numbers under columns "1a", "1b", "1c" and "1d" denote the uncertainties associated with each of those effects for the Q-method analyses of the four Run-1 datasets. All the numbers are in parts per billion (ppb).

Systematic effect	1a	1b	1c	1d
Input clock stability	0.075	0.075	0.075	0.075
Input clock upconversion factor	2.100	2.100	2.100	2.100
In-fill Gain Amplitude	5.000	4.000	4.000	8.000
1n-fill Gain Time Constant	8.000	2.000	3.000	2.000
Pile-up modified error bars	15.000	15.000	15.000	15.000
Pile-up Simulations	10.000	10.000	10.000	10.000
Muon loss	17.000	3.000	2.000	3.000
CBO frequency change	5.500	16.000	48.400	33.000
CBO decoherence envelope model	4.100	1.000	14.000	38.000
CBO time constant	6.000	8.000	28.000	3.000
Vertical drift	198.000	200.000	342.000	208.000

crosscheck and proof of robustness of ω_a measurement.

While the biggest error contribution came from statistical uncertainty, the systematic effects also contributed to the overall uncertainty. Table 3.6.5 summarizes the systematic uncertainties. The procedures to describe the methods of estimating some of these systematic uncertainties will be discussed in detail in chapter 5. As evident, the Q-method analysis suffered most from the systematic uncertainty coming from vertical drift which is a slow effect. Since the Q-method has a very low threshold, it is more susceptible to any slow variation in the data. This motivated the need to develop analyses techniques which are less susceptible to such effects. The Ratio Method is one such histogramming technique which is described in the next chapter.

Chapter 4 The Ratio Method

4.1 Motivation

As discussed so far, the Energy Integrating Reconstruction or the Q-method draws its merits from the fact that it avoids individual positron reconstruction. Also it has less sensitivity to systematic biases coming from gain and pile-up effects owing to its small threshold which is applied only to avoid the region of noise (unlike positron counting methods where threshold is applied to select high energy positrons). Due to its low threshold Q-method is more susceptible to any slow variation in data. Run-1 Q-method result reported a systematic uncertainty of ~ 300 ppb from vertical drift which is a slow effect. This was the largest of all the systematic uncertainties. To control this a histogramming technique called Ratio-Method was employed in Run-2 and Run-3 ω_a analysis.

4.2 Ratio Method

The underlying principle for this histogramming technique is dividing the data into subsets and then constructing a ratio of linear combinations of the subsets in such a way that any slow effect that multiplies the normalization of the muon decay time spectrum would cancel out. The biggest slow effect comes from the muon's decay lifetime itself. To cancel out the effects of muon lifetime in the ratio, one subset of data is shifted later in time by half of anomalous precession frequency period, $T_a/2$, while another subset is shifted earlier in time by the same amount. A linear combination of these subsets can be used to cancel out muon's lifetime as described in section 4.2.1 [72].

4.2.1 Ratio Construction

To construct the ratio histogram, the four sets of the data are

$$v_1(t) = v_2(t) = H(t) \tag{4.1}$$

$$u_+(t) = H(t + \frac{T_a}{2}) \tag{4.2}$$

$$u_-(t) = H(t - \frac{T_a}{2}) \tag{4.3}$$

where $H(t)$ is the time distribution of the positron energies. Linear combinations taken are

$$U(t) = u_+(t) + u_-(t) \tag{4.4}$$

and

$$V(t) = v_1(t) + v_2(t) \tag{4.5}$$

Then the ratio would be

$$R(t) = \frac{V(t) - U(t)}{V(t) + U(t)} \tag{4.6}$$

Assuming a simple 5-parameter functional for $H(t)$,

$$H(t) = N_0 e^{\frac{-t}{\gamma\tau}}(1 + A cos(\omega_a t - \phi)) \tag{4.7}$$

we have

$$R(t) = \frac{2N_0 e^{\frac{-t}{\gamma\tau}}(1+Acos(\omega_a t))-N_0 e^{\frac{-(t-\frac{T_a}{2})}{\gamma\tau}}(1+Acos(\omega_a(t-\frac{T_a}{2})))-N_0 e^{\frac{-(t+\frac{T_a}{2})}{\gamma\tau}}(1+Acos(\omega_a(t+\frac{T_a}{2})))}{2N_0 e^{\frac{-t}{\gamma\tau}}(1+Acos(\omega_a t))+N_0 e^{\frac{-(t-\frac{T_a}{2})}{\gamma\tau}}(1+Acos(\omega_a(t-\frac{T_a}{2})))+N_0 e^{\frac{-(t+\frac{T_a}{2})}{\gamma\tau}}(1+Acos(\omega_a(t+\frac{T_a}{2})))} \tag{4.8}$$

where for simplicity, it is assumed that $\phi = 0$. Note that the normalization, N_0 and the exponential decay factor, $e^{-t/\gamma\tau}$ cancel out in the numerator and the denominator. Further, the ratio can be simplified and approximated as

$$R \approx A cos(\omega_a t) \tag{4.9}$$

This removes the slow effects including the muon lifetime as shown in Figure 4.1.
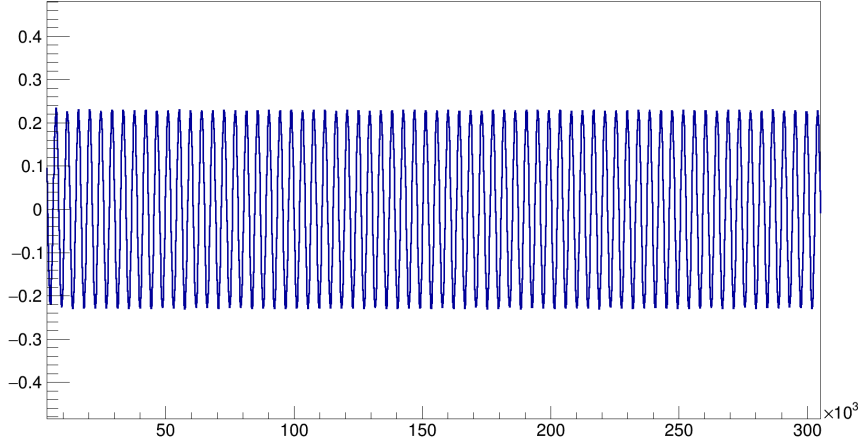
Figure 4.1: Ratio Q-method histogram

As evident in equation 4.8, this does not cancel out muon lifetime entirely and we still have factors $e^{\pm T_a/2\gamma\tau}$ in the numerator and the denominator. Instead of splitting the dataset equally with weights 1:1:1:1 into v_1, v_2, u_+ and u_-, if the weights are assigned according to 1:1:$e^{\frac{T_a}{2\tau}}$:$e^{\frac{-T_a}{2\tau}}$, a complete cancellation of τ can be achieved. In the same way the cancellation of the other slow terms is also not perfect, but since the lifetimes of these effects are thought to be large, the factors such as $e^{\pm T_a/2\tau_{slow}}$ are ~1 and are negligible.

48

Time Shift of the u_+, u_- Histograms in the Ratio Q-method

Q-method histograms have fixed time decimated bins, hence the shift can not be equal to exactly half of the g-2 period ($\sim$4365 ns). A scan was performed with various shifts in the 18.75 ns wide raw Q-Method bins ranging from a shift of 95 bins (1781.25 ns) to 144 bins (2700 ns), shown in figure 4.2 with dataset C from Run-2. Blinded R value showed no systematic dependence on various time shifts and the statistical precision on R (σ_R) was found to be lowest at a shift of ~ 116 bins (2175 ns) which is the closet that one can get to half of g-2 period with raw Q-method binning. A scan over shift in time bin for 3 parameter ratio fit fourier transform was also performed. The peaks corresponding to the CBO and vertical oscillations were found to appear and disappear from the fourier transforms for certain shifts in the bin as shown in figure 4.3. It was determined that a frequency peak disappeared from fourier transform when the shift in time was an integer multiple of the time period corresponding to that frequency[74].

Q-method final fits are performed with binning of 150 ns to minimize effects from fast rotation, so the raw bins need to be rebinned by a factor of 8. For the ratio construction, the Q-method raw bins are rebinned first by a factor of 8 to obtain 150 ns wide bins and then the ratio construction is done. The optimum bin shift (equivalent to half of g-2 period) for 150 ns wide bins is between 14 and 15 bins. A shift of 15 150 ns wide bins is close to the integer multiple of the vertical waist frequency time period[74]. If a shift of 15 bins is chosen, the vertical waist frequency disappears from the ratio histogram. However, due to combination with fast rotation signal a more complicated vertical waist envelope persists in the data with smaller amplitudes. This necessitates a randomization by the vertical waist frequency time period while constructing the ratio histogram[72]. To avoid this additional randomization, a shift of 14 bins was picked for Run-2 and Run-3 ratio Q-method analysis.

There are two different ways of generating the four subsets of data for constructing the ratio histogram: copy method and randomized method as described in the next two subsections.
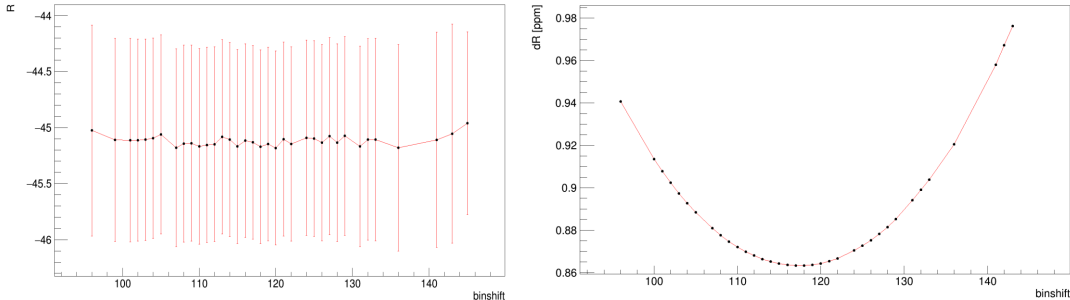
Figure 4.2: Figure on the left shows blind R[ppm] as a function of shift in 18.75ns wide bins for a subset of Run-2C. Figure on the right shows the corresponding statistical precision on R as a function of same shifts in 18.75ns bins.
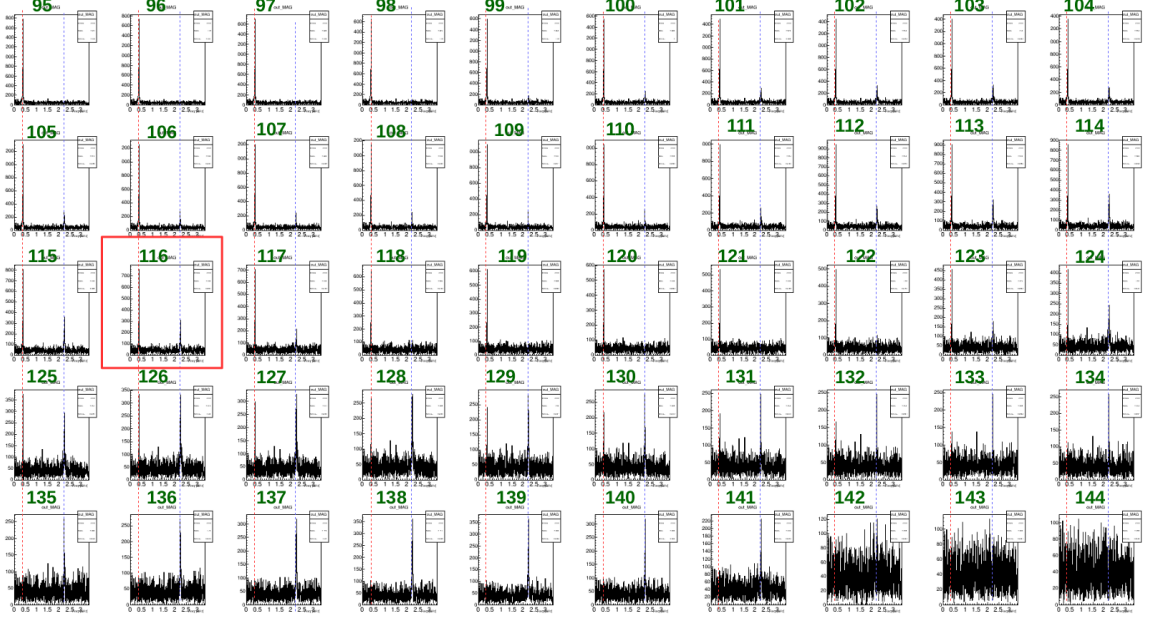
Figure 4.3: Fast Fourier Transforms (FFT) of ratio histogram fit for various shifts in 18.75 ns wide bins. The numbers in green on the top of each subplot denote the shift in number of bins for that FFT. The subplot highlighted with red box is the shift of bins closest to $\frac{1}{2}$ of g-2 period. The red and blue dotted vertical lines denote the positions of the CBO and vertical waist peak respectively.

Copy Ratio Method

The four sets of data are the copies of the same dataset. Since the copies of same histograms are shifted forward and backward and then combined together, this method introduces bin-to-bin correlations and correlated uncertainties. The calculation of the χ^2 function for minimization to perform the fit has to be correctly handled to account for the bin-to-bin correlations in the data. The χ^2 should be calculated using equation 4.10 [73].

$$\chi^2 = \sum_{ij}[y_i - f(x_i)][cov_{ij}]^{-1}[y_j - f(x_j)] \tag{4.10}$$

where y_i denotes the histogram content of ith bin, $f(x_i)$ is the fit-function evaluated at the corresponding time x_i and cov_{ij} is the covariance matrix element for bin i and j.

Applying the ratio construction from equation 4.7, content of each bin of the ratio histogram, y_{R_i} can be written as

$$y_{R_i} = \frac{2y_i - y_{i+\delta} - y_{i-\delta}}{2y_i + y_{i+\delta} + y_{i-\delta}} \tag{4.11}$$

Each bin content of the ratio histogram y_{R_i} gathers contribution from a set of bins separated by δ, where δ is $\sim 1/2$ of $g-2$ time period shift in Q-method bins.

Using the standard error propagation, one can obtain

$$\sigma_{R_i}^2 = (dy_{R_i})^2 = (\frac{\partial y_{R_i}}{\partial y_i})^2 (dy_i)^2 + (\frac{\partial y_{R_i}}{\partial y_{i+\delta}})^2 (dy_{i+\delta})^2 + (\frac{\partial y_{R_i}}{\partial y_{i-\delta}})^2 (dy_{i-\delta})^2 \qquad (4.12)$$

Covariance matrix elements were calculated for each non-zero pair of covariances. The non-zero covariances are: $cov(y_{R_i}, y_{R_i}) = (\sigma_{R_i})^2$, $cov(y_{R_i}, y_{R_{i\pm\delta}})$ and $cov(y_{R_i}, y_{R_{i\pm2\delta}})$ since,

$$y_{R_{i\pm\delta}} = \frac{2y_{i\pm\delta} - y_{i\pm2\delta} - y_i}{2y_{i\pm\delta} + y_{i\pm2\delta} + y_i} \qquad (4.13)$$

and

$$y_{R_{i\pm2\delta}} = \frac{2y_{i\pm2\delta} - y_{i\pm3\delta} - y_{i\pm\delta}}{2y_{i\pm2\delta} + y_{i\pm3\delta} + y_{i\pm\delta}} \qquad (4.14)$$

For covariance calculation we use

$$cov(y_i, y_j) = E(y_i y_j) - E(y_i)E(y_j) \qquad (4.15)$$

Since each of these quantities y_i and y_j are data points of ratio histograms, the calculation of expectation values is not straightforward. This motivates the need to look for methods of approximation. One such approximation method can be to employ Taylor expansion of the quantities y_i and y_j so that the ratio becomes a linear combination of its constituents. To calculate the expectation values $E(f(x, y, z..))$, where f is a function of $x, y, z...$, we can make use of Taylor expansion of $f(x, y, z...)$ about the mean $x_0, y_0, z_0...$ [75].

$$\begin{aligned} E(f(x, y, z..)) = &E(f(x_0, y_0, z_0..) + f'_x(x_0, y_0, z_0..)(x - x_0) + f'_y(x_0, y_0, z_0..)(y - y_0) \\ &+ f'_z(x_0, y_0, z_0..)(z - z_0) + \frac{1}{2}[f''_x(x_0, y_0, z_0..)(x - x_0)^2 \\ &+ f''_y(x_0, y_0, z_0..)(y - y_0)^2 + f''_z(x_0, y_0, z_0..)(z - z_0)^2 \\ &+ 2f''_{x,y}(x - x_0)(y - y_0) + 2f''_{y,z}(y - y_0)(z - z_0) + 2f''_{z,x}(z - z_0)(x - x_0)] \\ &+ ....) \end{aligned}$$

$$(4.16)$$

This simplifies the expectation value of the ratio histogram to be expressed as a linear sum of the terms of the Taylor expansion.

For example , to calculate $E(y_{R_i})$, one can write $E(y_{R_i})$ in terms of Taylor expansion of y_{R_i} about true means $(\mu_{y_i}, \mu_{y_{i+\delta}}, \mu_{y_{i-\delta}})$ of its constituent bins $y_i, y_{i+\delta}$ and $y_{i-\delta}$

$$E(y_{R_i}) = E(\frac{2y_i - y_{i+\delta} - y_{i-\delta}}{2y_i + y_{i+\delta} + y_{i-\delta}}) \qquad (4.17)$$

51

where

$$
\begin{aligned}
E(y_{R_i}) =\ & E(y_{R_i}|_{\mu_{y_i},\mu_{y_{i+\delta}},\mu_{y_{i-\delta}}} \\
& + \frac{\partial y_{R_i}}{\partial y_i}|_{\mu_{y_i},\mu_{y_{i+\delta}},\mu_{y_{i-\delta}}}(y_i - \mu_{y_i}) + \frac{\partial y_{R_i}}{\partial y_{i+\delta}}|_{\mu_{y_i},\mu_{y_{i+\delta}},\mu_{y_{i-\delta}}}(y_{i+\delta} - \mu_{y_{i+\delta}}) \\
& + \frac{\partial y_{R_i}}{\partial y_{i-\delta}}|_{\mu_{y_i},\mu_{y_{i+\delta}},\mu_{y_{i-\delta}}}(y_{i-\delta} - \mu_{y_{i-\delta}}) + \frac{1}{2!}[\frac{\partial^2 y_{R_i}}{\partial y_i^2}|_{\mu_{y_i},\mu_{y_{i+\delta}},\mu_{y_{i-\delta}}}(y_i - \mu_{y_i})^2 \\
& + \frac{\partial^2 y_{R_i}}{\partial y_{i+\delta}^2}|_{\mu_{y_i},\mu_{y_{i+\delta}},\mu_{y_{i-\delta}}}(y_{i+\delta} - \mu_{y_{i+\delta}})^2 + \frac{\partial^2 y_{R_i}}{\partial y_{i-\delta}^2}|_{\mu_{y_i},\mu_{y_{i+\delta}},\mu_{y_{i-\delta}}}(y_{i-\delta} - \mu_{y_{i-\delta}})^2 \\
& + 2\frac{\partial^2 y_{R_i}}{\partial y_i \partial y_{i+\delta}}|_{\mu_{y_i},\mu_{y_{i+\delta}},\mu_{y_{i-\delta}}}(y_i - \mu_{y_i})(y_{i+\delta} - \mu_{y_{i+\delta}}) \\
& + 2\frac{\partial^2 y_{R_i}}{\partial y_{i+\delta} \partial y_{i-\delta}}|_{\mu_{y_i},\mu_{y_{i+\delta}},\mu_{y_{i-\delta}}}(y_{i+\delta} - \mu_{y_{i+\delta}})(y_{i-\delta} - \mu_{y_{i-\delta}}) \\
& + 2\frac{\partial^2 y_{R_j}}{\partial y_{i-\delta} \partial y_i}|_{\mu_{y_i},\mu_{y_{i+\delta}},\mu_{y_{i-\delta}}}(y_{i-\delta} - \mu_{y_{i-\delta}})(y_i - \mu_{y_i})])
\end{aligned}
$$

(4.18)

Now the terms like $E(y_{i+\delta} - \mu_{y_{i+\delta}})$ are zero[75]. So non-zero terms in $E(y_{R_i})$ are:

$$
\begin{aligned}
E(y_{R_i}) =\ & E(y_{R_i}|_{\mu_{y_i},\mu_{y_{i+\delta}},\mu_{y_{i-\delta}}} \\
& + \frac{1}{2!}[\frac{\partial^2 y_{R_i}}{\partial y_i^2}|_{\mu_{y_i},\mu_{y_{i+\delta}},\mu_{y_{i-\delta}}}(y_i - \mu_{y_i})^2 \\
& + \frac{\partial^2 y_{R_i}}{\partial y_{i+\delta}^2}|_{\mu_{y_i},\mu_{y_{i+\delta}},\mu_{y_{i-\delta}}}(y_{i+\delta} - \mu_{y_{i+\delta}})^2 \\
& + \frac{\partial^2 y_{R_i}}{\partial y_{i-\delta}^2}|_{\mu_{y_i},\mu_{y_{i+\delta}},\mu_{y_{i-\delta}}}(y_{i-\delta} - \mu_{y_{i-\delta}})^2])
\end{aligned}
$$

(4.19)

And terms like $E(y_{i+\delta} - \mu_{y_{i+\delta}})^2$ are $\sigma_{i+\delta}^2$. So $E(y_{R_i})$ is given by

$$
\begin{aligned}
E(y_{R_i}) =\ & y_{R_i}|_{\mu_{y_i},\mu_{y_{i+\delta}},\mu_{y_{i-\delta}}} + \frac{1}{2!}[\frac{\partial^2 y_{R_i}}{\partial y_i^2}|_{\mu_{y_i},\mu_{y_{i+\delta}},\mu_{y_{i-\delta}}}\sigma_i^2 + \frac{\partial^2 y_{R_i}}{\partial y_{i+\delta}^2}|_{\mu_{y_i},\mu_{y_{i+\delta}},\mu_{y_{i-\delta}}}\sigma_{i+\delta}^2 \\
& + \frac{\partial^2 y_{R_i}}{\partial y_{i-\delta}^2}|_{\mu_{y_i},\mu_{y_{i+\delta}},\mu_{y_{i-\delta}}}\sigma_{i-\delta}^2]
\end{aligned}
$$

(4.20)

Likewise the other terms in Equation 4.15 are calculated.

Covariances can be also determined empirically from the auto-correlation histogram. For this, one must perform an initial fit without the full covariance matrix and then a fourier transform (FT) of the fit residuals. Then, the plot of auto-correlations can be generated from the FT of the squared FT of the initial fit residuals. An example

is shown in 4.4. This plot gives the correlation coefficients for the correlated bins. For example, to obtain the correlation coefficient between bin i and bin $i+\delta$, we take the ratio of the bin content of bin number $1 \pm \delta$ and bin number 1. And then the covariances can be calculated as

$$Cov(y_{R_i}, y_{R_j}) = Corr(y_{R_i}, y_{R_j})\sigma_{R_i}\sigma_{R_j} \qquad (4.21)$$

One should note that the auto-correlation plot is prone to noise. The correlation coefficients calculated using both Taylor expansion method and the auto-correlation method agree well with each other as shown in 4.5.
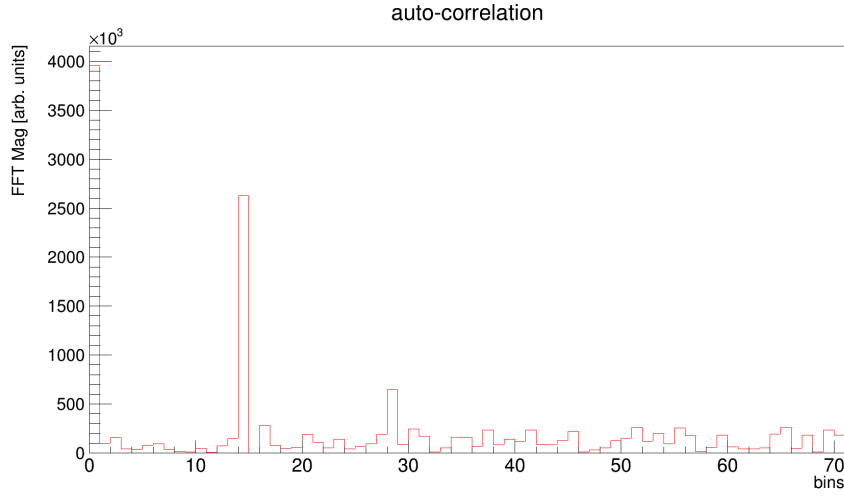
Figure 4.4: Auto-correlation plot (only showing first 70 bins): The correlation peaks appear at bin 15 and bin 29, which correspond to a shift of $\delta =14$ bins with respect to bin 1.

Randomized Ratio Method

In this ratio construction, the Q-method flushes are randomly split into four different histograms, thus the subsets are independent of each other. The χ^2 calculation is simplified to equation 4.22 [73].

$$\chi^2 = \frac{f(x_i) - y_i}{\sigma_i^2} \qquad (4.22)$$

Now the ratio histogram bins are

$$y_{R_i} = \frac{y_{1_i} + y_{2_i} - y_{3_i} - y_{4_i}}{y_{1_i} + y_{2_i} + y_{3_i} + y_{4_i}} \qquad (4.23)$$

where y_{3_i} and y_{4_i} are shifted by $\pm\delta$ with respect to y_{1_i} and y_{2_i}.
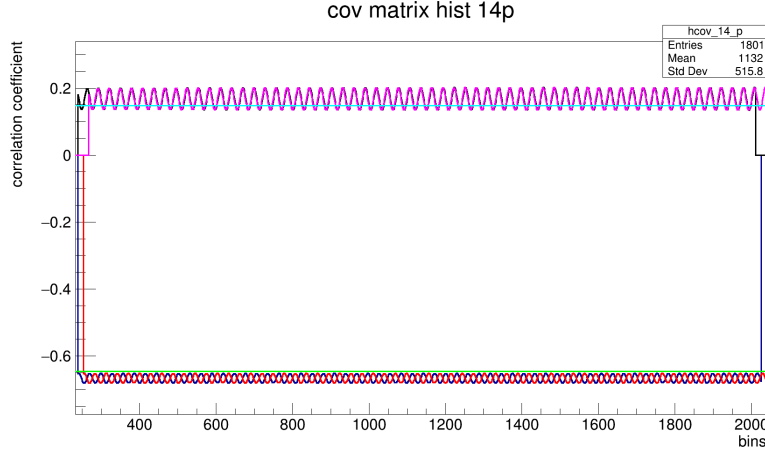
Figure 4.5: Correlation coefficients; coefficients calculated by Taylor expansion method are shown in dark blue for $+\delta$, in red for $-\delta$, in black for $+2\delta$ and in pink for -2δ. Coefficients calculated empirically(from auto-correlation histogram) are shown in green for $\pm\delta$ and in cyan for $\pm2\delta$

The errors are propagated from the constituent histograms

$$(dy_{R_i})^2 = (\frac{\partial y_{R_i}}{\partial y_{1_i}})^2(dy_{1_i})^2 + (\frac{\partial y_{R_i}}{\partial y_{2_i}})^2(dy_{2_i})^2 + (\frac{\partial y_{R_i}}{\partial y_{3_i}})^2(dy_{3_i})^2 + (\frac{\partial y_{R_i}}{\partial y_{4_i}})^2(dy_{4_i})^2 \quad (4.24)$$

Creating four independent subsets introduces extra noise in the ratio histogram which then requires running and averaging over random seeds. For Run-2 and 3 results, 32 random seeds were used.

4.2.2 Fast Rotation Handling

Smoothing or the phase cancellation of the cyclotron frequency can be implemented to reduce the effect of cyclotron frequency as has been introduced in 3.6.3. For Runs-2 and 3 analysis, the raw 18.75 ns wide Q-method bins were first rebinned by 4 to obtain 75 ns wide binning. Next, a second copy of the data was made and an offset of one bin (75 ns) was introduced between the two copies. Then the two copies, shifted and unshifted were superimposed leading to cancellation of the cyclotron phase. This introduced additional correlations in the data, which also needed proper handling. The procedure is described in the next sub-section.

Fast Rotation Smoothing in Copy Ratio Method

Let y_i denote the bins of the histogram which have binwidth equal to approximately half of cyclotron period i.e 75 ns (rebinned by factor of 4 with respect to the raw 18.75 ns bin width). To cancel out the Fast Rotation phase, a copy of this histogram is
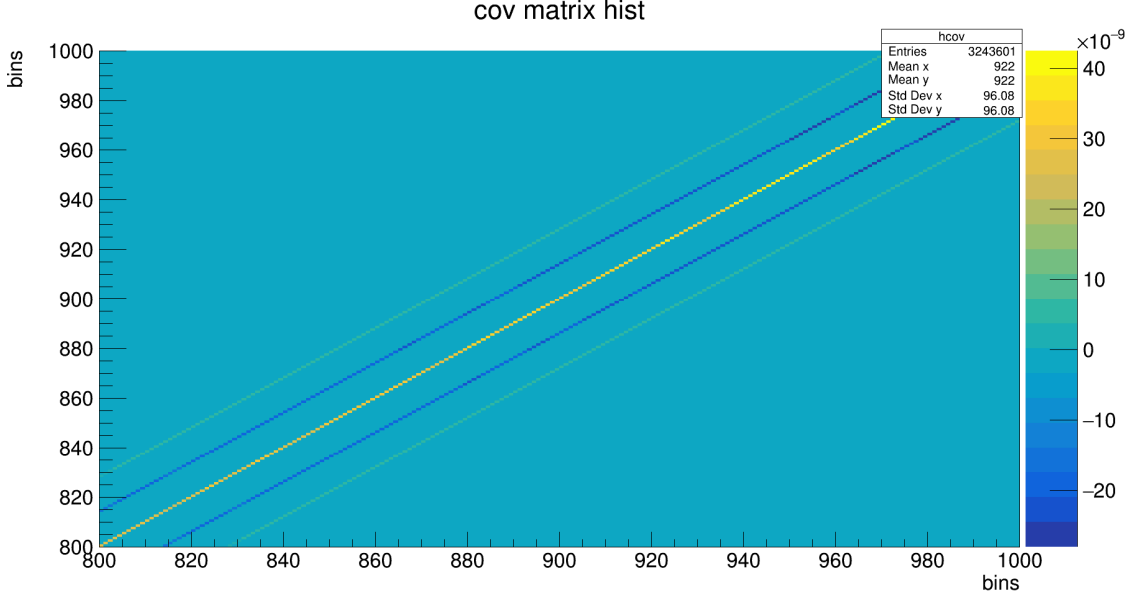
Figure 4.6: Covariance matrix(zoomed in at 800-1000 bins range) for Ratio Method without the fast rotation correction. The non-zero elements appear along diagonal, diagonal$\pm\delta$ and diagonal$\pm2\delta$.

made and shifted by one bin. The shifted and unshifted copies are then superimposed to cancel out the FR phase.

$$y_{FR_i} = \frac{y_i + y_{i+1}}{2} \tag{4.25}$$

The superposed histogram, y_{FR_i} is then further rebinned by a factor of 2 to obtain y_{RB_i} with 150 ns binning.

$$y_{RB_i} = \frac{y_{FR_{2i-1}} + y_{FR_{2i}}}{2} \tag{4.26}$$

or in terms of y_i,

$$y_{RB_i} = \frac{y_{2i-1}}{4} + \frac{y_{2i}}{2} + \frac{y_{2i+1}}{4} \tag{4.27}$$

Four copies of y_{RB_i} are made to construct the ratio histogram.

$$y_{R_i} = \frac{2y_{RB_i} - y_{RB_{i+\delta}} - y_{RB_{i-\delta}}}{2y_{RB_i} + y_{RB_{i+\delta}} + y_{RB_{i-\delta}}} \tag{4.28}$$

δ corresponds to a shift by $\sim 1/2$ of $g-2$ period. Hence again in terms of y_i, one can rewrite as

$$y_{R_i} = -\frac{2y_{2(i-\delta)} - 4y_{2i} + 2y_{2(i+\delta)} + y_{2(i-\delta)-1} + y_{2(i-\delta)+1} - 2y_{2i-1} - 2y_{2i+1} + y_{2(i+\delta)-1} + y_{2(i+\delta)+1}}{2y_{2(i-\delta)} + 4y_{2i} + 2y_{2(i+\delta)} + y_{2(i-\delta)-1} + y_{2(i-\delta)+1} + 2y_{2i-1} + 2y_{2i+1} + y_{2(i+\delta)-1} + y_{2(i+\delta)+1}} \tag{4.29}$$

55

Table 4.1: Non-zero elements in the covariance matrix for copy ratio method with fast rotation handling. δ is equal to the time shift in units of the Q-method bins

Non-zero elements
i,i±1
i,i±$(\delta - 1)$
i,i±δ
i,i±$(\delta + 1)$
i,i±$(2\delta - 1)$
i,i±2δ
i,i±$(2\delta + 1)$

The errors are propagated from the constituent histograms

$$
\begin{aligned}
\sigma^2_{R_i} = (dy_{R_i})^2 = & (\frac{\partial y_{R_i}}{\partial y_{2(i-\delta)}})^2 (dy_{2(i-\delta)})^2 + (\frac{\partial y_{R_i}}{\partial y_{2i}})^2 (dy_{2i})^2 + (\frac{\partial y_{R_i}}{\partial y_{2(i+\delta)}})^2 (dy_{2(i+\delta)})^2 \\
& + (\frac{\partial y_{R_i}}{\partial y_{2(i-\delta)-1}})^2 (dy_{2(i-\delta)-1})^2 + (\frac{\partial y_{R_i}}{\partial y_{2(i-\delta)+1}})^2 (dy_{2(i-\delta)+1})^2 \\
& + (\frac{\partial y_{R_i}}{\partial y_{2i-1}})^2 (dy_{2i-1})^2 + (\frac{\partial y_{R_i}}{\partial y_{2i+1}})^2 (dy_{2i+1})^2 + (\frac{\partial y_{R_i}}{\partial y_{2(i+\delta)-1}})^2 (dy_{2(i+\delta)-1})^2 \\
& + (\frac{\partial y_{R_i}}{\partial y_{2(i+\delta)+1}})^2 (dy_{2(i+\delta)+1})^2
\end{aligned}
$$

$$(4.30)$$

The non-zero elements in covariance matrix in this case are given in table 4.2.2.

These covarainces can be calculated similarly using the procedure described in section 4.2.1.

Fast Rotation Smoothing in Randomized Ratio Method

To implement fast rotation phase cancellation in randomized ratio method, four independent subsets of data with time bin width equal to $\sim \frac{1}{2}$ of cyclotron period (75 ns) are generated. Then a copy of each those histogram is shifted by one bin and then superimposed with the corresponding unshifted histogram: $y_{1_{FR_i}} = \frac{y_{1_i}+y_{1_{i+1}}}{2}$, $y_{2_{FR_i}} = \frac{y_{2_i}+y_{2_{i+1}}}{2}$, $y_{3_{FR_i}} = \frac{y_{3_i}+y_{3_{i+1}}}{2}$ and $y_{4_{FR_i}} = \frac{y_{4_i}+y_{4_{i+1}}}{2}$. Then the ratio is con-
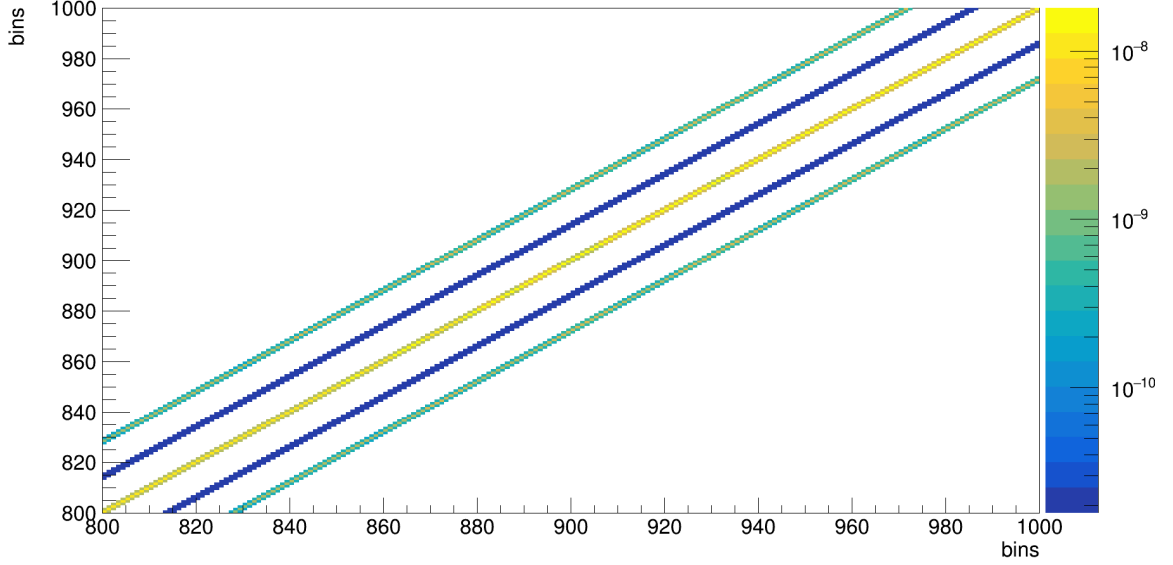
Figure 4.7: Full covariance matrix(zoomed in at 800-1000 bins range) for Fast Rotation corrected Ratio Method. The non-zero elements appear along diagonal, diagonal ±1, diagonal $\pm\delta$, (diagonal $\pm\delta$) ± 1, diagonal $\pm2\delta$ and (diagonal $\pm2\delta$) ± 1.

structed similar to equation 4.23. The error propagation in this case would be

$$
\begin{aligned}
\sigma^2_{R_i} = (dy_{R_i})^2 = & (\frac{\partial y_{R_i}}{\partial y_{1_{i-1}}})^2(dy_{1_{i-1}})^2 + (\frac{\partial y_{R_i}}{\partial y_{1_i}})^2(dy_{1_i})^2 + (\frac{\partial y_{R_i}}{\partial y_{1_{i+1}}})^2(dy_{1_{i+1}})^2 \\
& (\frac{\partial y_{R_i}}{\partial y_{2_{i-1}}})^2(dy_{2_{i-1}})^2 + (\frac{\partial y_{R_i}}{\partial y_{2_i}})^2(dy_{2_i})^2 + (\frac{\partial y_{R_i}}{\partial y_{2_{i+1}}})^2(dy_{2_{i+1}})^2 \\
& (\frac{\partial y_{R_i}}{\partial y_{3_{i-1}}})^2(dy_{3_{i-1}})^2 + (\frac{\partial y_{R_i}}{\partial y_{3_i}})^2(dy_{3_i})^2 + (\frac{\partial y_{R_i}}{\partial y_{3_{i+1}}})^2(dy_{3_{i+1}})^2 \\
& (\frac{\partial y_{R_i}}{\partial y_{4_{i-1}}})^2(dy_{4_{i-1}})^2 + (\frac{\partial y_{R_i}}{\partial y_{4_i}})^2(dy_{4_i})^2 + (\frac{\partial y_{R_i}}{\partial y_{4_{i+1}}})^2(dy_{4_{i+1}})^2
\end{aligned}
\tag{4.31}
$$

And the non-zero covariances are $Cov(yR_i, yR_{i\pm1})$ which can be calculated in the same way as described in section 1.1.2.

4.2.3 Fourier Transforms of Correlated data

The fourier transform of the residuals of fit to data with bin-to-bin correlations has correlation wave. A toy simulation showing the number of oscillation periods changing with the shift in 150 ns wide Q-method bins is shown in 4.8. The number of oscillation periods in the full FFT (Fast Fourier Transform) spectrum is equal to the number of bins by which the histograms are shifted. The presence of the wave makes it difficult to look for smaller peaks in the FFT, hence it is important to cross check with the FFT of a randomized ratio method fit. An attempt was made to remove this structure from the FFT by fitting with a simple sine squared function. However, it was found that such a function is not enough to remove the structure from the FFT, and so

further simulation studies are recommended to investigate the exact structure of the correlation bumps in the FFT.
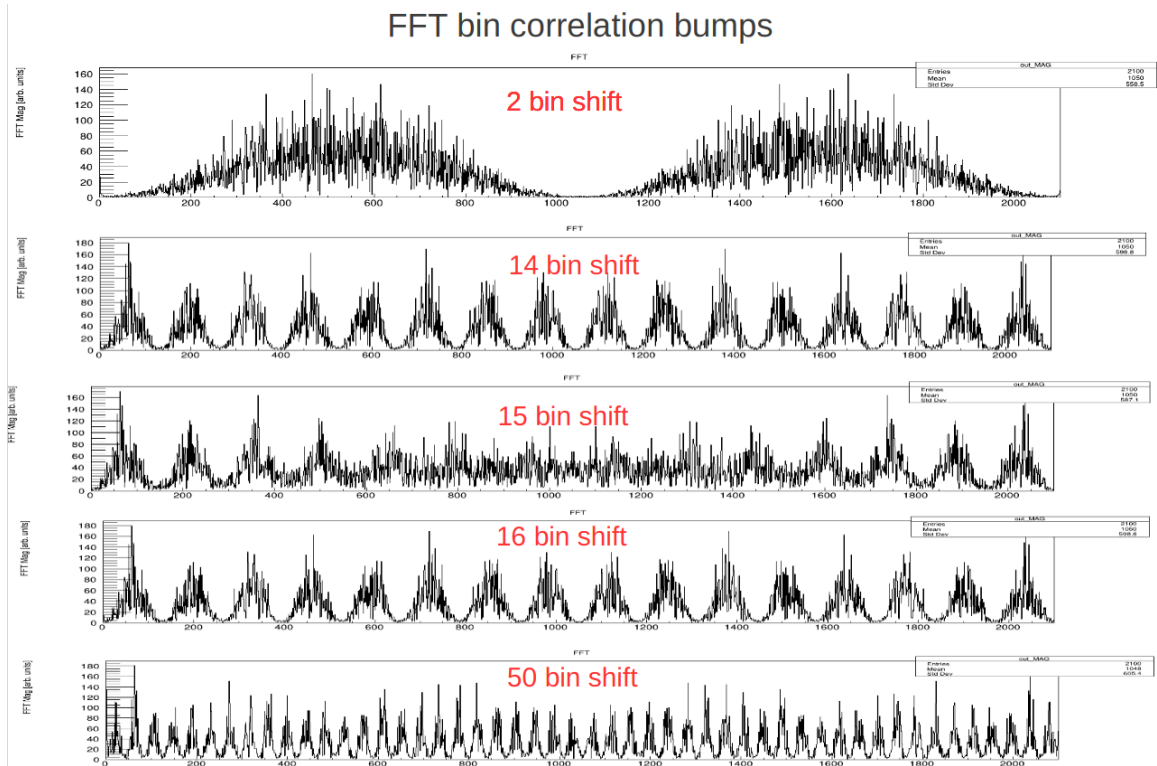
Figure 4.8: Fourier Transforms for various time bin shifts in ratio method. The red caption at the top of each subplot denotes the time shift in the number of 150 ns wide bins.

Chapter 5 Energy Integrating, Ratio Method Analysis of Run-2 and 3 Data

5.1   Data Analyzed

Energy Integrated Ratio method described in chapter 3 and 4, was one of the analysis techniques used in Run-2 and Run-3 precession frequency analysis in E-989. Run-2 data taking began in late 2018 and concluded in summer of 2019 while Run-3 data was collected from 2019 Fall through 2020 Spring. Total number of sub-datasets in these two runs combined are 20 and the total size of the dataset is approximately four times the total data collected in the BNL experiment. Run-2 production data consists of 7 datasets denoted B through H and Run-3 production datasets are denoted B through O. Between data taking periods of Run-2 and Run-3, a better temperature stability was achieved in the experimental hall which hosts the storage ring. There was also hardware improvement work done on the kicker system while taking Run-3 data. As a result, the optimum kick was achieved starting from sub-dataset N from Run-3. Also, the hardware blinding is different between Run-2 and Run-3 data. As a result, the data collected in these two runs are analyzed in 3 groups, Run-2 (B to H), Run-3a (B to M) and Run-3b (N and O). Table 5.1 summarizes the data analyzed from Run-2 and Run-3 per dataset. Software release **v9_75_00** was used to analyze all the datasets.

5.2   Procedures

5.2.1   Data Selection

As mentioned before, the Q-method data is recorded in time-decimated bins where the smallest bin width can be 1 clock-tick ~ 1.25 ns. Beginning with run number 24727, which is a part of dataset 2C, the DAQ settings were changed. Time decimation factor was changed from 60 to 15, fills per flush was increased from 1 to 4 and the end time was extended to 352000 clock-ticks. As a result, the Run-2 and 3 datasets that were analyzed have a bin width of 15 clock-ticks or ~ 18.75 ns. Since the start time of the flush corresponds to 100000 clock-ticks, the total number of time bins in each of the datasets are 16800.

Not every fill that is recorded by the DAQ system is analysis quality data. There are fills that are taken during sparks in the ESQ system or kicker system. Some of the fills also contain laser pulses used for determining in-fill gain correction constants. All these are removed from production data by performing a Data Quality Cut (DQC) analysis. Since the Q-method combines fills into flushes, it needs to have a modified version of DQC cuts. A flush-by-flush DQC cut was applied to Run-2 and 3 datasets using the filter module **QFlushDQCFilter_module.cc** which is why Q-method analyzed data have less number of fills analyzed than total available. Since

Table 5.1: Data analyzed for Run 2 and 3. The column "Dataset name" lists the names given to the produced datasets that were finally analyzed. The column "Total Fills" denotes the number of fills that were present in these produced datasets and the column "Fills analyzed" denotes the number of fills that were analyzed in the Q-method due to the modified data quality cuts. The last column, "Fraction", denotes the percentage of total fills analyzed in the Q-method analysis.

	Dataset name	Total Fills	Fills Analyzed	Fraction
2B	gm2pro_daq_offline_dqc_run2B_5126A	1437874	0	0%
2C	gm2pro_daq_offline_dqc_run2C_51224A	6593870	4984328	75.59%
2D	gm2pro_daq_offline_dqc_run2D_5123A	5284733	4369016	82.67%
2E	gm2pro_daq_offline_dqc_run2E_5124BC	2098556	1677976	79.96%
2F	gm2pro_daq_offline_dqc_run2F_5125AB	2130004	2063216	96.86%
2G	gm2pro_daq_offline_dqc_run2G_5125A	445103	431032	96.84%
2H	gm2pro_daq_offline_dqc_run2H_5125A	609113	589904	96.85%
3B	gm2pro_daq_offline_dqc_run3B_5218A	4693687	4575656	97.49%
3C	gm2pro_daq_offline_dqc_run3C_5218A	1275319	1238260	97.09%
3D	gm2pro_daq_offline_dqc_run3D_5218A	7185302	6973100	97.05%
3E	gm2pro_daq_offline_dqc_run3E_5218A	2900754	2807360	96.78%
3F	gm2pro_daq_offline_dqc_run3F_5218A	1467861	1421264	96.83%
3G	gm2pro_daq_offline_dqc_run3G_5218A	3326052	3221392	96.85%
3I	gm2pro_daq_offline_dqc_run3I_5218A	3220143	3117812	96.82%
3J	gm2pro_daq_offline_dqc_run3J_5218A	2397365	2321472	96.83%
3K	gm2pro_daq_offline_dqc_run3K_5218A	1563390	1512068	96.72%
3L	gm2pro_daq_offline_dqc_run3L_5218A	1120450	1083544	96.71%
3M	gm2pro_daq_offline_dqc_run3M_5218A	3911125	3791196	96.93%
3N	gm2pro_daq_offline_dqc_run3N_5217ABC	6615051	6342024	95.87%
3O	gm2pro_daq_offline_dqc_run3O_5217A	4932960	4770784	96.71%

DAQ setting was changed during dataset 2C, dataset 2B had Run-1 configuration and was not included in Run-2 and 3 analysis.

Q-method Energy Threshold

A threshold scan was performed to determine the optimal value. There was no consistent trend in R or σ_R with a changing threshold. Figure 5.1 shows threshold scan of dataset 2D from 100 MeV to 800 MeV. While choosing a higher threshold did show an improvement in χ^2/NDF, it also led to losing some low energy pulses. Hence it was decided to keep the threshold same as Run-1 analysis which is 300 MeV. The threshold of 300 MeV was also comfortably above the energies of other possible beam contaminants like deuterons, protons or lost muons.
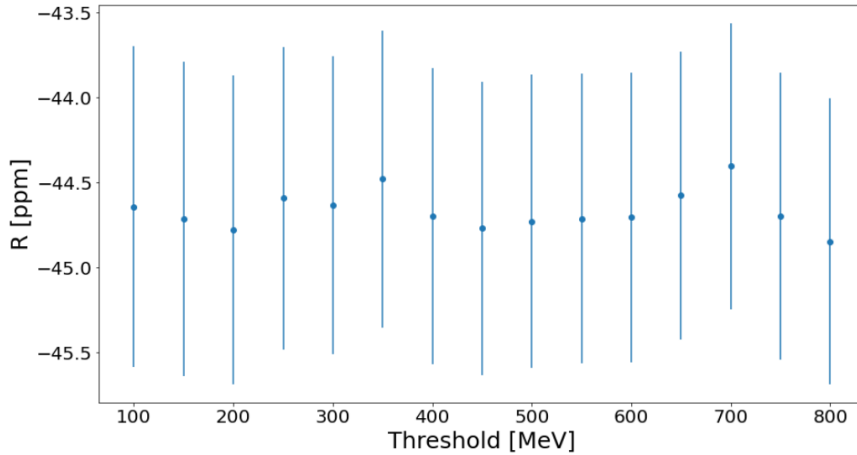
Figure 5.1: Threshold scan of blinded R from dataset 2D

Pedestal Subtraction

Pedestal subtraction algorithm has already been described in section 3.3. For Run-2 and 3 datasets, the pedestal window was 8 bins on either side of the trigger sample with a gap of 1 bin. 8 bins was chosen to make the pedestal window width 150 ns which is approximately the same as the fast rotation time period of 149.2 ns to avoid biases due to cyclotron modulation.

Noise Handling

This procedure has also been discussed in section 3.4. For Run-2 and 3 analysis, the window for calculating average noise was 100 time bins near the end of the flush time range between bin 16650 and 16750. The value of threshold multiplier for calculating the rolling threshold was determined through a scan. The range of threshold multiplier values covered in this scan is from 5 to 15. The value of 10 was found to be optimum to remove crystal noise from the data[76].

Removal of In-fill Laser

For Run-2 and 3, flushes with in-fill laser pulses were removed from the analyzed data using the filter module **QFlushDQCFilter_module.cc**. Since this module was found to be failing in some cases, an additional filter was also incorporated in the analyzer to remove in-fill laser. In this filter, for each time bin of each flush, the ADC value is compared against a small threshold of 1000, which was chosen empirically (since the laser pulses typically have a high amplitude). If an ADC value of 1000 or greater occured in the same time bin for more than 50 crystals (almost all the crystals of the calorimeter see the laser pulse when it is fired), then that flush was flagged as having an in-fill laser pulse and was discarded.

Removal of Unphysical Large Spikes

Some very large unphysical spikes were also encountered in the data, which were suspected to be introduced by a corrupt node while running production jobs on the High Performance Computing (HPC) grid. To prevent such spikes from contaminating the data, a crystal-by-crystal rejection of flushes with samples with ADC values less than -3000 and greater than 40000 was applied. This was implemented using filter module **QSpikeCheckFilter_module.cc**

Repeat Readout of Stale Calorimeter Data between Flushes

An occasional problem with repeat of stale calorimeter data was found in which there was a readout of a fill between flushes. Since the flush factor is set to 4, having a non-empty fill at a gap of less than 4 fills was making some of the data redundant. This spurious readout only occurred in a handful of calorimeters. To check this, a filter module **QFlushQualityFilter_module.cc** was put in where a fill readout was rejected if it was found to contain less than 22 calorimeters which is the production standard.

5.2.2 Energy Calibration and Gain Correction

For ADC-to-MeV calibration constants, a dataproduct named **EnergyCalibrationConstantsArtRecord** was used to perform the energy calibration for each crystal. Similarly, the out-of-fill gain corrections were obtained using the dataproduct **OOFConstantsArtRecord** and the ADC values per crystal were divided by the constants. For in-fill gain, module **IFGnostdpConstantsService** from dataproduct **IFGConstantsArtRecord** was used and the ADC values were divided by the constants.

5.2.3 Pile-up Correction

Pile-up is corrected while applying the pedestal subtraction. Any above threshold pulse in the pedestal window is rejected from the average pedestal calculation to avoid distortion to the calculated pedestal. There was a small leftover effect from under-

threshold pulses falling on the trigger sample and pedestal window. A systematic uncertainty associated with this effect will be calculated.

5.2.4 Fast Rotation

As already described in section 3.6.3, smoothing procedure was implemented to reduce the effect of fast rotation. The raw 18.75 ns Q-method bins were first rebinned by 4 to 75 ns binning. Then a second copy of the data was made and shifted by one (75 ns) bin. Then the two copies, shifted and unshifted were superimposed leading to cancellation of the cyclotron phase. This introduced bin-to-bin correlations in the data.

5.2.5 Ratio Construction

The fast rotation corrected Q-method histograms with binwidth 75 ns were rebinned by 2 to obtain 150 ns wide binning. At this stage four copies of the dataset were made and then two of them were shifted earlier and later in time by 14 bins (= 2100 ns $\sim$ $\frac{1}{2}$g-2 period). The weighting factors for the 4 subsets need fixing the muon lifetime to a pre-determined value. This was chosen to be 64.440 μs which was obtained from the results of fitting the Run-2 data using regular Q-method where muon lifetime was a fit-parameter. The ratio was constructed as follows:

$$y_{R_i} = \frac{2y_i - y_{i+\delta} - y_{i-\delta}}{2y_i + y_{i+\delta} + y_{i-\delta}} \tag{5.1}$$

where δ is 14 bins, y_i is the fast rotation corrected histogram and y_{R_i} is the ratio histogram on which the fits are performed. This introduced additional bin-to-bin correlations in the data. And as discussed before, the χ^2 for fit minimization was calculated as

$$\chi^2 = \sum_{i,j} [y_{R_i} - f(x_i)][cov_{ij}]^{-1}[y_{R_j} - f(x_j)] \tag{5.2}$$

5.2.6 Fit Function

Since the data has been transformed into ratio histograms, the fit function also needed to be changed accordingly. Simplest functional form to fit the ratio histogram would be

$$f(t) = A cos(\omega_a t - \phi) \tag{5.3}$$

However as mentioned in section 4.2.1, this functional form is an approximation and does not account for the distortions due to beam dynamics. So, for fitting the ratio histogram following fit function was used

$$F(t) = \frac{2f(t) - f(t + \frac{T_a}{2}) - f(t - \frac{T_a}{2})}{2f(t) + f(t + \frac{T_a}{2}) + f(t - \frac{T_a}{2})} \tag{5.4}$$

where,

$$f(t) = N_{cbo}N_{vw}N_yN_{xy}(1 + A(t)cos(\omega_a t - \phi_0 - \phi(t))) \tag{5.5}$$

The terms in equation 5.5 are expanded as

$$N_{cbo} = 1 + A_{cbo_N} e^{-\frac{t}{\tau_{cbo}}} \cos(\omega_{cbo}(t)t - \phi_{cbo_N}) + A_{2cbo_N} e^{-\frac{2t}{\tau_{cbo}}} \cos(2\omega_{cbo}(t)t - \phi_{2cbo_N}) \quad (5.6)$$

with $\omega_{cbo}(t) = \omega_{cbo}(1 + A_{cbo_t} e^{-\frac{t}{\tau_{cbo_t}}})$

$$N_{vw} = 1 + A_{vw} e^{-\frac{t}{\tau_{vw}}} \cos(\omega_{vw}t - \phi_{vw}) \quad (5.7)$$

$$N_y = 1 + A_y e^{-\frac{t}{\tau_y}} \cos(\omega_y t - \phi_y) \quad (5.8)$$

$$N_{xy} = 1 + A_{xy} e^{-\frac{t}{\tau_{xy}}} \cos(\omega_{xy}t - \phi_{xy}) \quad (5.9)$$

$$A(t) = A_0 e^{-\frac{t}{\tau_{rlx}}} (1 + A_{cbo_A} e^{-\frac{t}{\tau_{cbo}}} \cos(\omega_{cbo}(t)t - \phi_{cbo_A})) \quad (5.10)$$

$$\phi(t) = A_{cbo_\phi} e^{-\frac{t}{\tau_{cbo}}} \cos(\omega_{cbo}(t)t - \phi_{cbo_\phi}) \quad (5.11)$$

N_{cbo}, $A(t)$ and $\phi(t)$ are the terms that capture normalization, asymmetry and phase modulation by the coherent betatron oscillation (CBO) which is a radial oscillation of the muon beam as described in section 3.6.4. Notice that an additional time dependence has been added to the CBO frequency ω_{cbo}. This term is incorporated to handle the drift in ω_{cbo} at early times. The need for this functional form was seen when the fit start time scans were performed (described in section 5.3.1). The CBO parameters were drifting at early times without this time dependence included in the fit function as shown in figure 5.7. The time variation of CBO frequency was not observed in Run-3b (the dataset after kicker improvement) and so this term was not included in fit function for fitting Run-3b.

N_{vw} and N_y are the normalization modulation due to vertical waist (VW) oscillation and oscillation of the vertical mean respectively. An additional frequency at 1.9 MHz was also observed. This is the frequency due to the cross term between the CBO and the VW, $cos(\omega_{cbo}).cos(\omega_{vw})$ and to handle this, an additional term was incorporated represented here by N_{xy} [77]. The lifetime τ_{xy}, and the frequency, ω_{xy} were fixed at the values obtained from the results of regular Q-method fits since the amplitude of this frequency is small in ratio Q-method.

An additional relaxation term was included in the fit for the asymmetry parameter with a time constant τ_{rlx}. This was incorporated since the asymmetry parameter was drifting with time in the fit start time scan, shown in figure 5.6. This is hypothesized to be associated with an unknown slow effect which causes the drift in the time spectrum from early to late times. This slow effect can possibly be due to uncorrected drift in the pedestal leaking into the pedestal subtracted data, gain changes that haven't been accounted for or uncorrected residual pile-up effects. The exact source of this effect is still under investigation. The effect of including this term in fit-function on R is negligible (less than 10 ppb).

5.3 Fit Results

Once the proper form of fit-function was established, the ratio histogram was fit with this function. The ratio fit was performed using python **curve_fit** from package **scipy**. The ratio construction and covariance matrix calculation was done using ROOT. To cross-check the results, parallel fits were performed with randomized ratio method and regular Q-method which are described in section 5.4.

The starting point of the fit was $t = 30\mu s$ and the end time was $t = 305\mu s$ which meant the number of degrees of freedom (NDF) with 150 ns wide bins was 1835. The full fit function contained 26 parameters in case of Run-2 and Run-3a and 24 parameters in case of Run-3b. This meant the effective NDF for the fits were 1809 and 1811 respectively. The fit results of the datasets Run-2, Run-3a and Run-3b are summarized in Table 5.2. The fit results from individual datasets are also summarized in Table 1 of Appendix A.
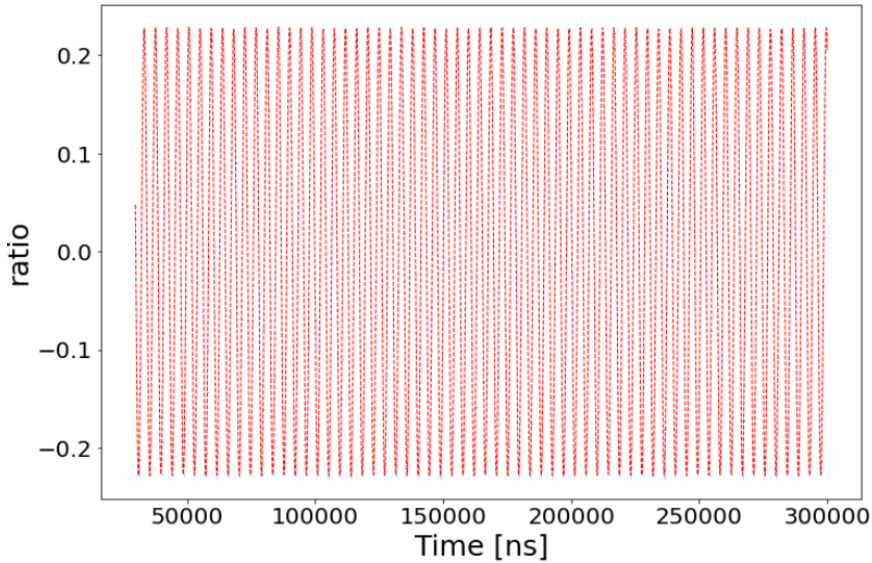
Figure 5.2: Fit to the Run-2 summed ratio histogram

Figure 5.3 shows the fit residuals defined as

$$R_i = \frac{y_i - f(x_i)}{\sigma_i} \tag{5.12}$$

where y_i is the data, $f(x_i)$ is the function value and σ_i is the uncertainty on the data-point at bin i. Figure 5.4 shows fourier transform (FT) of those residuals for fit to summed Run-2, Run-3a and Run-3b. The residuals and the FTs show no structure other than noise indicating a good fit to the ratio histogrammed data. The periodic

65

Table 5.2: Fit results of all the fit parameters in Run-2, Run-3a and Run-3b

	2	3a	3b
χ^2/NDF	1717/1809	1851/1809	1807/1811
R [ppm]	-44.476 ± 0.489	-35.308 ± 0.385	-33.985 ± 0.612
A	0.2289285 ± 0.0000167	0.2294122 ± 0.0000132	0.2282373 ± 0.0000209
ϕ	4.014185 ± 0.000075	4.023101 ± 0.000059	3.996710 ± 0.000093
A_{cbo}	0.00230 ± 0.00002	0.00186 ± 0.00002	0.00113 ± 0.00003
τ_{cbo} [μs]	253.68 ± 8.41	230.60 ± 7.11	209.92 ± 16.45
ω_{cbo} [rad/μs]	2.3412 ± 0.0004	2.3296 ± 0.0005	2.3312 ± 0.0004
ϕ_{cbo}	5.7719 ± 0.0566	5.9338 ± 0.0753	2.5735 ± 0.0298
A_{cbo_A}	0.00084 ± 0.00008	0.00040 ± 0.00006	0.00036 ± 0.00010
ϕ_{cbo_A}	5.74 ± 0.10	6.01 ± 0.17	2.26 ± 0.27
A_{cbo_ϕ}	0.00007 ± 0.00008	0.00008 ± 0.00006	0.00012 ± 0.00010
ϕ_{cbo_ϕ}	0.37 ± 1.09	3.82 ± 0.79	1.59 ± 0.86
A_{2cbo}	0.000124 ± 0.000016	0.000115 ± 0.000013	0.000026 ± 0.000022
ϕ_{2cbo}	2.81 ± 0.17	3.37 ± 0.19	3.45 ± 0.85
A_y	0.00020 ± 0.00003	0.00047 ± 0.00004	0.00075 ± 0.00011
τ_y [μs]	175.28 ± 56.12	85.34 ± 8.41	54.67 ± 7.21
ω_y [rad/μs]	13.930 ± 0.002	13.892 ± 0.001	13.900 ± 0.002
ϕ_y	5.90 ± 0.16	5.98 ± 0.08	2.68 ± 0.14
A_{VW}	0.0014 ± 0.0021	0.0042 ± 0.0007	0.0030 ± 0.0005
τ_{VW} [μs]	28.14 ± 2.66	15.47 ± 1.01	21.25 ± 1.91
ω_{VW} [rad/μs]	14.037 ± 0.003	14.100 ± 0.004	14.049 ± 0.004
ϕ_{VW}	4.26 ± 0.15	0.84 ± 0.16	1.96 ± 0.17
τ_{rlx} [μs]	304420 ± 63683	357500 ± 69176	587140 ± 297485
A_{cbo_t}	0.007 ± 0.002	0.005 ± 0.002	-
τ_{cbo_t} [μs]	19.9 ± 6.5	24.2 ± 7.7	-
$A_{1.9MHz}$	0.004 ± 0.003	0.004 ± 0.001	0.007 ± 0.004
$\phi_{1.9MHz}$	0.05 ± 0.77	0.99 ± 0.32	2.45 ± 0.55
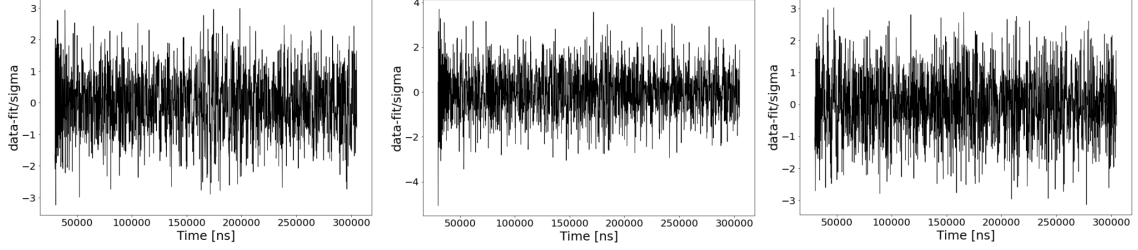
Figure 5.3: Run-2, Run-3a and Run-3b central fit residuals.
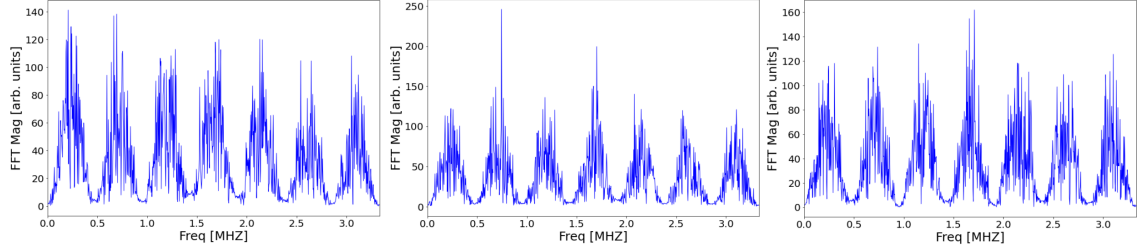
Figure 5.4: Run-2, Run-3a and Run-3b fourier transforms (FTs) of the residuals. The bumps correspond to the bin-to-bin correlation in the data as a result of the ratio construction.

structure in the FT come from bin-to-bin correlation as a result of the construction of ratio histogram using the copies of the same wiggle histogram as mentioned in section 4.2.3. The period of the oscillation in the FT is determined by the number of bins by which the time distribution was shifted for ratio construction. The oscillation period is equal to the number of bins in the histogram divided by the number of bins in the time shift. The construction of the ratio was done with a time shift of 14 (150 ns wide) bins which is roughly equivalent to half of the precession frequency period. So we observe 7 peaks in the FT. Since it becomes more difficult to see the smaller peaks in the FT in the presence of the periodic structure, the randomized ratio method was used to verify that no such peaks are being missed.

5.3.1   Start Time Scans

Fit start time scan in the range 30 μs to 105 μs was performed. The form of the fit-function was same as that was used for the central fits with some additional constraints to help the fit to converge. The vertical waist frequency and lifetime was kept fixed at the central fit value since the VW frequency decoheres quickly ($\sim 30\mu s$). The lifetime of the time dependent envelope for the CBO frequency was also kept constant at the central fit value. Figure 5.5 shows the start time scan for blind R for the three data groups. The error bars of the subsequent points on these plots are correlated to the previous points, so the allowed variation cannot be judged solely by looking at the error bars. The red line denotes the allowed statistical variation of one σ calculated

at each start time, t_i as

$$k(t_i) = p_{t_0} \pm \sqrt{\sigma_{t_i}^2 - \sigma_{t_0}^2} \qquad (5.13)$$

where p_{t_0} is the fit parameter value when fit start time is t_0, σ_{t_i} is the statistical precision on the fit parameter, p, when fit start time is t_i and σ_{t_0} is the statistical precision on p_{t_0}.

The scans of the other fit parameters were also well behaved. The asymmetry parameter and the CBO parameters showed a systematic variation with start time and as mentioned before additional terms for asymmetry relaxation and time dependence of CBO were introduced to correct that behavior. The scans of all the fit parameters are given in Appendix A.
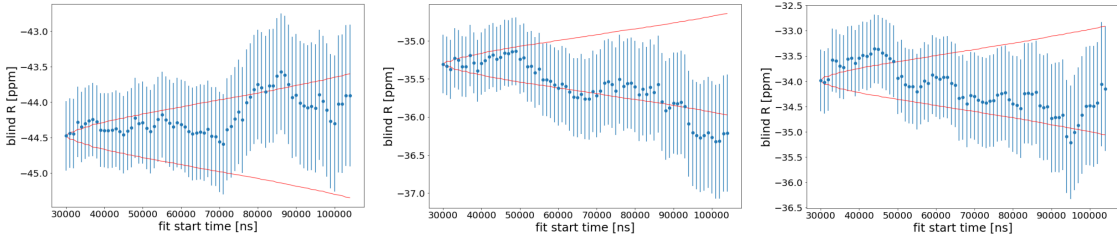
Figure 5.5: Run-2, Run-3a and Run-3b start time scan of blind R. The red lines show the band corresponding to 1 σ.
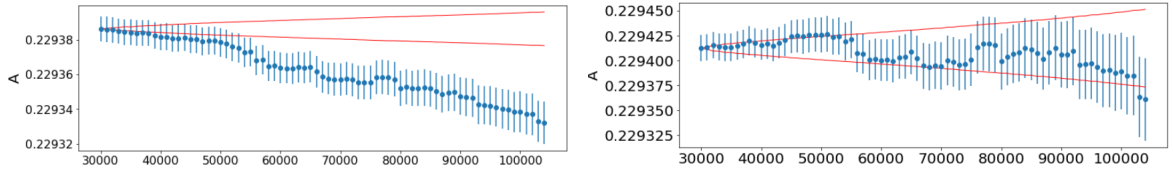
Figure 5.6: Asymmetry start time scan before (left) and after (right) relaxation term for Run-3a. Note that the vertical axis scale has shifted after including the asymmetry relaxation term.
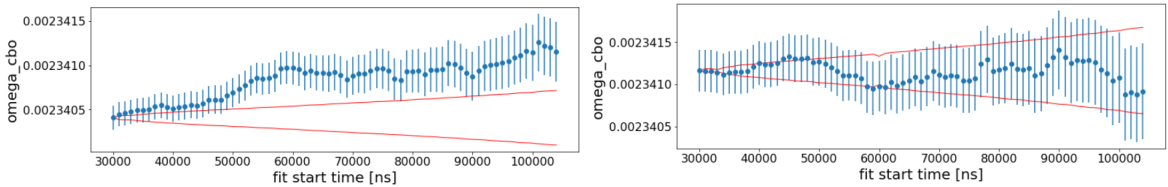
Figure 5.7: ω_{cbo} start time scan before and after time carying cbo frequency term in fit function in Run-2

5.3.2 Calorimeter Scans

Another important sanity check that can be performed is fitting individual calorimeters. The fit function used had the same form as the central fit function with certain parameters held constant to help the fit converge. For example the vertical oscillations are only visible at certain calorimeters [78] and hence the frequency and the lifetime of both VW and mean vertical oscillation were fixed at the central fit values. The fitted R values for the three datasets for per calorimeter fit are shown in figure 5.8. The calorimeter scans of all other fit parameters are given in Appendix A.
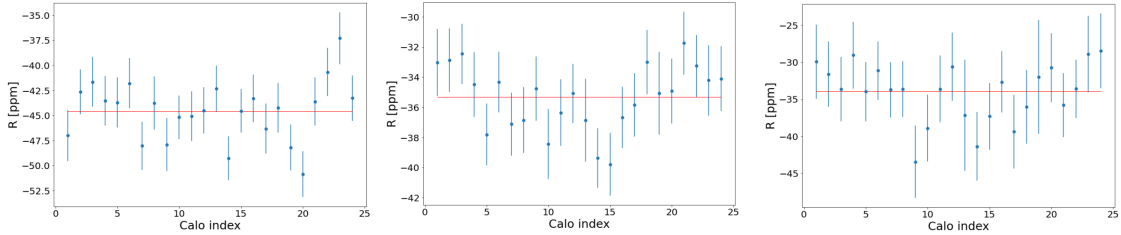
Figure 5.8: This figure shows blinded R vs calorimeter index. The error bars are inflated by multiplying them with the square root of their respective calorimeter fit. The red line shows a fit to a straight line.

The R versus calorimeter showed a wave pattern in Run-3a and Run-3b. This was determined to be related to the mismodelling of the CBO envelope in the per calorimeter fits. The amplitude of this wave is highly dependent on the parameter τ_{cbo_t}, that is the lifetime of the time dependence of ω_{cbo}. In the central fits, τ_{cbo_t} was found to be roughly $20\mu s$. But in the calorimeter scans if this parameter was fixed at a lower value such as $\sim 5\mu s$, then the amplitude of the wave could be reduced significantly [79] as shown in figure 5.9. For example in Run-3a, the amplitude of the wave was found to be 2.2 ppm if there was no time-dependent CBO envelope in the fit function, 1.7 ppm if the time dependent CBO envelope was included with a time constant of 24 μs (the parameter value obtained from central fit) and 0.8 ppm if the time constant of the time varying CBO envelope was fixed at 5.5 μs. The exact nature of the wave structure should be further investigated.

5.3.3 Per-Dataset Fits

The individual datasets were also fit and scans of the fit parameters per dataset was performed. The vertical waist and the mean vertical oscillation frequency and lifetime were kept fixed at their respective calorimeter sum fit result values. The asymmetry relaxation term or the 1.9 MHz frequency (N_{xy}) term was not included in the per dataset fits. Figure 5.10 shows blind R versus the individual datasets. All other parameters are given in Appendix A. Note that the hardware blinding is different between Run-2 and Run-3. Also, there was a significant amount of environmental temperature fluctuation during the course of Run-2 which may have caused the field
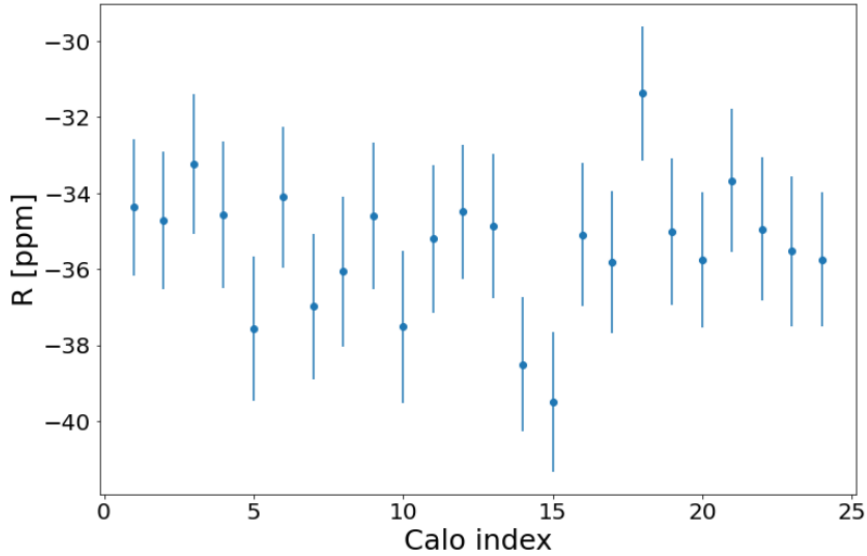
Figure 5.9: The wave pattern in Run-3a calo scan after putting in a time dependent CBO envelope with a time constant of 5.5 μs.

in the storage ring to drift. A much better stability in temperature was achieved during Run-3 data taking after the magnet was properly insulated.
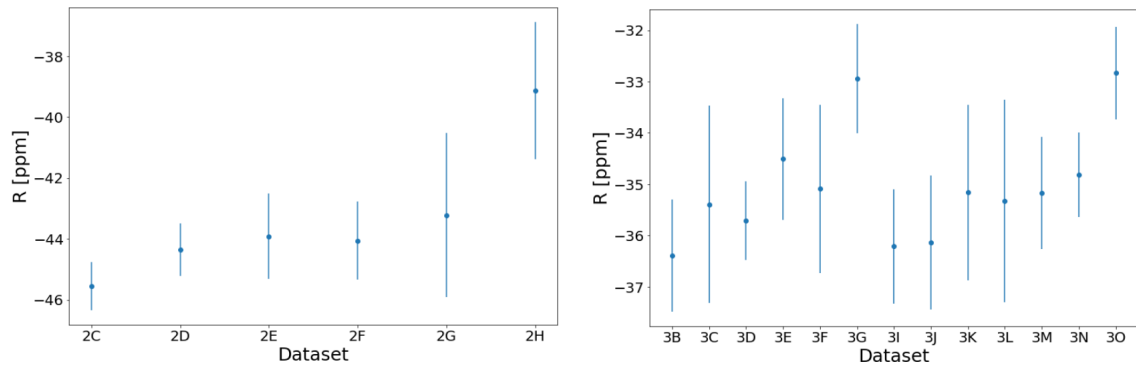
Figure 5.10: Plot of blind R versus the datasets of Run-2 and Run-3. Note that the hardware blinding is different in Run-2 and Run-3

5.4   Methods Comparisons

To establish the correctness of the ratio Q-method analysis, two parallel analyses were performed. One is the regular Q-method analysis. The details of the analysis techniques are already discussed in chapter 3. Additionally, ratio method histograms constructed using randomization were also analyzed. As discussed in section 4.2.1, each dataset was divided into 4 subsets which were independent of each other and

these subsets were then used for ratio construction. In both these cases the fast rotation correction leads to correlations between adjacent bins. For this the empirical calculation of the correlation coefficients was employed. The fits were performed in **ROOT** using the package **MINUIT**.
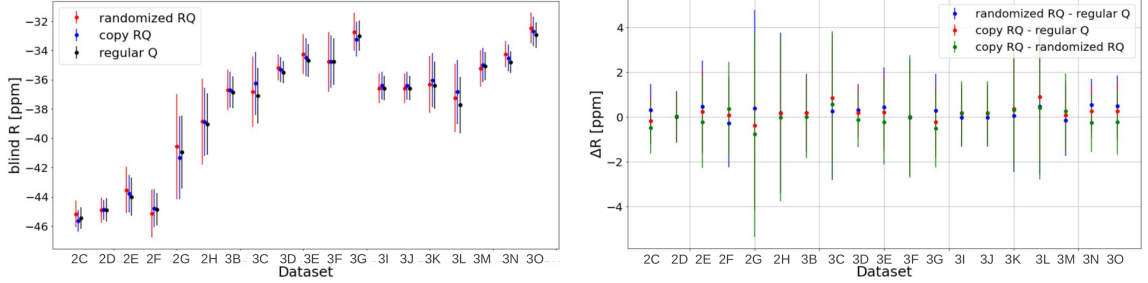
Figure 5.11: Comparison of blinded R for different Q-method analyses. The plot on the left shows the R-values obtained from fitting the individual Run-2 and Run-3 datasets using regular Q-method (black), copy ratio Q-method (red) and randomized ratio Q-method (blue). The plot on the right shows the difference between R-values obtained using three methods for the individual Run-2 and Run-3 datasets.

As shown in figure 5.11 all the differences between the three analyses are below $\sim$ 1 ppm. The size of the allowed difference between ratio and regular analyses scales with the statistics [80] and that is why the larger deviations are seen in the datasets which have low statistics. For example, for a dataset with statistics of 2C, allowed difference in the ratio and regular positron counting analysis is $\sim$ 80 ppb. Since, the Q-method is less precise than positron counting methods, the region of allowed differences is bigger for this analysis.

5.5   Impact of Correlated Bins on the Fit Results

Since the covariance matrix calculation described in chapter 4 is an approximation, it is important to look at the impact of such approximation on the fit results. Studies were performed by varying the off diagonal elements of the calculated covariance matrix to understand such effects. A scale factor was multiplied with the off diagonal elements of the covariance matrix and changes on the fitted value of R, precision over R and the chi-squared were evaluated. The range of variation of scaling factor was from 0.998 to 1.001. The matrix was no longer positive definite beyond this upper limit of 1.001. The change in R in Run-2 over this range was 6 ppb and σ_R changed by 17.5 ppb ($\sim 4\%$) as shown in figure 5.12. And as figure 5.13 shows, the corresponding change in χ^2 was by 120 units for a degree of freedom of 1812($\sim 7\%$).

It should be noted that in the region approaching the positive definite limit for the covariance matrix, the change in both χ^2 and σ_R is no longer linear. As a matter
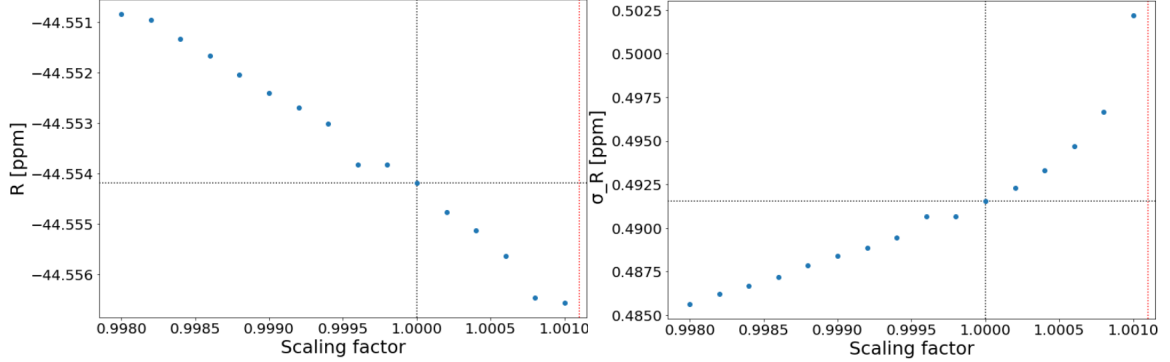
Figure 5.12: Figure on the left shows variation of R with a scaling factor of off-diagonal elements of the covariance matrix. Figure on the right shows the variation of sigma with the scaling factor of the off diagonal elements. The horizontal and vertical black dotted lines represent the fitted value of R without any scaling of the calculated covariance matrix elements. The vertical red dotted lines corresponds to highest possible scaling of off diagonal elements beyond which the matrix is no longer positive definite.

of fact, when the scaling factor goes from 1.000 to 1.001, σ_R increases by $\sim 2\%$ and correspondingly χ^2 increases by $\sim 4\%$. Systematic uncertainties will be assigned to address the impacts of approximation of bin-to-bin covariances.

5.6 Systematic Uncertainties

5.6.1 Ratio Construction

Choice of Muon lifetime

As mentioned in section 4.2.1, the weighting of the four component histograms for ratio construction requires knowledge of the muon lifetime, τ. The value used in the analysis is 64440 ns. A systematic study was done to determine the bias in blinded R as a result of the choice of this particular value of τ. To perform this study, full fit with a range of τ values for ratio construction was chosen. This scan was perfomed separately for the three datasets of Run-2 and 3. Figure 5.14 shows the fitted R values for various choices of τ in the range 64000 ns to 65000 ns for dataset 3a. The value of R was found to shift by ~ 6 ppb for Run-2, ~ 4 ppb for Run-3a and ~ 2 ppb in Run-3b.

5.6.2 Covariance Matrix for Fitting

As mentioned in section 5.5, the calculation of covariance matrix for fitting copy ratio method involves some approximations and thus a systematic uncertainty was assigned. The change in R was 6 ppb for a range of scaling factors (between 0.998 to 1.001) for the off-diagnonal matrix elements in Run-2. This was assigned to all the dataset since the procedure remains same.

72
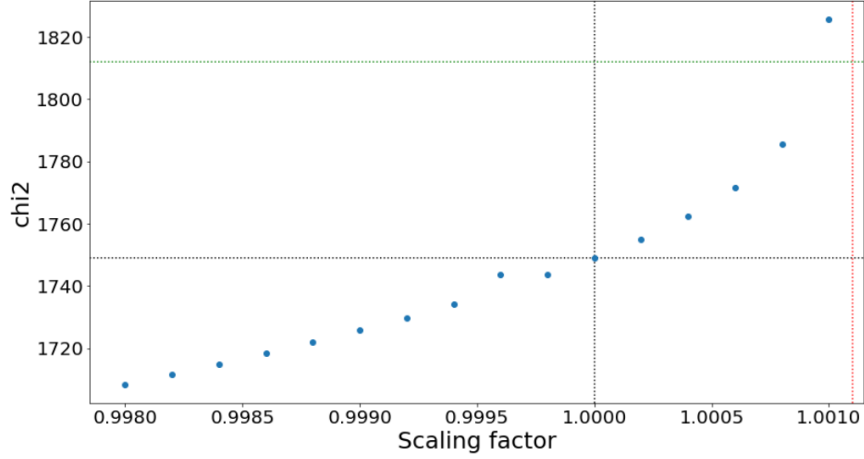
Figure 5.13: Fit Chi-squared versus scaling factor for off-diagonal elements of covariance matrix. The horizontal and vertical black dotted lines represent the fitted value of R without any scaling of the calculated covariance matrix elements. The vertical red dotted lines correspond to the highest possible scaling of off-diagonal elements beyond which the matrix is no longer positive definite. The horizontal dotted green line corresponds to a reduced chi-square of 1 which corresponds to a chi-square of 1812 on the vertical axis.
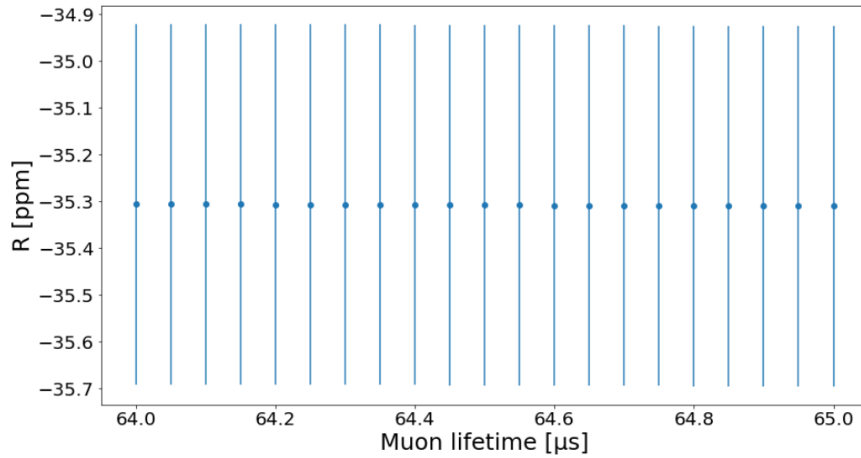
Figure 5.14: Blinded R versus various values of muon lifeitmes for Run-3a

5.6.3 Residual Early-to-Late Effect

As was done in Run-1, the residual early-to-late effect or the slow effect was determined by noting the change in the fitted value of R with a an extra term in the ratio fit function. The functional form of the fit function was

$$D(t) = 1 + Ae^{-t/\tau_D} \qquad (5.14)$$

73

Table 5.3: Various systematic uncertainties on R in Run-2 and Run-3 analysis usin
ratio Q-method where ratio was constructed using the copies of the same dataset

	Run-2 [ppb]	Run-3a [ppb]	Run-3b [ppb]
Muon Life-time	6	4	2
Covariance Matrix approximation	6	6	6
Slow term	7	13	39

The change in R in the 3 datasets, Run-2, Run-3a and Run-3b were 7 ppb, 13 ppb
and 39 ppb. These values are quoted as systematic uncertainties associated with slow
effect in the Run-2 and 3 analysis.

Chapter 6 Conclusion

6.1 Muon g-2 Run-1 Results

On 7th April 2021, the collaboration released its results of the Run-1 data taken in 2018. For the ω_a analysis there were 11 different results, 10 of which were analyzed using positron counting methods. The 11th analysis was using the integrated energy method and the analysis procedure has been briefly described in Chapter 3 of this dissertation. 4 out of the 10 positron counting methods were asymmetry weighted (A-method) analyses and thus had the best statistical precision. To minimize statistical uncertainty of the Run-1 result, these 4 A-method analyses were averaged over to obtain the final number for ω_a. The rest of the analyses, including the energy integrating analysis, served as cross checks and all the results were in agreement with each other. Since, the energy integrating method is the only method that does not reconstruct individual positron events and also has very different sensitivities to various systematic effects, it is the most different analysis procedure and a robust cross-check for the final ω_a result. Similarly, at least two parallel analyses were performed for each of the three steps that constitute magnetic field measurement viz. calibration, field tracking and muon weighting. The final unblinded ω_a and $\tilde{\omega}_p$ results of Run-1 datasets are summarized in table 6.1.

The final value of a_μ obtained after applying necessary corrections is given below

$$a_\mu^{FNAL} = 116592040(54) \times 10^{-11} \tag{6.1}$$

This value confirmed the findings of the BNL Muon g-2 experiment (E-821)

$$a_\mu^{BNL} = 116592080(63) \times 10^{-11} \tag{6.2}$$

The weighted average of the FNAL Run-1 and BNL final experimental values is

$$a_\mu^{Exp} = 116592061(41) \times 10^{-11} \tag{6.3}$$

Table 6.1: Run-1 final results of ω_a, $\tilde{\omega}_p$ and their ratios multiplied by 1000 per dataset [66] after unblinding.

Run	$\omega_a/2\pi$ [Hz]	$\tilde{\omega}_p/2\pi$ [Hz]	$(\omega_a/\tilde{\omega}_p)\times1000$
1a	229081.06 (28)	61791871.2 (7.1)	3.7073009 (45)
1b	229081.40 (24)	61791937.8 (7.9)	3.7073024 (38)
1c	229081.26 (19)	61791845.4 (7.7)	3.7073057 (31)
1d	229081.23 (16)	61791003.4 (6.6)	3.7072957 (26)
Run-1			3.7073003 (17)
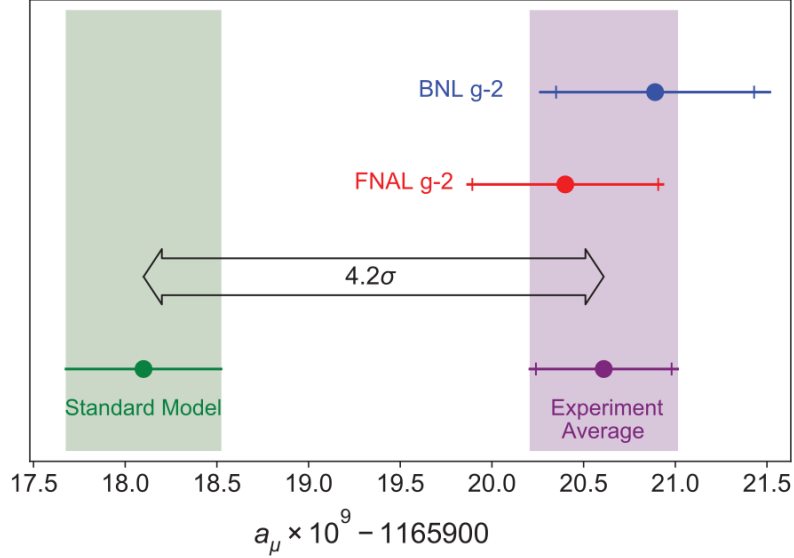
Figure 6.1: Figure showing the current theory prediction of a_μ in green, the BNL final result in blue, FNAL Run-1 result in red and the current experimental average in violet.

and the theoretical prediction as recommended by the *Muon g-2 Theory Initiative* white-paper is

$$a_\mu^{SM} = 116592089(63) \times 10^{-11} \tag{6.4}$$

The E-989 Run-1 results deviate from the Standard Model prediction by 3.3 σ and the E-989 and E-821 combined experimental value strengthens the discrepancy with the theoretical prediction to 4.2 σ as illustrated in figure 6.1. However one should note that the theoretical value recommended by the white-paper does not take into account the recent results from the lattice QCD calculation of the HVP contribution to a_μ^{SM}. If these new results are taken into account, the discrepancy with the experimental average is reduced to $\sim$1.5 σ.

6.2 Ratio Q-method Analysis of Run-2 and Run-3

As mentioned before, the Run-1 energy integrating analysis result suffered from systematic biases arising from slow variation in the data and to control this problem, the ratio histogramming technique was incorporated in the energy integrating analysis of the Run-2 and Run-3 data. The blinded analysis of the Run-2 and Run-3 data using the energy integrating ratio method has been concluded and the results are listed in table 6.2. The central fit results and sanity checks like start-time scans, calorimeter scans etc look encouraging and are detailed in chapter 5.

Table 6.2: Run-2 and Run-3 blinded results along with the statistical uncertainties. The results are also blinded with respect to other analysis methods employed in Run-2 and Run-3 analyses and cannot be directly compared. However, within the energy integrating analysis, the same analysis has been done in three different ways as mentioned in section 5.4 and all the central values agree well with each other as shown in figure 5.11

Run	R [ppm]	σ_R [ppm]
2	-44.476	0.489
3a	-35.308	0.385
3b	-33.985	0.612

Like in Run-1, for this data there are 7 independent analysis groups which performed parallel ω_a analyses and energy integrated ratio analysis is one the 7 groups. All the central values are still blinded. Some of the systematics have been evaluated as discussed and tabulated in section 5.6. With the introduction of the ratio histogramming, the systematic uncertainty from slow effects was reduced by an order of magnitude as discussed in section 5.6.3. As a result of this improvement, the Q-method ratio analysis has a similar scale of systematic effects as the other analysis groups and thus will serve as an important cross-check. In the analyses of the subsequent runs (Run-4 through Run-6), the overall uncertainties will be dominated by systematic uncertainties rather than the statistical uncertainties and consequently the significance of the ratio Q-method analysis as a cross-check will be more pertinent.

6.3   Outlook

The Muon g-2 experiment at Fermilab has already released its Run-1 results and is now on its way to publish the combined results from Run-2 and Run-3 in which the statistical uncertainty is projected to be ~ 200 ppb, a factor of 2 improvement over Run-1 statistical precision. If the central value does not move, the new results will be able to push the deviation of the experimental average to the 5 σ threshold with respect to the Muon g-2 Theory Initiative value. The experiment has also recently concluded taking the Run-5 data and a Run-6 is planned for the year 2022-23. All this combined will enable the experiment to accumulate more than 20 times the total data accumulated by the BNL experiment and improve the experimental precision four fold. The current status of the data accumulated by E-989 is shown in figure 6.2.

This dissertation has described the analysis of the Run-2 and the Run-3 data using a novel reconstruction technique called the energy integrating reconstruction which was used for the first time in the Run-1 analysis. The author has further improved the analysis procedure by incorporating a new ratio histogramming technique which was so far only limited to positron counting methods. The combination of the new
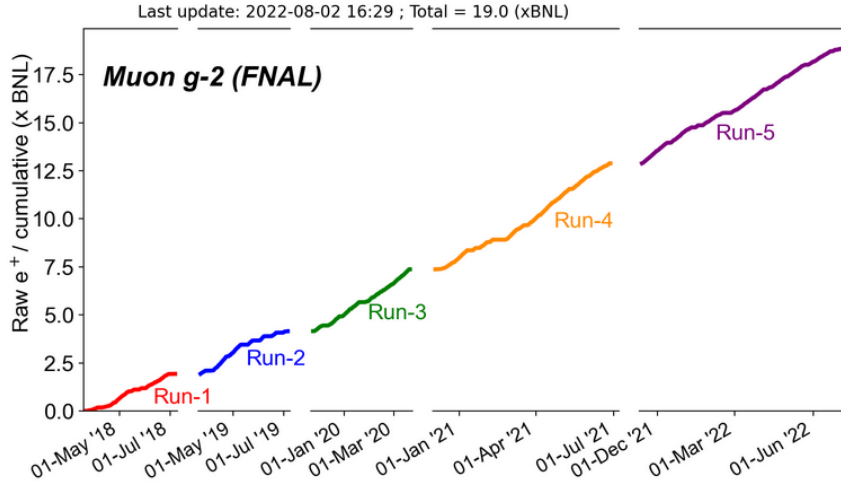
Figure 6.2: Figure showing the data collected by E-989 from Run-1 through Run-5 in units of total data collected by E-821. The total data collected by the end of Run-5 is 19 times the total data collected by the BNL experiment.

reconstruction method with the ratio histogramming technique provides a unique alternative determination of anomalous spin precession frequency of the muon in E-989. As the experiment collects more data and reduces the statistical uncertainty, the energy integrating ratio analysis for validating the anomalous precession frequency results will gather increased importance.

Appendices

Appendix A: Supplmentary Plots and Fit Parameters from Run-2 and Run-3 Analyses using Integrated Energy Ratio Method
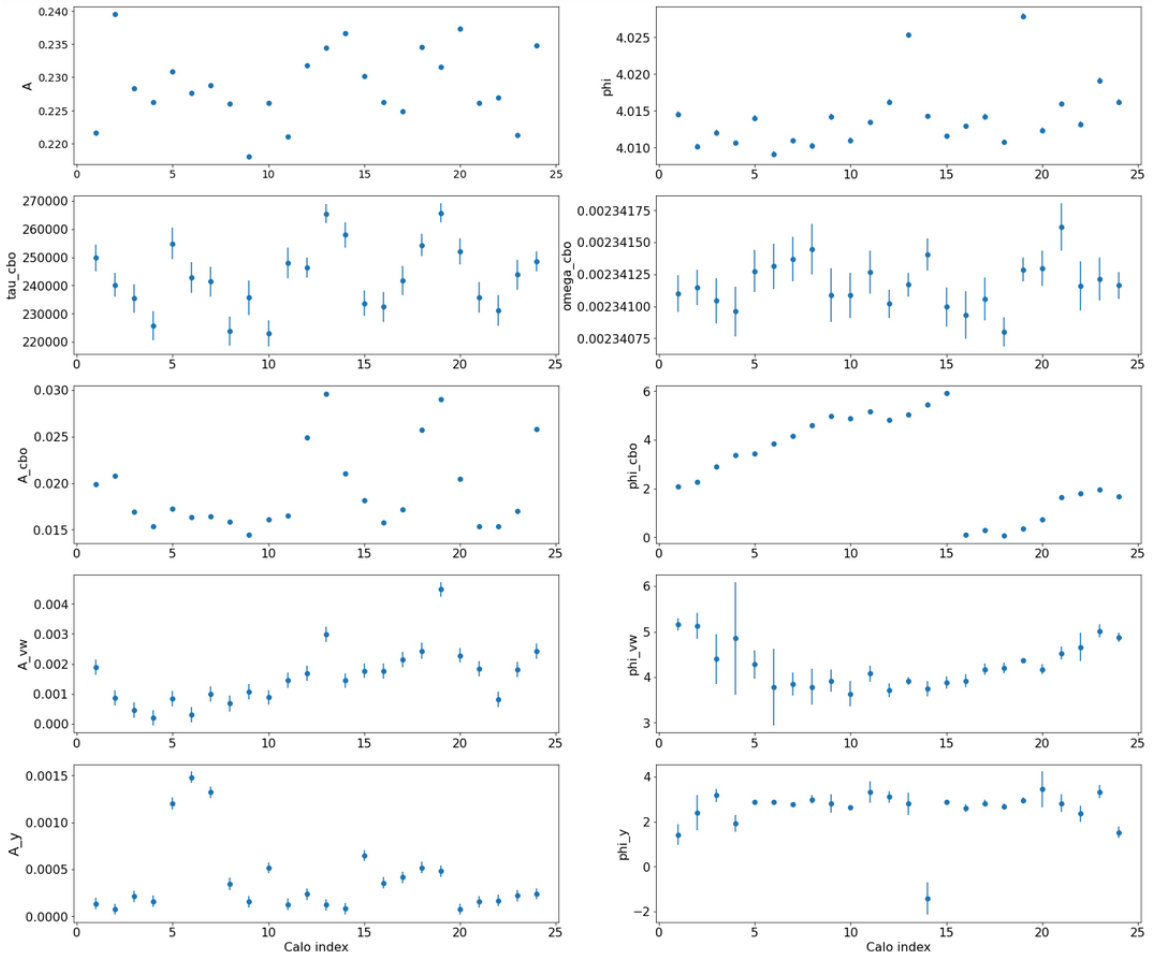
Figure 1: Run-2 calorimeter scans of all the fits parameters in the fit function
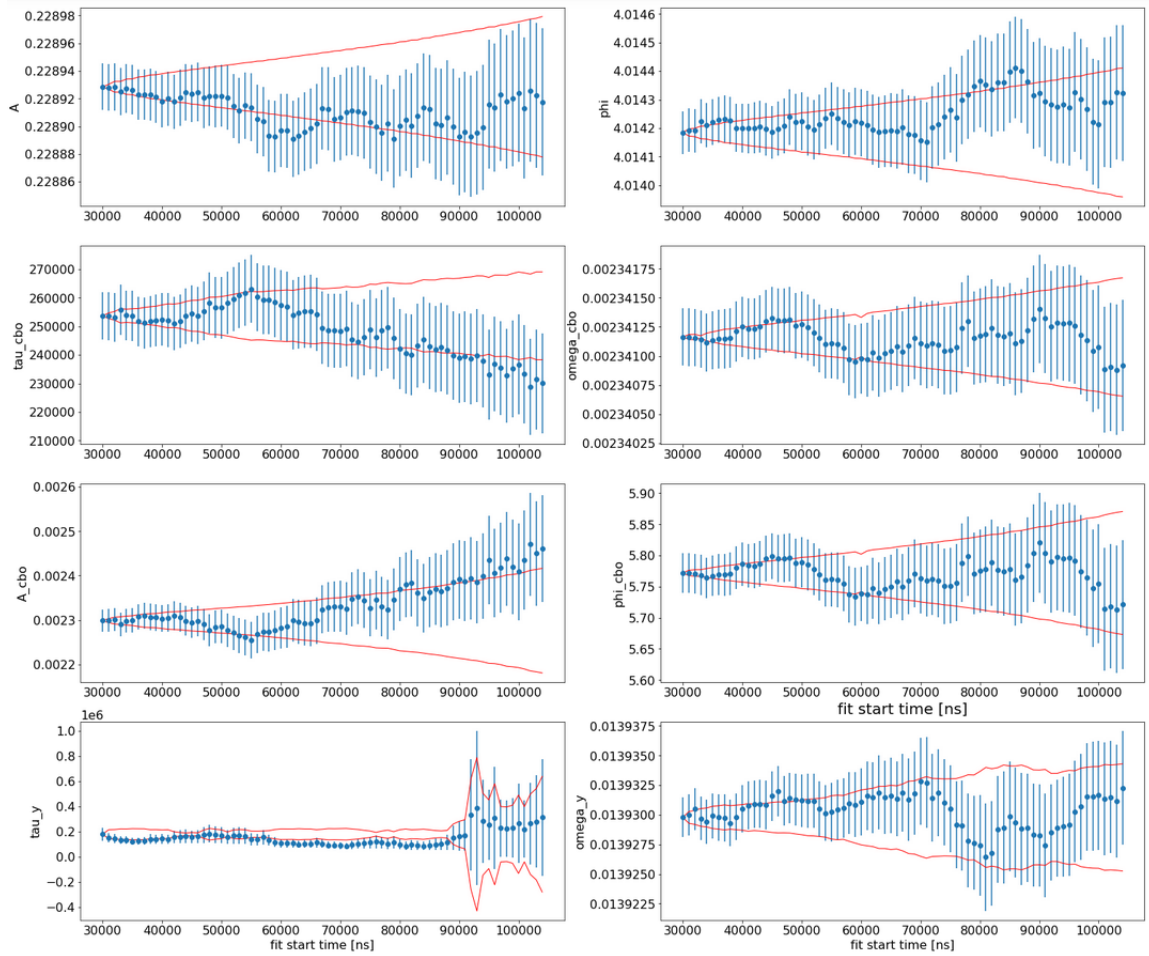
Figure 2: Run-2 start time scans of all the parameters in the fit function
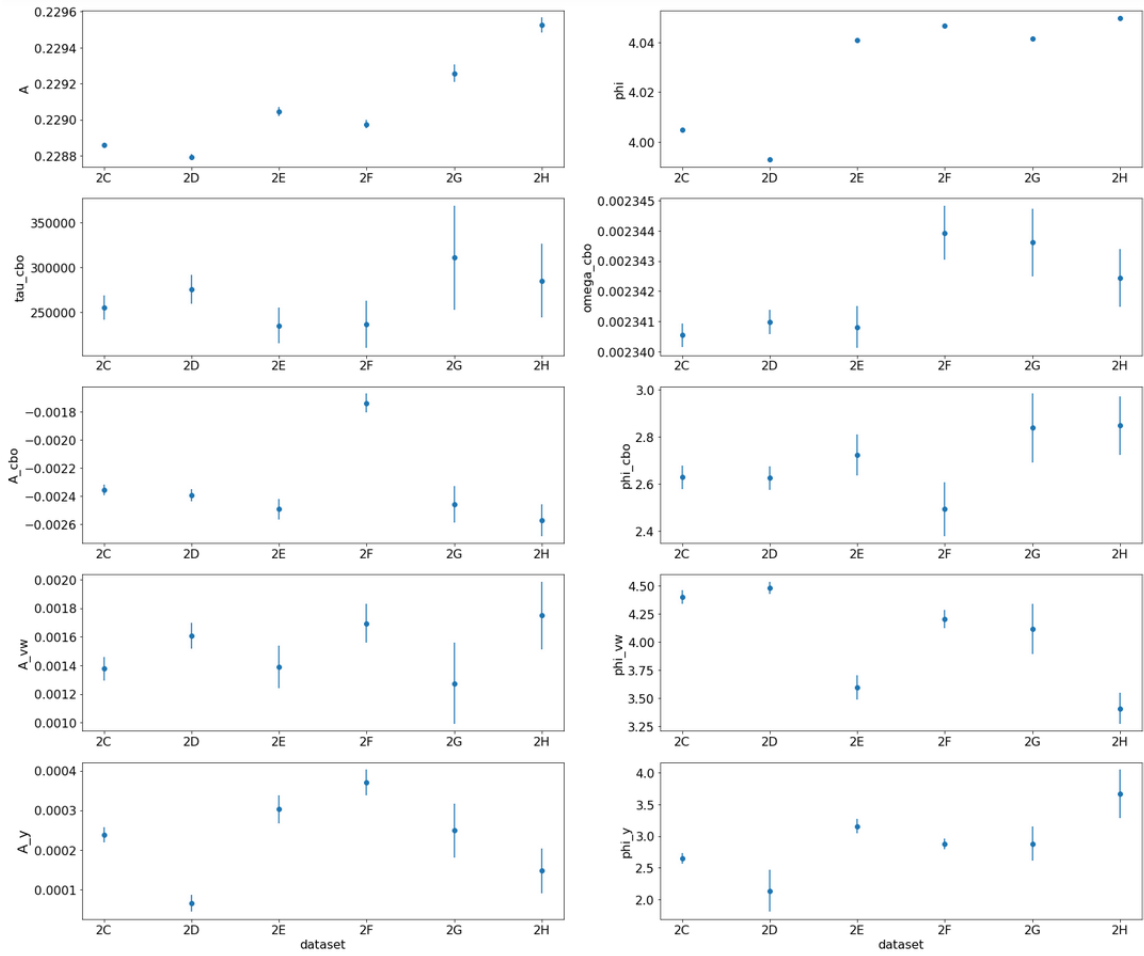
Figure 3: Run-2 dataset scan of all the parameters in the fit function
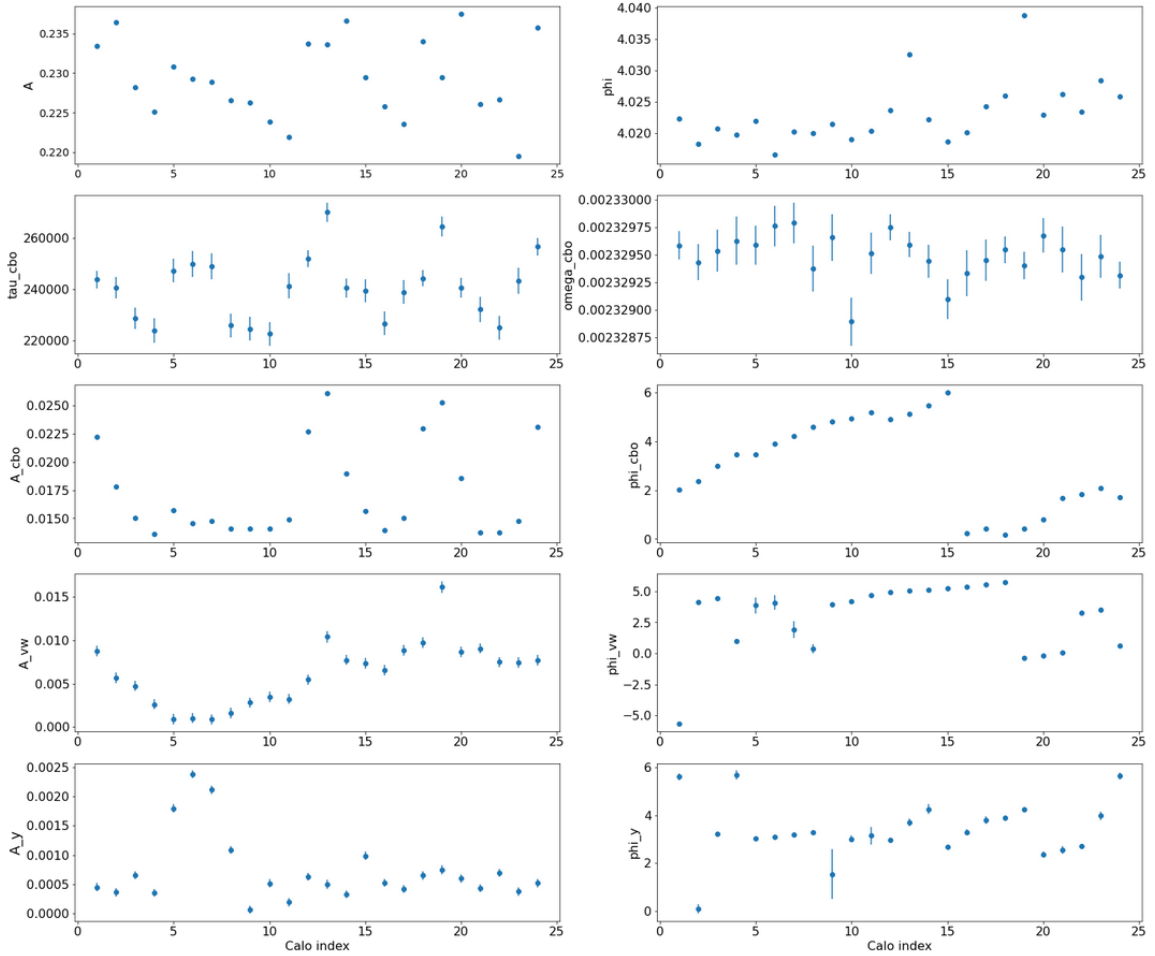
Figure 4: Run-3a calorimeter scan of all the fits parameters in the fit function
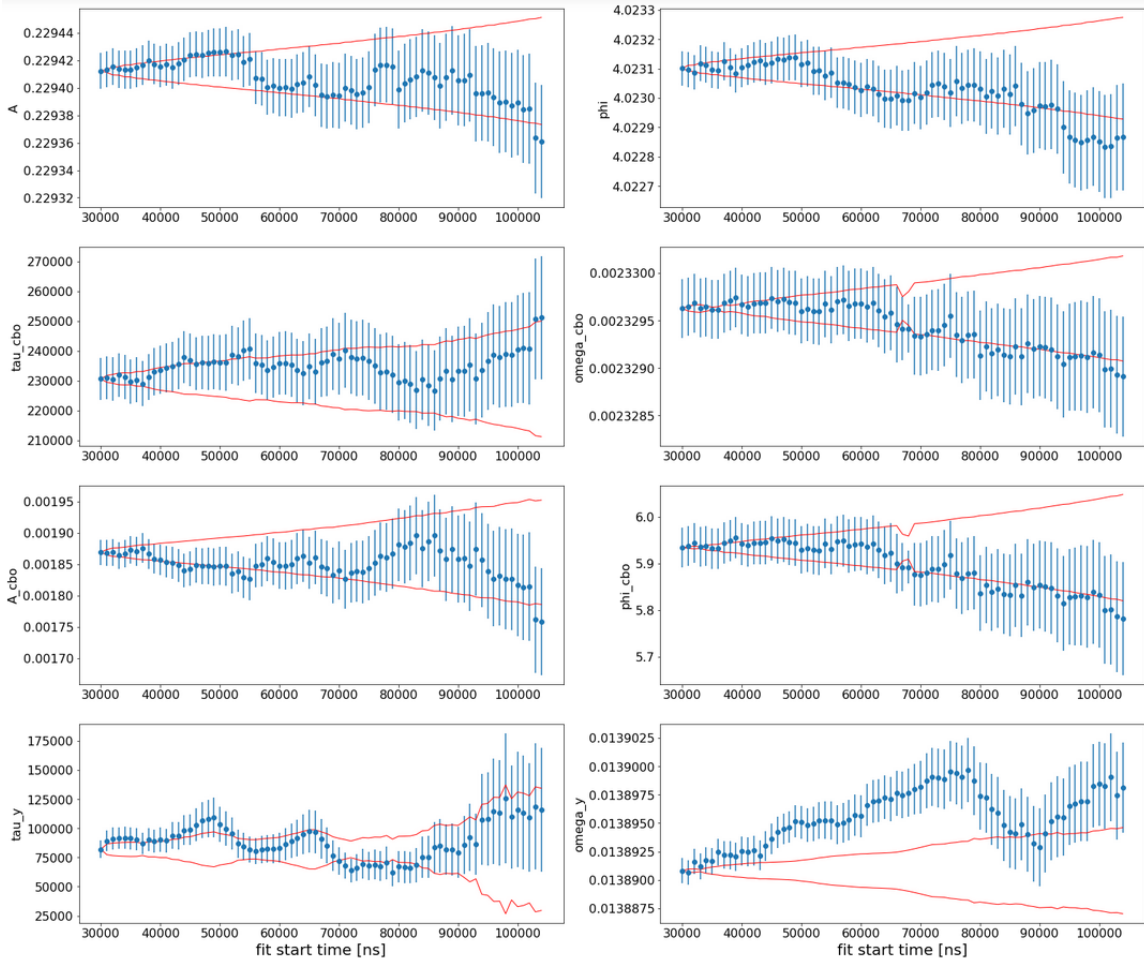
Figure 5: Run-3a start time scans of all the parameters in the fit function
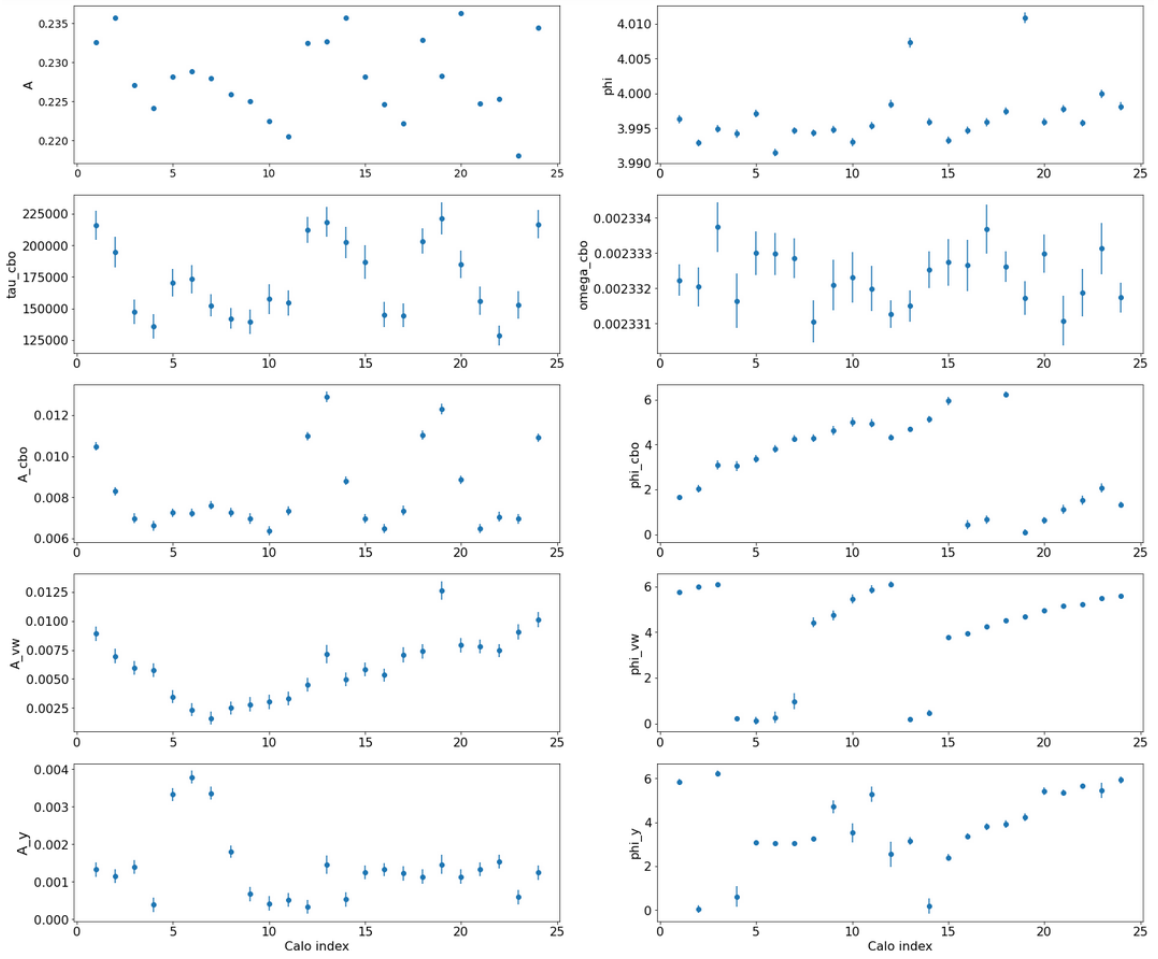
Figure 6: Run-3b calorimeter scan of all the fits parameters in the fit function

Figure 7: Run-3b start time scans of all the parameters in the fit function
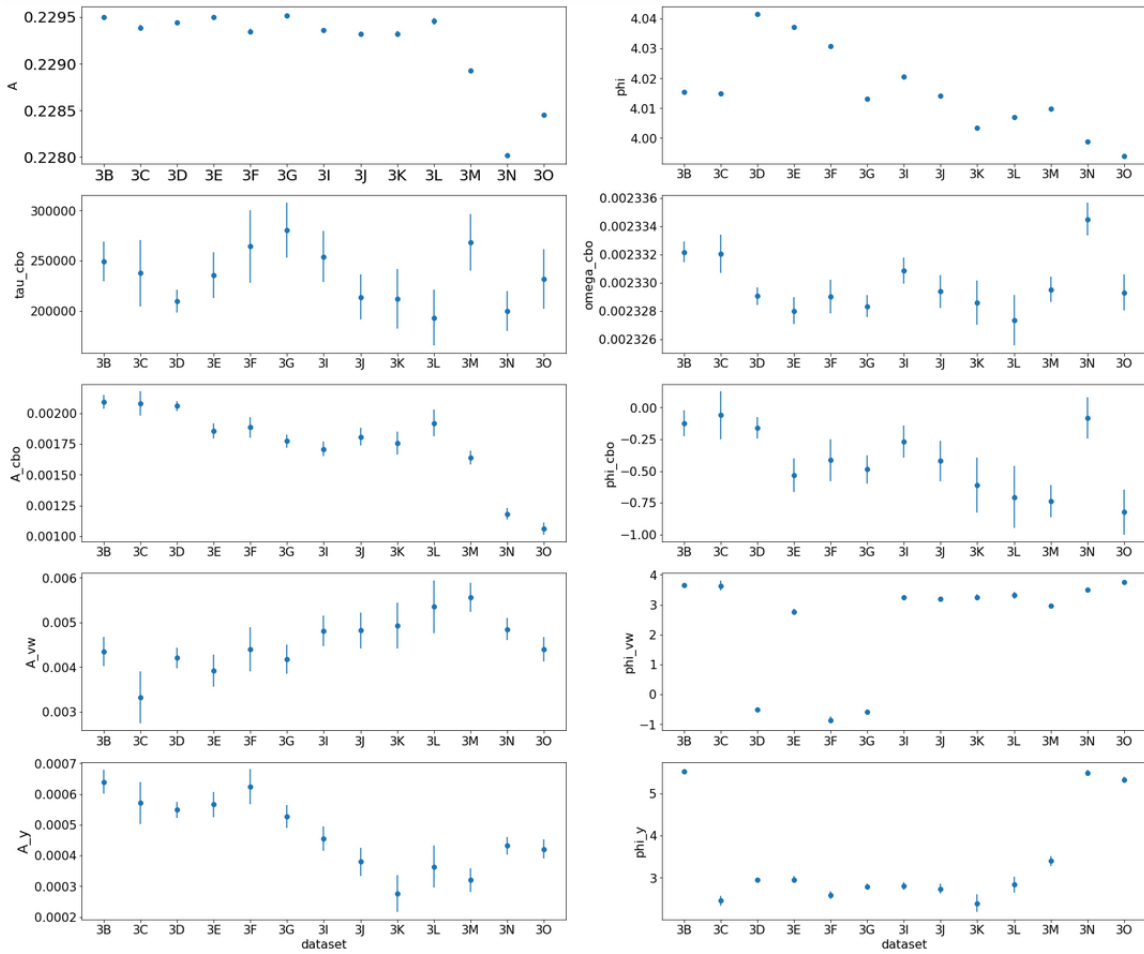
Figure 8: Run-3 dataset scan of all the parameters in the fit function

Table 1: Run-2 per dataset fit results. The frequency and lifetime of vertical mean oscillation and vertical waist terms were kept fixed at the Run-2 central fit results for the individual dataset.

|	2C	2D	2E	2F	2G	2H
χ^2/NDF	1636/1817	1672/1817	1675/1817	1682/1817	1597/1817	1572/1817
R [ppm]	-45.557 ± 0.79	-44.364 ± 0.863	-43.918 ± 1.402	-44.06 ± 1.291	-43.223 ± 2.702	-39.131 ± 2.262
A	0.22886 ± 0.00001	0.22879 ± 0.00002	0.22905 ± 0.00003	0.22897 ± 0.00002	0.22926 ± 0.00005	0.22953 ± 0.00004
ϕ	4.00488 ± 0.00012	3.99294 ± 0.00013	4.04098 ± 0.00021	4.04674 ± 0.00020	4.04136 ± 0.00041	4.04958 ± 0.00035
A_{cbo}	0.00236 ± 0.00004	0.00239 ± 0.00004	0.00249 ± 0.00007	0.00174 ± 0.00007	0.00246 ± 0.00013	0.00257 ± 0.00011
τ_{cbo} [μs]	255 ± 13	275 ± 16	235 ± 20	236 ± 26	311 ± 58	285 ± 41
ω_{cbo} [rad/μs]	2.3405 ± 0.0004	2.3410 ± 0.0004	2.3408 ± 0.0007	2.3439 ± 0.0009	2.3436 ± 0.0011	2.3424 ± 0.0009
ϕ_{cbo}	2.629 ± 0.050	2.625 ± 0.051	2.723 ± 0.088	2.493 ± 0.114	2.838 ± 0.147	2.848 ± 0.123
A_{cbo_A}	0.00066 ± 0.00012	0.00071 ± 0.00013	0.00077 ± 0.00022	0.00174 ± 0.00021	0.00079 ± 0.00040	0.00062 ± 0.00034
ϕ_{cbo_A}	2.50 ± 0.19	0.46 ± 0.19	2.66 ± 0.30	2.66 ± 0.16	0.20 ± 0.52	0.08 ± 0.55
A_{cbo_ϕ}	0.00012 ± 0.00012	0.00011 ± 0.00013	0.00020 ± 0.00022	0.00042 ± 0.00020	0.00056 ± 0.00040	0.00029 ± 0.00034
ϕ_{cbo_ϕ}	0.38 ± 1.06	-2.74 ± 1.19	2.39 ± 1.12	27.84 ± 0.51	9.80 ± 0.73	2.38 ± 1.20
A_y	0.00024 ± 0.00002	0.00007 ± 0.00002	0.00030 ± 0.00004	0.00037 ± 0.00003	0.00025 ± 0.00007	0.00015 ± 0.00006
τ_y [μs]	175.334 (fixed)	175.334 (fixed)	175.334 (fixed)	175.334 (fixed)	175.334 (fixed)	175.334 (fixed)
ω_y [rad/μs]	13.93 (fixed)	13.93 (fixed)	13.93 (fixed)	13.93 (fixed)	13.93 (fixed)	13.93 (fixed)
ϕ_y	2.65 ± 0.08	2.13 ± 0.33	3.16 ± 0.12	2.88 ± 0.09	2.88 ± 0.27	3.67 ± 0.39
A_{VW}	0.00138 ± 0.00008	0.00161 ± 0.00009	0.00139 ± 0.00015	0.00169 ± 0.00014	0.00127 ± 0.00028	0.00175 ± 0.00024
τ_{VW} [μs]	28.138 (fixed)	28.138 (fixed)	28.138 (fixed)	28.138 (fixed)	28.138 (fixed)	28.138 (fixed)
ω_{VW} [rad/μs]	14.037 (fixed)	14.037 (fixed)	14.037 (fixed)	14.037 (fixed)	14.037 (fixed)	14.037 (fixed)
ϕ_{VW}	4.40 ± 0.06	4.48 ± 0.06	3.60 ± 0.11	4.20 ± 0.08	4.11 ± 0.22	3.41 ± 0.14

Table 2: Run-3 per dataset fit results. The frequency and lifetime of vertical mean oscillation and vertical waist terms were kept fixed at the Run-3 central fit results for the individual dataset.

	3B	3C	3D	3E	3F	3G	3I	3J	3K	3L	3M	3N	3O
χ^2/NDF	1619/1817	1590/1817	1712/1817	1714/1817	1621/1817	1580/1817	1646/1817	1643/1817	1729/1817	1682/1718	1621/1817	1882/1817	1718/1817
R [ppm]	-36.392 ± 1.096	-35.396 ± 1.919	-35.705 ± 0.761	-34.509 ± 1.189	-35.089 ± 1.64	-32.941 ± 1.068	-36.214 ± 1.119	-36.137 ± 1.307	-35.156 ± 1.705	-35.328 ± 1.966	-35.17 ± 1.087	-34.821 ± 0.828	-32.841 ± 0.907
A	0.22949 ± 0.00002	0.22938 ± 0.00003	0.22944 ± 0.00001	0.2295 ± 0.00002	0.22934 ± 0.00003	0.22952 ± 0.00002	0.22936 ± 0.00002	0.22932 ± 0.00002	0.22932 ± 0.00003	0.22946 ± 0.00004	0.22893 ± 0.00002	0.22802 ± 0.00001	0.22845 ± 0.00002
ϕ	4.01552 ± 0.00017	4.01484 ± 0.00029	4.0416 ± 0.00012	4.03723 ± 0.00018	4.03087 ± 0.00025	4.01306 ± 0.00016	4.02054 ± 0.00017	4.01408 ± 0.00020	4.0035 ± 0.00026	4.00692 ± 0.00030	4.00993 ± 0.00017	3.99879 ± 0.00013	3.99395 ± 0.00014
A_{cbo}	0.00209 ± 0.00006	0.00208 ± 0.00010	0.00206 ± 0.00004	0.00185 ± 0.00006	0.00189 ± 0.00008	0.00177 ± 0.00005	0.00171 ± 0.00006	0.00181 ± 0.00007	0.00176 ± 0.00009	0.00192 ± 0.00011	0.00164 ± 0.00005	0.00118 ± 0.00005	0.00106 ± 0.00005
τ_{cbo} [μs]	249 ± 20	238 ± 33	210 ± 11	236 ± 23	264 ± 37	280 ± 28	254 ± 26	214 ± 22	212 ± 30	193 ± 28	268 ± 28	200 ± 20	232 ± 30
ω_{cbo} [rad/μs]	2.3322 ± 0.0007	2.3320 ± 0.0014	2.3290 ± 0.0006	2.3280 ± 0.0009	2.3290 ± 0.0012	2.3283 ± 0.0008	2.3308 ± 0.0009	2.3294 ± 0.0012	2.3286 ± 0.0016	2.3273 ± 0.0018	2.3295 ± 0.0009	2.3345 ± 0.0012	2.3293 ± 0.0013
ϕ_{cbo}	-0.125 ± 0.104	-0.061 ± 0.188	-0.159 ± 0.082	-0.530 ± 0.132	-0.416 ± 0.167	-0.486 ± 0.112	-0.271 ± 0.128	-0.422 ± 0.158	-0.613 ± 0.215	-0.705 ± 0.243	-0.736 ± 0.126	-0.082 ± 0.162	-0.822 ± 0.178
A_{cbo_A}	0.00022 ± 0.00017	0.00014 ± 0.00030	0.00045 ± 0.00012	0.00050 ± 0.00019	0.00039 ± 0.00025	-0.00068 ± 0.00016	0.00010 ± 0.00017	-0.00072 ± 0.00021	0.00050 ± 0.00028	0.00024 ± 0.00033	-0.00066 ± 0.00017	-0.00040 ± 0.00014	-0.00030 ± 0.00014
ϕ_{cbo_A}	-0.27 ± 0.75	1.27 ± 2.22	0.44 ± 0.29	-0.29 ± 0.40	-0.59 ± 0.66	2.22 ± 0.26	0.44 ± 1.74	2.18 ± 0.33	-0.33 ± 0.59	0.13 ± 1.39	2.54 ± 0.28	2.79 ± 0.38	1.90 ± 0.50
A_{cbo_ϕ}	0.00015 ± 0.00017	0.00008 ± 0.00030	0.00010 ± 0.00013	0.00029 ± 0.00019	0.00021 ± 0.00025	0.00017 ± 0.00016	0.00014 ± 0.00018	0.00028 ± 0.00022	0.00005 ± 0.00028	0.00010 ± 0.00034	0.00028 ± 0.00017	0.00008 ± 0.00014	0.00018 ± 0.00014
ϕ_{cbo_ϕ}	0.05 ± 1.11	-0.10 ± 3.68	0.48 ± 1.29	2.50 ± 0.67	-0.17 ± 1.21	1.86 ± 0.95	0.75 ± 1.27	0.69 ± 0.77	2.60 ± 6.08	-12.32 ± 3.35	0.52 ± 0.60	1.40 ± 1.69	1.65 ± 0.84
A_y	0.00063 ± 0.00004	0.00057 ± 0.00007	0.00055 ± 0.00003	0.00057 ± 0.00004	0.00062 ± 0.00006	0.00053 ± 0.00004	0.00045 ± 0.00004	0.00038 ± 0.00005	0.00027 ± 0.00006	0.00036 ± 0.00007	0.00032 ± 0.00004	0.00042 ± 0.00003	0.00041 ± 0.00003
τ_y [μs]	85.337 (fixed)	85.337 (fixed)	85.337 (fixed)	85.337 (fixed)	85.337 (fixed)	85.337 (fixed)	85.337 (fixed)	85.337 (fixed)	85.337 (fixed)	85.337 (fixed)	85.337 (fixed)	85.337 (fixed)	85.337 (fixed)
ω_y [rad/μs]	13.891 (fixed)	13.891 (fixed)	13.891 (fixed)	13.891 (fixed)	13.891 (fixed)	13.891 (fixed)	13.891 (fixed)	13.891 (fixed)	13.891 (fixed)	13.891 (fixed)	13.891 (fixed)	13.891 (fixed)	13.891 (fixed)
ϕ_y	5.52 ± 0.06	2.46 ± 0.12	2.97 ± 0.05	2.97 ± 0.07	2.59 ± 0.09	2.80 ± 0.07	2.82 ± 0.09	2.75 ± 0.12	2.42 ± 0.22	2.86 ± 0.19	3.42 ± 0.12	5.49 ± 0.07	5.32 ± 0.08
A_{VW}	0.00434 ± 0.00033	0.00333 ± 0.00058	0.00421 ± 0.00023	0.00394 ± 0.00036	-0.00439 ± 0.00049	0.00419 ± 0.00032	0.00479 ± 0.00034	0.00480 ± 0.00039	0.00491 ± 0.00051	0.00535 ± 0.00059	0.00556 ± 0.00033	0.00477 ± 0.00025	0.00433 ± 0.00027
τ_{VW} [μs]	15.47 (fixed)	15.47 (fixed)	15.47 (fixed)	15.47 (fixed)	15.47 (fixed)	15.47 (fixed)	15.47 (fixed)	15.47 (fixed)	15.47 (fixed)	15.47 (fixed)	15.47 (fixed)	15.47 (fixed)	15.47 (fixed)
ω_{VW} [rad/μs]	14.099 (fixed)	14.099 (fixed)	14.099 (fixed)	14.099 (fixed)	14.099 (fixed)	14.099 (fixed)	14.099 (fixed)	14.099 (fixed)	14.099 (fixed)	14.099 (fixed)	14.099 (fixed)	14.099 (fixed)	14.099 (fixed)
ϕ_{VW}	3.85 ± 0.08	3.82 ± 0.17	2.82 ± 0.05	2.95 ± 0.09	-0.68 ± 0.11	2.74 ± 0.08	3.42 ± 0.07	3.37 ± 0.08	3.42 ± 0.10	3.50 ± 0.11	3.15 ± 0.06	3.69 ± 0.05	3.93 ± 0.06

88

Bibliography

[1] J. D Jackson *Classical Electrodynamics* Wiley, 2016

[2] J. J Sakurai *Modern Quantum Mechanics* Pearson, 2012

[3] M. E. Peskin and D. V. Schroeder *An Introduction to Quantum Field Theory* Levant, 2005

[4] G. E. Uhlenbeck and S. A. Goudsmit, Die Naturwissenschaften, 13, 953-954 (1925)

[5] W. Gerlach and O. Stern, *The magnetic moment of the silver atom* Zeitschrift fr Physik, 9, 353-355. (1922)

[6] L. H. Thomas, *The motion of the spinning electron* Nature 117, 514 (1926)

[7] L. H. Thomas, *The kinematics of an electron with an axis* Lond. Edinb. Dublin Philos. Mag. J. Sci. 3, 1 (1927)

[8] P. A. M. Dirac *The quantum theory of the electron* Proceedings of Royal Society A, Volume 117, Issue 778 (1928)

[9] R. Frisch and O. Stern *Magnetic Deviation of Hydrogen Molecules and the Magnetic Moment of the Proton I* Zeitschrift fr Physik, 85, 416.

[10] I. Estermann and O. Stern *Magnetic Deviation of Hydrogen Molecules and the Magnetic Moment of the Proton II* Zeitschrift fr Physik, 85, pages 1724 (1933)

[11] L. W. Alvarez and F. Bloch *A Quantitative Determination of the Neutron Moment in Absolute Nuclear Magnetons* Phys. Rev. 57, 111 Published 15 January 1940

[12] P. Kusch and H.M Foley, *Precision Measurement of the Ratio of the Atomic 'g Values' in the $^2P_{\frac{3}{2}}$ and $^2P_{\frac{1}{2}}$ States of Gallium* Phys. Rev 72, 1256 (1947)

[13] J.E. Nafe, E.B. Nelson and I.I. Rabi, *The Hyperfine Structure of Atomic Hydrogen and Deuterium* Phys. Rev. 71, 914(1947)

[14] D.E. Nagel, R.S. Julian and J.R. Zacharias, *The Hyperfine Structure of Atomic Hydrogen and Deuterium* Phys. Rev. 72, 971 (1947)

[15] J. Schwinger, *On Quantum-Electrodynamics and the Magnetic Moment of the Electron* Phys. Rev. 73, 416 Published 15 February 1948

[16] P. Kusch, *The magnetic moment of the electron* Nobel Lecture, December 12, 1955

[17] C. D. Anderson and S. H. Neddermeyer, *Cloud Chamber Observations of Cosmic Rays at 4300 Meters Elevation and Near Sea-Level* Phys. Rev. 50, 263 Published 15 August 1936

[18] J. C. Street and E. C. Stevenson, *New Evidence for the Existence of a Particle of Mass Intermediate Between the Proton and Electron* Phys. Rev. 52, 1003 Published 1 November 1937

[19] M. Conversi, E. Pancini, AND O. Picconic *On the Disintegration of Negative Mesons* Phys. Rev. 71, 209 Published 1 February 1947

[20] File:Standard Model of Elementary Particles.svg . link

[21] F. Jegerlehner and A. Nyffeler, *The Muon g-2* Phys. Rep. 477, 1 (2009)

[22] T. Aoyama, et al. *The anomalous magnetic moment of the muon in the Standard Model* Physics Reports Volume 887, 3 December 2020

[23] T. Aoyama, M. Hayakawa, T. Kinoshita, and M. Nio *Complete Tenth-Order QED Contribution to the Muon g-2* Phys. Rev. Lett. 109, 111808 Published 13 September 2012

[24] A. Czarnecki, W. J. Marciano and A. Vainshtein *Refinements in electroweak contributions to the muon anomalous magnetic moment* Phys. Rev. D, 73 (2006), p. 119901

[25] R. H. Parker *Measurement of the fine-structure constant as a test of the Standard Model* Science, 360 (2018)

[26] M. Davier, A. Hoecker, B. Malaescu and Z. Zhang *Reevaluation of the hadronic vacuum polarisation contributions to the Standard Model predictions of the muon g-2 and $\alpha(m_Z^2)$ using newest hadronic cross-section data* , European Physical Journal C 77, 827 (2017)

[27] M. Davier, A. Hoecker, B. Malaescu, and Z. Zhang *A new evaluation of the hadronic vacuum polarisation contributions to the muon anomalous magnetic moment and to $\alpha(m_Z^2)$* European Physical Journal C 80, 241 (2020)

[28] A. Keshavarzi, D. Nomura and T. Teubner *g-2 of charged leptons, $\alpha(m_Z^2)$, and the hyperfine splitting of muonium* Phys. Rev. D 101, 014029 Published 29 January 2020

[29] A. Keshavarzi, D. Nomura and T. Teubner *Muon g-2 and $\alpha(m_Z^2)$: A new data-based analysis* Phys. Rev. D 97, 114025 Published 25 June 2018

[30] S. Borsanyi et al., *Leading hadronic contribution to the muon magnetic moment from lattice QCD* Nature 593 (2021) 51

[31] M. Cè et al., *Window observable for the hadronic vacuum polarization contribution to the muon g 2 from lattice QCD* arXiv:2206.06582.

[32] C. Alexandrou et al., *Lattice calculation of the short and intermediate time-distance hadronic vacuum polarization contributions to the muon magnetic moment using twisted-mass fermions* arXiv:2206.15084

[33] C. S. Wu, E. Ambler, R. W. Hayward, D. D. Hoppes and R. P. Hudson *Experimental Test of Parity Conservation in Beta Decay* Phys. Rev. 105, 1413 Published 15 February 1957

[34] T. D. Lee and C. N. Yang *Question of Parity Conservation in Weak Interactions* Phys. Rev. 104, 254 Published 1 October 1956

[35] R. L. Garwin, L. M. Lederman and M. Weinrich *Observations of the Failure of Conservation of Parity and Charge Conjugation in Meson Decays: the Magnetic Moment of the Free Muon* Phys. Rev. 105, 1415 Published 15 February 1957

[36] R. L. Garwin, D. P. Hutchinson, S. Penman and G. Shapiro *Accurate Determination of the μ^+ Magnetic Moment* Phys. Rev. 118, 271 Published 1 April 1960

[37] G. Charpak, F. J. M. Farley, R. L. Garwin, T. Muller, J. C. Sens, V. L. Telegdi and A. Zichichi *Measurement of the Anomalous Magnetic Moment of the Muon* Phys. Rev. Lett. 6, 128 Published 1 February 1961

[38] G. Charpak, F.J.M. Farley and R.L. Garwin *A New Measurement of the Anomalous Magnetic Moment of the Muon* Phys.Lett. 1 (1962) 16

[39] J. Bailey et al., *Precision measurement of the anomalous magnetic moment of the muon* Phys. Lett. B28, 287 (1968)

[40] J. H. Field and G. Fiorentini *Corrections to the g - 2 Frequency in weak focusing storage devices due to betatron oscillations* Nuovo Cim. A21, 297 (1974)

[41] F. J. M. Farley and E. Picasso *The Muon g 2 Experiments* Adv. Ser. Direct. High Energy Phys. 7, 479 (1990)

[42] J.Bailey et al., *Final report on the CERN muon storage ring including the anomalous magnetic moment and the electric dipole moment of the muon, and a direct test of relativistic time dilation* Nucl. Phys. B150, 1 (1979)

[43] B. L. Roberts *The history of the muon (g-2) experiments* SciPost Phys. Proc. 1, 032 (2019) published 20 February 2019

[44] G. W. Bennett, et al. *Final report of the E821 muon anomalous magnetic moment measurement at BNL* Phys. Rev. D 73, 072003 Published 7 April 2006

[45] D. Hanneke, S. Fogwell, and G. Gabrielse, *New Measurement of the Electron Magnetic Moment and the Fine Structure Constant* Phys. Rev. Lett. 100, 120801 Published 26 March 2008

[46] W. Liu, et al. *High Precision Measurements of the Ground State Hyperfine Structure Interval of Muonium and of the Muon Magnetic Moment* Phys. Rev. Lett. 82, 711 Published 25 January 1999

[47] Peter J. Mohr, David B. Newell, and Barry N. Taylor *CODATA recommended values of the fundamental physical constants: 2014* Rev. Mod. Phys. 88, 035009 Published 26 September 2016

[48] J. Grange, et al. *Muon g-2 Technical Design Report*   arXiv:1501.06858v2 [physics.ins-det]

[49] D. Stratakis, et al. *Accelerator performance analysis of the Fermilab Muon Campus* Phys. Rev. Accel. Beams 20, 111003

[50] A.P.Schreckenberger, et al. *The fast non-ferric kicker system for the Muon g-2 Experiment at Fermilab* Nuclear Inst. and Methods in Physics Research, A 1011 (2021) 165597

[51] N. Froemming, et al. *Commissioning the Superconducting Magnetic Inflector System for the Muon g-2 Experiment* Proc. IPAC18, Vancouver, BC, Canada, Apr. 4, pp. 18441847

[52] D. A. Sweigart *A Measurement Of The Anomalous Precession Frequency Of The Positive Muon* PhD Thesis Internal Document 20920

[53] J. Mott *Tracking analysis summary for DOE/NSF briefing* Internal Document 13705

[54] D.F.Anderson, M.Kobayashi, C.L.Woody and Y.Yoshimura, *Nuclear Instruments and Methods in Physics Research Section A: Accelerators, Spectrometers, Detectors and Associated Equipment* Nucl.Instrum.Meth.A 290 (1990) 385-389

[55] K. S. Khaw, et al. *Performance of the Muon g-2 calorimeter and readout systems measured with test beam data* Nuclear Instruments and Methods in Physics Research Section A: Accelerators, Spectrometers, Detectors and Associated Equipment Volume 945, 21 November 2019, 162558

[56] E. Hazen, A. Heister, C. Hill, J. Rohlf, S. X. Wu and D. Zou *The AMC13XG: a new generation clock/timing/DAQ module for CMS MicroTCA* JINST 8 (2013) C12036

[57] B.G. Taylor *TTC distribution for LHC detectors* IEEE Trans. Nucl. Sci. 45 (1998) 821828

[58] TRIUMF MIDAS homepage Link

[59] W. Gohn, *Data Acquisition with GPUs for Muon g-2 at Fermilab* Internal Document 7688

[60] T. Albahri, et al. *Magnetic-field measurement and analysis for the Muon g2 Experiment at Fermilab* Phys. Rev. A 103, 042208 Published 7 April 2021

[61] A. Fienberg, et al. *Methods for energy calibration and timing alignment of the calorimeters* E-989 Internal Note 173

[62] E. Bottalico, et al. *Run 1 In Fill Gain Corretion* E-989 Internal Note 193

[63] A. Anastasi, et al. *The laser-based gain monitoring system of the calorimeters in the Muon g2 experiment at Fermilab* 2019 JINST 14 P11025

[64] T. Albahri, et al. *Beam dynamics corrections to the Run-1 measurement of the muon anomalous magnetic moment at Fermilab* Phys. Rev. Accel. Beams 24, 044002 Published 27 April 2021

[65] T. Albahri, et al. *Measurement of the anomalous precession frequency of the muon in the Fermilab Muon g2 Experiment* Phys. Rev. D 103, 072002 Published 7 April 2021

[66] B. Abi, et al. *Measurement of the Positive Muon Anomalous Magnetic Moment to 0.46 ppm* Phys. Rev. Lett. 126, 141801 Published 7 April 2021

[67] T. Gorringe and K. S. Khaw, *Observation of oscillating pedestal in calorimeter channels in Run 1 data in both Q-method and T-method reconstructions* Internal Document 17149

[68] T. Gorringe, *Handling effects of vertical drift on normalization and asymmetry in Qmethod wiggle fits* Internal Document 19201

[69] T. Gorringe, *Qmethod -evidence of spin relaxation term in ω_a fits* Internal Document 18496

[70] A. T. Fienberg, *Measuring the Precession Frequency in the E989 Muon g 2 Experiment* PhD Thesis Internal Document 16264

[71] T. Gorringe, *Archiving some summed run 1 datasets, Qmethod plots* .Internal Document 24384

[72] N. Kinnaird, *Muon Spin Precession Frequency Extraction and Decay Positron Track Fitting in Run 1 Of the Fermilab Muon g 2 Experiment* PhD thesis. Internal Document 20917

[73] G. Cowan, *Statistical Data Analysis*

[74] R. Chakraborty, *Ratio Q-method Update* Internal Document 25551

[75] H. Seltman, *Approximations for Mean and Variance of a Ratio* pdf link

[76] R. Chakraborty, *Q-Method Threshold Scan for Run 2D* Internal Document 27210

[77] H. Binney, *UW ω_a update: 1.9 MHz oscillation fitting* Internal Document 26115

[78] R. Chakraborty, *UKy Q-Ratio-Preliminary Run2/3 Analysis Update* Internal Document 26662

[79] R. Chakraborty, *Change in Ratio-Q Fit Function: Asymmetry relaxation and Time dependent CBO* Internal Document 27237

[80] A. Edmonds, *Kernel for BU Ratio Method Analysis* Internal Document 26149

Vita

Ritwika Chakraborty

Place of Birth:

- Kolkata, West Bengal, India

Education:

- University of Kentucky, Lexington, Kentucky, USA
  M.S. in Physics, August 2019

- Indian Institute of Science Education and Research, Bhopal, Madhya Pradesh, India
  M.S. in Physics, May 2016

- Indian Institute of Science Education and Research, Bhopal, Madhya Pradesh, India
  B.S. in Physics, May 2016

Professional Positions:

- Graduate Teaching Assistant, University of Kentucky Fall 2016–Spring 2019

- Graduate Research Assistant, University of Kentucky Fall 2019–Present

Honors

- Max Steckler Fellowship 2017, University of Kentucky

- Indian Academy of Sciences-Summer Research Fellowship 2015

- INSPIRE SHE Fellowship, Department of Science and Technology, Govt of India - 2011-2016

Publications & Preprints:

- *Measurement of the Positive Muon Anomalous Magnetic Moment to 0.46 ppm*
  Muon $g - 2$ Collaboration
  Phys. Rev. Lett. 126, 141801 Published 7 April 2021

- *Measurement of the anomalous precession frequency of the muon in the Fermilab Muon $g - 2$ Experiment*
  Muon $g - 2$ Collaboration
  Phys. Rev. D 103, 072002 Published 7 April 2021

- *Magnetic-field measurement and analysis for the Muon $g-2$ Experiment at Fermilab*
  Muon $g-2$ Collaboration
  Phys. Rev. A 103, 042208 Published 7 April 2021

- *Beam dynamics corrections to the Run-1 measurement of the muon anomalous magnetic moment at Fermilab*
  Muon $g-2$ Collaboration
  Phys. Rev. Accel. Beams 24, 044002 Published 27 April 2021